Designing New Materials for Photocathodes

Bruno Camino
Department of Chemistry
Imperial College London

A thesis submitted for the degree of
Doctor of Philosophy

2017

Declaration of Originality

I hereby declare that the research presented in this thesis is my own. It has not been submitted in any form for another degree or academic qualification at any university or institution of higher education. Information derived from any Internet sources, books, and published or unpublished work of others has been acknowledged in the text and a list of references is given in the bibliography. Any additional sources of information have been appropriately referenced.

The research presented in this thesis was conducted under the supervision and guidance of Professor Nicholas M. Harrison at Imperial College London in South Kensington.

Bruno Camino

February 2017

Declaration of Copyright

Abstract

Free electron lasers (FELs) are state of the art in terms of generating light pulses. By using free electrons as lasing medium, FELs provide tunable radiation in the infrared to X-rays wavelength range and on the femtosecond timescale. Their use in biology, chemistry and materials science allows for the probing of dynamic processes at levels never reached before.

In order to design the new generation of FELs, a bright and low emittance electron beam must be generated from the photocathode. For this reason widespread experimental and computational efforts are taking place worldwide in order to generate more efficient materials for photocathode applications.

However, a clear understanding of the emission process and, in particular, how the process is influenced by the surface structure needs further investigation.

In this work, a computational tool based on the well know three step model (3SM) for photoemission is presented. In its original formulation, the 3SM is based on the bulk electronic structure of materials. In this study it is extended to explicit models of the surfaces. This approach retains the simple chemical intuition and it allows the disentanglement of the effect of the atomic, electronic and chemical structure of the surface on the observed photoemission. This is achieved by using a layer-by-layer decomposition of the surface electronic structure that is calculated through reliable density functional theory (DFT) calculations.

Test calculations on clean copper, silver and magnesium surfaces are reported in this thesis and compared to the measured quantum efficiency. The ability of the model to simulate the influence of surface modifications on the observed quantum efficiency are also reported: the adsorption of oxygen, hydrogen and cesium on the Mg (0001) surface and the presence of steps on the Ag (111) surface are discussed. Hydrogen and oxygen were selected because they are well known contaminants of photocathode surfaces and cesium was simulated because it is commonly used to enhance the quantum efficiency of photoemitting materials. The calculations allow the known effects of surface states and

work function changes to be rationalised. Furthermore, the simulations of the adsorbate covered surfaces generated some counter intuitive results that can be explained by the model developed in this work.

The computational tool presented in this thesis has already provided some insights on how surface chemistry and reconstruction influence the quantum efficiency of materials currently used in photocathodes and will be used in future studies to generate guidelines for the design of more efficient photocathodes.

Acknowledgments

The first version of the acknowledgments I wrote was longer than one of my results chapters. This is because the PhD has been a very long journey for me and I feel like there are so many people who deserve a huge thank you. However, here I will only give a condensed version of my acknowledgments, after all, the people who made a difference to me know it already and don't need to read it here.

First of all I want to thank my supervisor, Prof Nic Harrison, for having been my guide in this journey. I have always learned something from our conversations, about science or about books and wine and I will take away with me everything you taught me. I also want to thank the ASTeC group at the Daresbury Laboratory, in particular Mark, Tim, Elaine and everyone involved in the Photocathode Design project. Collaborating with you has been a great scientific opportunity. Of the people I met at the Daresbury Lab I also want to acknowledge Sonal, most of all for our post-meeting chats along the canal, you know how helpful they were and I hope our paths will cross again in the future. Anna, at any important stage of my career, I will always be grateful for what you taught me during the time you were my supervisor. All of this would not have happened if you hadn't given me the chance to prove to you how passionate I am about science.

Maman and Papi, a whole book would not be enough to thank you for being so special, I will limit myself to saying that you have been the most amazing parents someone could have asked for and I feel blessed that you were mine. Thank you because you gave me all the means to live the life I wanted and your support, in many decisions I took, is my strength and made me the person I am. Nonna, unfortunately you are no longer here to see my achievements, but you were there when I started and I often think of you and how proud of me you would be now.

During these years in London I met some pretty amazing people. No one deserves the top of the list as much as Tetta. You are among my dearest friends and the sister I never had, also after having shared the office with me for such a long time, you know more than anyone else how hard this was for me. I can't imagine going through my PhD (and though life) without you on my side. We shared so many great and intense moments during these years and it makes me emotional even just starting to think about it. Our paths might be going in different directions now, but I have no doubts we will find new ways for our friendship to grow even stronger. Miguel, I honestly don't remember how my life was before having you in it, the way we take care of each other is simply stunning. Thank you for being sensitive, a good listener and dressing well (your turn). Dr. Katia, you know how much this document means and your advice, particularly during the final months, was invaluable, but most of all I want to thank you for helping me in the process of being more open to the world and teaching me to be proud of who I am. Nicoló, at first you fascinated me with the scientifically wrong explanation of how a radiometer works. Then we learned to discover one another the way Antoine de Saint-Exupéry taught us: step by step and I found out that's the fastest way to build incredibly strong relationships. Valentina R, you were my first friend in London and anyone who has moved to a big city will realise how much this means and how special our relationship will always be for me. Grant, we had a great time together, the trip to South Africa has been among the best of my life. Also, thank you for making me more open minded, in particular about Italian (inspired) cuisine. Ste, my small avocado, what an amazing period it was when we lived together in London. Thank you because whether you are next to me, or thousands of kilometers apart you always manage to cheer me up, I literally think of you everyday, when I look at my arm. Luca, I don't even know where to start, getting to know you better during the year you lived in London (among astrology, aliens, etc.) is one of the things I am most grateful for. You are a very special human being and I feel blessed to have you in my life. Carmine, you have been so important at the stage of my life when I met you and I honestly don't know where I would be now if we hadn't had that clumsy conversation on that cold December night. You are one of the most important people in my life. Also, thank you for introducing me to Felix, you are the most beautiful couple ever. Chiara, I think we built a very special friendship, I don't think anyone ever made me laugh as much as you do. I hope ours is a bond that will last despite the distance. Valentina S (aka "my giraffe"), ours is that kind of friendship that doesn't need so much time spent together, but still means a lot. Any single moment shared with you was special. Also, you taught me a very important lesson that I keep repeating to myself: "after all, what could possibly go wrong? And when everything goes wrong, I'm a seagull!". Diogo, I have a lot of great memories with you and I am very happy we met and managed to be there for one another through all these years. Gabri, we went a long way since we met in Golders Green that morning. We both changed a lot during these years, not only talking about hair and beards. It has been great to have you on my side during this journey, thank you. Francesca DSP, our lives have certainly not taken the path I hoped for when I was 7 years old. I guess it is for the best because I could not imagine loving a friend more than I do love you. What an amazing month this March 2017 has been for both of us: a mom and a Doctor, I am sure we will remember it forever. Lucinda and Marina, you are the best landlady and neighbour I could ever have had. I moved to Quadrant Grove for what was supposed to be three months and ended up being two years, I think this says a lot about how great an experience that was.

As I was warned when I moved to London, friendships here have an expiration date because people come and go all the time. In my experience that is absolutely true: my group of friends changed so many time while I was living here. However, even though some of the people I met were in my life for only a few months, or even just one day, they left something precious behind that I carry in my heart everyday. What an honour it was being accepted in the midwives group: Roberta, Alessia, Noemi and Eleonora, all of you are special in your own way, I have a lot of great memories with you and I am glad I had the opportunity to meet you. In random order, I want to thank Nicoleta, Jacopo, Luca C and Alessandra (the best worst-decisions team, so grateful for that!), Marco, Panos, Álvaro, Matteo, Lefteris, Annika, Eduardo, Chris (thanks for the free yoga classes and the riverside Negronis, both helped the writing up phase) and many more, for one reason or another you all made a difference to me and I am infinitely grateful for that. I hope our paths will cross again.

And let's not forget all the people who were in my life before this wonderful experience and whose friendship was not undermined by the distance, but on the contrary, grew more and more important in my life: Anna, Japo, Fede, Giulia, Valeria, Francesca.

During these years I shared (too many) offices with great people at Imperial. First of all, thank you Ariadna, we had a lot beautiful moments and a lot of not so beautiful moments and having you on my side has been my strength. One of the most precious things I will bring with me after this PhD is our friendship. Giuseppe, thank you so much for having helped me from the very beginning of my PhD and for having been an essential part of it. Then a huge thank you goes to Monica (your work has been a great inspiration for me), Ruth, Romi, David, Fred, Andy (for proof reading this!!), Vincent, Tim, Stefano, Basma, Rosalia and Emma. It has been a pleasure to meet all of you on my path.

Publications

Publications based on this work:

B. Camino, T. C. Q. Noakes, M. Surman, E. A. Seddon and N. M. Harrison "Photoemission simulation for photocathode design: theory and application to copper and silver surfaces", *Computational Materials Science*, **122**, 331 (2016).

B. Camino, A. Lorusso, A. Perrone, N. M. Harrison "Experimental and theoretical study of Mg and Y as photoemitting materials", *In preparation.*

Presentations

Selection of the presentations based on this work:

Talks

ASTeC Early Stage Research Workshop, Cockcroft Institute for Accelerator Science, Daresbury Laboratory, July 2015. (Awarded the "Best Presentation Award")

European Workshop on Photocathodes for Particle Accelerator Applications, Cockcroft Institute for Accelerator Science, STFC Daresbury Laboratory, June 2016.

Postgraduate Symposium, Imperial College London, July 2016.

Invited Seminar, Universitá del Salento, December 2016.

Posters

Modelling in Solid State Chemistry, Imperial College London, Sept 2013.

Emerging Photon Technologies for Chemical Dynamics: Faraday Discussion 171, Sheffield, July 2014.

Postgraduate Symposium, Imperial College London, July 2015.

Modelling in Solid State Chemistry, Imperial College London, Sept 2016.

Le bonheur n'est pas
au bout du chemin...
Le bonheur est le chemin.

Contents

List of Figures

List of Tables

List of Acronyms

3GLS	third generation light source
4GLS	fourth generation light source
AO	atomic orbital
BF	Bloch function
BZ	Brillouin zone
CO	crystalline orbital
DFT	density functional theory
DOS	density of states
FBZ	first Brillouin zone
FEL	free electron laser
GGA	generalised-gradient approximation
GS	ground state
GTO	Gaussian-type orbital
HF	Hartree-Fock
HHG	high harmonic generation
IR	infrared
KS	Kohn-Sham
LCAO	linear combination of atomic orbitals
LDA	local-density approximation
LINAC	linear accelerator
MO	molecular orbital
MPA	Mulliken population analysis
PES	photoelectron spectroscopy
PDOS	projected density of states
PP	pseudopotential
PW	plane-wave
QE	quantum efficiency
SCF	self-consistent field
STO	Slater-type orbital
UV	ultraviolet
WF	work function
XFEL	X-ray free electron laser
XRD	X-ray diffraction

1

Introduction

Spectroscopy is an invaluable tool for the study of matter, chemistry and biological processes. Optical spectroscopy usually refers to the use of the infrared (IR), visible (Vis) and ultraviolet (UV) domains of the electromagnetic spectrum. These techniques provide information about the vibration states and electronic excitations as the system evolves. However, connecting the changes recorded by such techniques to structural changes of the system can only be achieved rigorously for simple molecules (diatomic or triatomic), whose ground and excited state potential energy surfaces are known from theoretical studies. This is because these spectroscopies lack the spatial and temporal resolution needed to identify unambiguously the contribution of molecular motifs to the overall adsorbtion of a system due to restrictions in spatial (1 Å) and temporal resolution (few fs).

X-rays provide such spatial resolution and have been used for many years in crystallography. Short (in time) pulses of highly focussed X-rays would combine the spatial and temporal resolution in order to get information about the structural changes of chemical and biological systems never achieved before. For this reason many international efforts have been initiated for the development of light sources able to deliver ultrafast pulses of light, ranging between the IR to X-rays domains.

Nowadays so-called fourth generation light sources [10–12] (4GLSs) are available and still under development. A detailed discussion of the theory and differences between third and fourth generation light sources is presented in the next chapter. Here only a brief discussion of the advantages of 4GLSs and the new scientific opportunities that can be achieved through them are presented in order to give a context for this project.

Among 4GLSs, one of the most promising developments are free electron lasers (FELs). As suggested by the name, these device use free electrons as lasing medium, as opposite to electrons bound at quantised energy levels in atoms, like normal lasers. Among the advantages of FELs there are the transverse coherence of the radiation, pulses in the timescale of fs and orders of magnitude more intense than previous light sources. The theory of FEL was proposed in 1970 [13] and since then, FELs operating at various wavelength in the IR-UV domains became available. However, it was the first lasing of the LCLS [14] at the SLAC National Accelerator Laboratory in October 2009 that represented a turning point in what can be achieved in terms in spectroscopic analysis. This is because LCLS was the first FEL to operate in the X-ray domain, obtaining light pulses in the timescale of fs and 10 orders of magnitude more intense than the previous light sources.

The 2014 Faraday Discussion 171 held in Sheffield (UK) was about "*Emerging photon technologies for chemical dynamics*". The proceedings published in this issue [15] offer a great example of the state of the art in terms of light sources and a science showcase of the new results that can be achieved through 4GLSs. Some of those are discussed in the next chapter and they include single molecule diffraction, nanocrystal imagining and subcellular imaging.

One of the basic components of FELs is the photocathode, which is the source of electrons used to generate the light pulse. Although photocathodes were already part of the set up of third generation light sources (3GLSs), they became a key underpinning technology with the introduction of 4GLSs. The reason for this is in 3GLSs the electron beam travels thought the accelerator many times (typically around 10^{11} times) and radiation damping [12] improves the properties of the circulating beam. On the contrary, FELs are single-pass machines, which means electrons generated from the photocathode travel through the machine once, they generate the light pulse and are deflected. Therefore, the quality of the electron beam in terms of focusing and brightness as emitted from the photocathode determines the properties of the emitted radiation.

The first XFELs were built using technologies developed for 3GLSs, which proved to be adequate but not ideal for FEL applications. The development of the first XFELs showed that a significant increase in the quantum efficiency (QE) of emitting materials and a significative (one order of magnitude) reduction of the transverse beam emittance of the electron beam is required in order to develop more efficient and less expensive accelerators [5, 16, 17].

A very good summary of the requirement for new and more efficient photocathodes can be found in Ref. [5], where a three points R&D plan for cathode development is discussed. The three points are:

- **experimental validation of emission properties** obtained through surface and bulk analysis of photoemitting materials;
- **development of reliable models to describe photoemission**. Several photoemission theories are available nowadays. However, none of them provides an efficient design oriented tool able to take into account the details of emission and provide the experimentalists with insights on how to generate more efficient materials;
- **testing of photocathode materials in operational systems**.

The work described in this thesis focuses on the second point. It is the result of a collaboration started by the ASTeC [18] group based at the STFC Daresbury Laboratory and the Computational Materials Science (CMS) group [19] at Imperial College London. The ASTeC is the centre of expertise in the charged particle acceleration field in the UK and it groups under its name scientists from different fields of the design of accelerators, ranging from the Accelerator Physics Group to the Vacuum Science Group, in order to develop and test world leading accelerators from any point of view of their design and construction covering all the points of the R&D plan discussed above.

This project aims at achieving a more rational design of emitting materials to be used in photocathodes by combining the experimental and theoretical approaches to the photocathode development. It will benefit from the expertise of the ASTeC group in the preparation and characterisation of materials and from the expertise in material simulations of the CMS group.

This thesis has two main goals. The first one is presenting a computational tool able to predict photoemission from materials in real environment and test such tool on simple systems for which experimental and computational data are available. The second aim is using this theory to simulate the behaviour of photocathodes after surface modification and give some preliminary guidelines for the rational design of photocathodes.

Overall, this thesis consists of 10 chapters. Starting from the brief introduction to the challenge faced by the project presented in this chapter, Chapter 2 describes some of the available technology in terms of light generation and emitting materials, pointing out which are those aspect that are expected to have particular impact in this field. In Chapter 3, the underlying theory of electronic structure used to compute the material properties and its implementation on modern quantum chemistry codes is discussed. The model used to simulate surfaces is also presented. The main two theories of photoemission, the one step and three step models, are explained in Chapter 4 and the differences between them are highlighted. The reasons for the choice of the three step model and its extension to surface calculations are also described in this chapter. Chapters 5 to 8 contain the discussion of the results of this work. In Chapter 5 the simulated structure of the three substrates studied here (copper, silver and magnesium) are discussed in terms of geometry and electronic structure of the bulk and surfaces. Chapter 6 validates the photoemission model presented in Chapter 4 on three low Miller indices surfaces for Cu, Ag and Mg. Surface chemistry, one of the main tools to tune the properties of emitting materials is simulated through the adsorption of oxygen, hydrogen and cesium on the Mg (0001) surface, in Chapter 7. The adsorption geometry and variations in terms of work function, electronic structure and finally, quantum efficiency of the modified structures with respect to the clean one are thoroughly discussed. In order to introduce one of the surface reconstructions that could be used to enhance the QE of emitting materials, the series of Ag (x11) vicinal surfaces is simulated in Chapter 8. The WF and electronic structure changes of these surfaces are discussed and compared to the pristine Ag (111) surface. Chapter 9 summarises the results of the previous three chapters and highlights how the knowledge gained from this project can be used by experimentalists in order to design more efficient materials. Lastly, Chapter 10 closes this thesis summarising the findings and providing an outlook on future science possibilities following this project.

2

Context and Background

This chapter will provide some background in order to understand the context of this research and an overview of the final applications of photocathodes. The underlying theory of light sources, in particular synchrotrons and free electron lasers (FELs) is presented in the first part of the chapter. The discussion focuses then on the photoinjectors and photocathode materials, the latter being the target of this work. Furthermore, the challenge and the questions this research aims to answer are discussed in Section 2.4.

2.1 Core Motivation

The ability to generate pulses of X-rays in the timescale of fs gives access to information about atomic and electronic dynamics that was not accessible before. Such short pulses can be generated by X-ray free electron lasers (XFELs), whose structure is described in Section 2.2. A key factor in order to design cost effective and more efficient XFELs is being able to obtain intense and focused electron bunches directly from the photocathode. The reason for this is the lack, in FELs, of the possibility to improve the quality of the electron bunch after emission, as opposite to synchrotrons, where the quality of the radiation depends on the quality of the booster ring used to focus and accelerate the electron bunch.

More efficient photocathodes can only be obtained though a rational design of materials, achievable by combining experimental characterisation and atomistic simulations [5]. These latter can be used to disentangle the influence of material composition and structure on the efficiency of materials. Also, it is able to screen materials and surface modifications more easily and cost effectively than the experimental approach. This thesis tackles the problem from the computational side. However, it must be com-

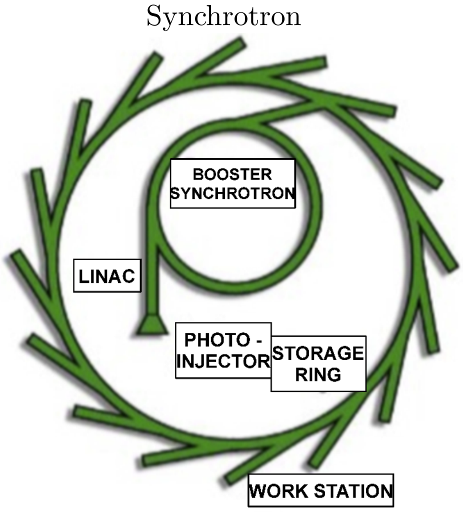

Figure 2.1: Schematic representation of a synchrotron. Image adapted from the BESSY II - Helmholtz-Zentrum Berlin (HZB) website [1]

bined with efforts from the experimental point of view in order to validate the results presented here and to give insights on which are the best candidates to be synthesized and tested in the working environments of the photoinjectors.

2.2 Fourth Generation vs. Third Generation Light Sources

Synchrotrons [20] are circular particle accelerators that use magnets to bend the path of the particles. They were proposed independently by Vladimir Veksler in 1944 and Edwin McMillan in 1945 [21]. Their first application was in the high-energy or nuclear physics communities which considered the synchrotron radiation, which is the radiation emitted by any charged particle when accelerated, as a nuisance because it limited the acceleration the electron beam was able to reach. However, when the scientific community realised the importance of such radiation, these devices were improved and became leading class machines in the field of light generation.

Synchrotrons reached their third generation, the main difference with the first and second generations is a greater control on the properties of the emitted X-rays in terms of brightness and spatial coherence achieved through the introduction of undulators and wigglers in the design of the accelerator.

A schematic representation of a third generation synchrotron is showed in Fig. 2.1

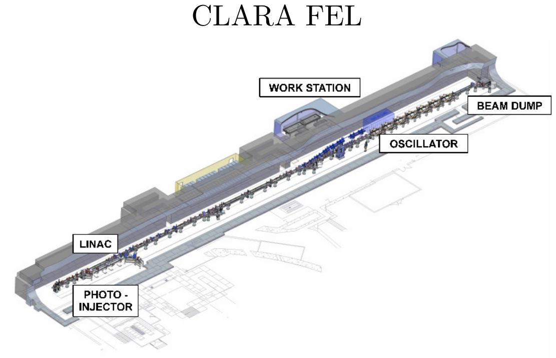

Figure 2.2: Schematic representation of the CLARA FEL. Image adapted from the CLARA conceptual design report [2].

and its main components are highlighted. The electron beam is generated from the photoinjector, it is then focused and accelerated by radio frequency electromagnetic fields and steered by dipole and quadrapole magnets in the booster ring where electrons reach approximatively 99.9999985 % of the speed of light. When the electron beam reaches the required speed and focusing it enters the main ring, where it is stored and radiation is generated and directed to the different work stations, called endstations, where experiments take place.

Synchrotrons are very well developed machines and are available worldwide in different sizes, from laboratory apparatus for a single group to large facilities where thousands of scientist can perform each year their experiments. The UK state of the art multi user facility is the Diamond light source, part of the STFC and Wellcome Trust [22].

The possibility of using free electrons to generate radiation was first proposed by John Madley while he was working on his PhD project at the Physics Department of the Stanford University in 1970 [13]. Normal lasers use various lasing mediums, such as gases (He-Ne), solid state (Nb:YVO_4) or semiconductor (alloys of Al and GaAs) among others. The main difference between this types of mediums and free electrons is that the latter are not discrete in energy, therefore their wavelength is tunable, as opposite to the electrons bound to atoms, which occupy discrete energy levels.

The schematic representation of a FEL is shown in Fig. 2.2. The electron bunch enters the machine from the photoinjector. It is then accelerated by linear accelerators (LINAC) and the light pulse is generated, by the transverse motion of electrons passing through an undulator. The undulator is an array of magnets whose distance will determine the wavelength of the laser. An enlargement of the undulator is represented in Fig. 2.3 and Fig 2.4. FELs are defined single pass machines, referring to the fact

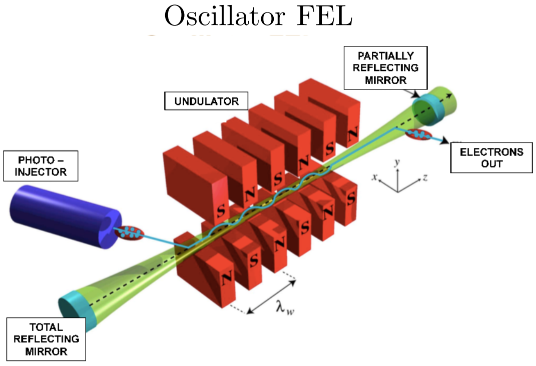
Oscillator FEL

Figure 2.3: Schematic representation of an oscillator FEL. Image adapted from “Oscillator FEL clip” from Vanderbilt University website [3]

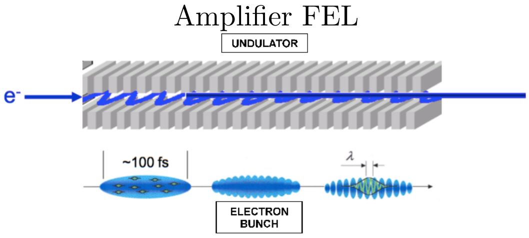
Amplifier FEL

Figure 2.4: Schematic representation of an amplifier FEL.

that electrons go through the accelerator once and are deflected at the end of their path after light has been generated. From the photocathode design point of view this is the main difference between synchrotrons and FELs: the quality of the electron bunch can be improved in synchrotrons, whereas in FELs the quality of the electron beam as it is emitted from the photocathode will influence the quality of the emitted radiation. A sharp and intense light pulse will be obtained from a focused and bright electron pulse. If the electron distribution is spread in time, a broad and less intense light pulse is obtained. For these reasons, photocathode development became one of the main research areas in the optimisation of new light sources.

When the electrons enter the undulator, they occupy random position in the bunch and the light they emit is therefore incoherent. In order to obtain coherent emission, which produces brighter and time focused light pulses, the electrons need to be bunched. This can be achieved in two ways, depending on the wavelength of the emitted radiation, by using oscillators or amplifiers. The difference between the two is briefly discussed.

- **Oscillator**: these can only be used for longer wavelengths (IR-UV). The schematic representation of an oscillator FEL is depicted in Fig 2.3. The two metal mirrors reflect the radiation generated by the electrons and the radiation acts back on the electron bunch causing the microbunching at the required wavelength. The total reflecting mirror is usually a metal plate, whereas the partlially reflecting one is a metal plate with a hole in the centre. One of the requirements for the mechanism to work is having a distance between mirrors that matches an integer number of wavelengths. This set up can only be used at wavelengths for which reflecting materials are available. Oscillator FELs are well tested and developed and reached the status of operational machines.

- **Amplifier**: these are used for shorter wavelengths (XUV and X-rays), for which no reflecting materials exist. The amplification must happen in a single pass and it is based on the principle of the self-amplified spontaneous emission (SASE). In the SASE regime, electrons are distributed randomly in the bunch emitted from the photocathode and start emitting radiation as they enter the undulator. The radiation itself interacts with the motion of electrons causing microbunches separated by one wavelength, this is represented in Fig. 2.4. This way a coherent light pulse is generated. However, the output is noisy in time and frequency and longer undulators are required, usually between the 10s and the 100s of meters. This type of machines are still under development.

An example of an oscillator FEL is the ALICE FEL (which is the acronym for Accelerators and Lasers In Combined Experiments) [23] at the Daresbury Laboratory developed by the ASTeC group [18]. It achieved its first lasing in 2010, making it the first UK FEL. It works in the IR region of the spectra, with a tunable wavelength of 5-9μm. One of its first application as a user facility has been the study of esophageal cancer cells [24] in collaboration with the University of Liverpool.

The first XFEL (operational since October 2009), which uses the amplifier set up, is the Linac Coherent Light Source (LCLS) at SLAC National Accelerator Laboratory in Stanford [14]. It is based on a preexisting 1 km long LINAC and a 130 m undulator. Other XFELs in the world are the SACLA in Japan [25], FLASH in Germany [26] and SwissFEL in Switzerland [27] among the most important ones.

The new UK FEL, named Compact Linear Accelerator for Research and Applications (CLARA) is currently under construction at the Daresbury Laboratory. This facility will be a UV FEL and aims at being a R&D facility for the development of more efficient XFELs. CLARA will use the VELA (Versatile Electron Linear Accelerator) as electron source, which has already been tested and used as user facility [28].

X-rays pulses in the timescale of fs and up to ten orders of magnitude more intense than the ones provided by the state of the art synchrotrons will bring advances in many fields of science, such as chemistry, biology and materials science. For example, among the 45000 protein structures available nowadays, only 450 of them are membrane proteins. The reason being membrane protein are extremely difficult to crystallise, excluding them from the usual X-rays experiments on crystallised proteins. Applications of XFELs on diluted solutions of proteins has already offered insights into some of them. Last November Science [29] published a study called "Structure of photosystem II and substrate binding at room temperature" performed at LCLS. Photosynthesis is one of the key processes for life on our planet and still it is not fully understood.

By using the ultrashort (40 fs) pulses of X-rays with resolution of 2 Å provided by the LCLS, it was possible to take images of the protein involved in photosystem II when it links to oxygen. Although this had already been achieved with frozen samples, this is the first time the complex could be observed in solution providing a better description of its working in nature. Outcomes of this study elucidate which is the mechanism for bond formation among the ones previously proposed in literature and will be used to develop more efficient mechanisms for light to fuel conversion thought photoelectrochemical water splitting.

The light sources discussed until now are all large-scale installation. The development of high harmonic generation (HHG) represents the most important advancement in terms of light sources at a laboratory scale. HHG sources operate in the VUV and XUV range and are the only devices able to reach the attosecond regime. Although some of the developments in the field of FELs will benefit also the HHG field, photocathode design is not one of them because in HHG sources no electrons are involved in the generation of the light pulse. For this reason the HHG theory and technology will not be discussed in this thesis. It was, however, mentioned here because it is part of the emerging technologies for ultra fast experiments.

The advantages of FELs over previous generation light sources are not only about the brightness of the beam, but include also transverse coherence, short pulses and X-rays generation. Nevertheless, synchrotrons will remain the best choice to study the range of processes happening in the timescale between 100ps and milliseconds, such as excited state structures [11].

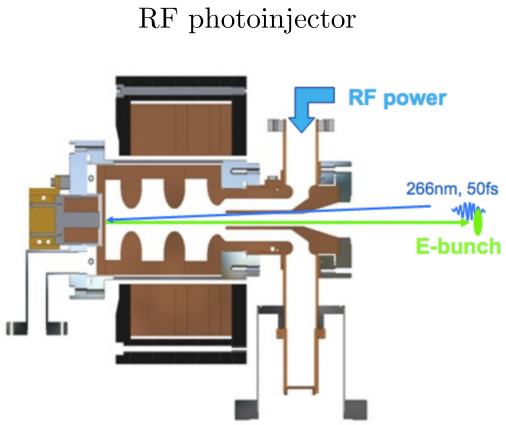

Figure 2.5: Schematic representation of an RF photoinjector. Image adapted from Ref. [4]

2.3 Photocathode Materials and Requirements

In synchrotrons and FELs, electron bunches are generated from a photoinjector. Among the most widely used there are radiofrequency guns (RF guns). In these, a RF couples with the electron bunch and accelerates it towards the exit of the photoinjector. A schematic representation of a photoinjector is shown in Fig. 2.5, where the main components are highlighted. On the left hand side of the picture there is the photocathode. The basic working of a photocathode can be described as photons, from a laser light source, reaching the photocathode surface and causing electrons to be ejected through photoelectric effect, as it is schematically depicted in Fig. 2.6.

Since the goal of this work is improving the photocathode material, the discussion here is focused on this part of the photoinjector. For a detailed discussion of the state of the art advancements of the other components of a photoinjector see Ref. [30].

The properties of photocathodes are:

- **quantum efficiency (QE)**: number of electrons emitted per incident photon;
- **spectral response**: variation of QE with wavelength of the laser light used to generate electrons;
- **response time**: length of the electron bunch for an infinitely short light pulse;
- **emittance**: size of the electron bunch in the plane perpendicular to the direction of propagation;

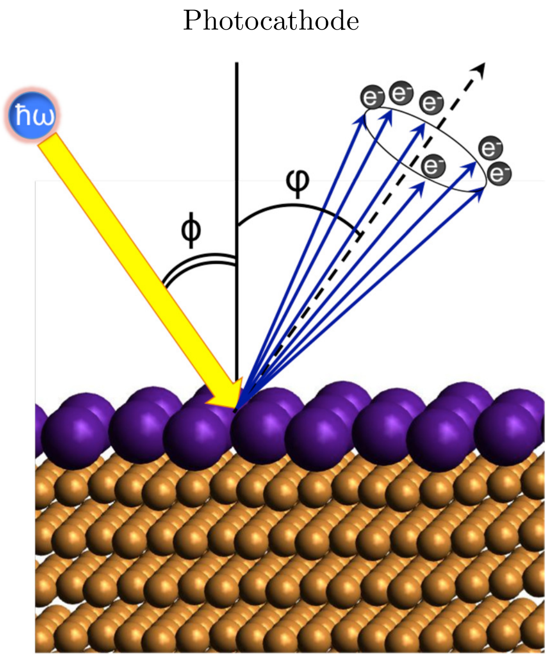

Figure 2.6: Schematic representation of a photocathode surface.

- **lifetime**: performance of the photocathode in time.

An ideal photocathode has high quantum efficiency, short response time, low emittance and long lifetime. Unfortunately there is no system that satisfies all these requirements yet. The main focus of this work is on the QE and spectral response. The emittance will be the next step of the project.

Photocathodes can be divided according to the materials used, in four main classes:

- Metals
  - normal conductivity
  - super conductivity
- Semiconductors
  - negative electron affinity (NEA)
  - positive electron affinity (PEA)

Their main properties are summarised in Table 2.1. Metals are characterised by low thermal emittance, which is one of the requirements for the amplifier FELs. They are,

Table 2.1: Properties of the four main classes of photocathode materials [5].

Class	Sub-class	Material	QE	λ	Application
Metal	Normal conducting	Cu, Mg, Ag	10^{-5}-10^{-4}	UV	Amplifier FELs Low Repetition Rate
	Super conducting	Nb, Pb	10^{-5}-10^{-4}	UV	Amplifier FELs - HRR High Repetition Rate
Semiconductor	PEA	Cs_3Sb	0.1-0.2	Uv-Vis	Oscillator FELs High Repetition Rate
	NEA	GaN(Cs)	0.1-0.2	Vis-IR	Oscillator FELs High Repetition Rate Polarised Electrons

therefore, used for XFELs applications despite their lower QE compared to semiconductors. For high repetition rate (frequency of the pulses $\geq$ 100 kHz), superconducting metals must be used. Oscillator FELs can accept electron bunches characterised by higher emittance. Therefore semiconductors are used since they provide QE up to three orders of magnitude higher than metals. Both positive and negative electron affinity materials can be used for high repetition rate. The negative electron affinity semiconductors also provide polarised electrons.

This project focuses on the normally conductive materials (copper, silver and magnesium) in the specific because they are the one that are going to be tested for applications in the VELA photoinjector for CLARA.

2.4 The Challenge

In this chapter the reasons why the accelerator community needs more efficient photocathodes to develop the new generation of light sources was explained. The gaps in our understanding of the emission process were recognised and a detailed R&D plan is taking place worldwide in order to obtain materials suitable for the next generation of FELs.

This works aims at studying the photoemission from the computational point of view. There are two main reasons for modelling the photoemission. The first is giving a better understanding of the factors influencing the efficiency of current materials. The second one is being able to predict efficiency from differently engineered surfaces and guide the experimentalists in the choice of new materials to be tested in photoinjectors.

The first challenge faced by this project was the lack of a theory that could predict photoemission from real environment materials. Available photoemission theory (discussed in Chapter 5) are either based on the bulk or on very approximated models of the surface potential. Therefore, half of the time resources used in this PhD project was devoted to the development of a theory able to model materials in their operational environment.

Once this tool has been developed and validated on simple systems, it has been used to generate trends on the efficiency of materials due to surface modifications such as presence of adsorbates at different coverages and surface reconstruction (described in Chapters 7 and 8). These preliminary results and the future simulations based on the theory developed here will provide the experimentalists with guidelines in order to achieve a more rational design of photoemitting materials.

3

Theoretical Model

3.1 Electronic Structure Methods

In this chapter, the electronic structure methods used to simulate the properties of molecules and materials are presented. Firstly, an overview of the underlying theory is discussed. Electronic structure methods can be divided in two main groups: wave function methods and density functional methods. The discussion focuses, then, on the modelling of 3D and 2D materials and the properties that can be obtained by theoretical models. Finally, the computational set up for the simulations described in Chapters 5-8 is discussed in Section 3.6.

3.1.1 The Schrödinger Equation

According [1] to the fifth postulate of the quantum mechanics "*The wave function of a system evolves in time according to the time-dependent Schrödinger Equation*":

$$i\hbar\frac{\partial\Psi(\mathbf{r},t)}{\partial t} = \left[-\frac{\hbar^2}{2m}\frac{\partial^2}{\partial\mathbf{r}^2} + \hat{V}(\mathbf{r})\right]\Psi(\mathbf{r},t), \tag{3.1}$$

where i is the imaginary unit, $\hbar$ is the reduced Planck constant, $\mathbf{r}$ and m are the spatial coordinate and the mass of the electron, t is the time, Ψ is the wavefunction and $\hat{V}$ the potential. This equation can be rewritten in order to separate the space and time terms. Most of the times the property of interest does not depend explicitely on time and the time-independent Schrödinger equation can be used:

$$\hat{H}|\Psi\rangle = E|\Psi\rangle \tag{3.2}$$

---

[1] The theoretical background discussed in this Chapter can be found in references [31–34]

where Ψ is a function of the three spatial and one spin coordinates for each particle. All the information about the electrons in the system is contained in Ψ (first postulate of the quantum mechanics). E is the total energy and $\hat{H}$ is the Hamiltonian operator, whose eigenvalues, when it operates on the Ψ, are the energy levels of the system. For a system containing N electrons and M nuclei, $\hat{H}$ can be written, in atomic units, as:

$$\begin{aligned}\hat{H} &= \hat{T}_e + \hat{T}_n + \hat{V}_{ne} + \hat{V}_{nn} + \hat{V}_{ee} \\ &= \sum_{i=1}^{N} -\frac{1}{2}\nabla_i^2 + \sum_{A=1}^{M} -\frac{1}{2M_A}\nabla_A^2 + \sum_{i=1}^{N}\sum_{A=1}^{M} -\frac{Z_A}{|\mathbf{r}_i - \mathbf{r}_A|} + \\ &+ \sum_{A=1}^{M}\sum_{B>A}^{M} \frac{Z_A Z_B}{|\mathbf{r}_A - \mathbf{r}_B|} + \sum_{i=1}^{N}\sum_{j>i}^{N} \frac{1}{|\mathbf{r}_i - \mathbf{r}_j|}\end{aligned} \tag{3.3}$$

where $\hat{T}_e$ and $\hat{T}_n$ are the kinetic energy of the nuclei and of the electrons, respectively. In a quantum mechanical system, the potential energy can be divided into three types of interactions: the nucleus-electron ($\hat{V}_{ne}$), nucleus-nucleus ($\hat{V}_{nn}$) and the electron-electron ($\hat{V}_{ee}$) interactions. The r_i and r_A are the coordinates of the electron i and the nucleus A (throughout this chapter italic lower case Roman letters refer to electrons and upper case letters to nuclei). M_A is the mass of the atom A and Z_A is its atomic number. The spin coordinate is omitted for the sake of simplicity.

By using the Born-Oppenheimer approximation [2], the Hamiltonian can be simplified to:

$$\begin{aligned}\hat{H} &= \hat{T}_e + \hat{V}_{ne} + \hat{V}_{ee} \\ &= \sum_{i=1}^{N} -\frac{1}{2}\nabla_i^2 + \sum_{i=1}^{N}\sum_{A=1}^{M} -\frac{Z_A}{|\mathbf{r}_i - \mathbf{r}_A|} + \sum_{i=1}^{N}\sum_{j>i}^{N} \frac{1}{|\mathbf{r}_i - \mathbf{r}_j|}\end{aligned} \tag{3.4}$$

Even under this approximation, the Schrödinger Equation cannot be solved exactly as any n-body problem where n is greater than two. Therefore, many methods to approximate its solution have been developed. These can be divided into two main groups: the wave-function based methods and density functional methods, that are briefly discussed in the following.

---

[2] The ratio between the masses of atoms and electrons is higher than 1800. The former can, therefore, be considered as fixed with respect to the latter. Under the Born-Oppenheimer approximation the kinetic energy of the nuclei is zero and their potential energy is constant for a fixed geometry. If this approximation is used, the energy depends parametrically on the coordinates of the nuclei ($E(\mathbf{R})$).

3.1.2 Wave Function Methods

The wave function based methods rely on the variational principle, which states that the energy E of a trial wavefunction Ψ_{tr} is greater than or equal to the ground state solution of the wave function Ψ_0:

$$E\left[\Psi_{tr}\right] \geq E_0 \tag{3.5}$$

where E_0 is the exact energy of the ground state. This method gives a criteria to improve the wave function at different cycles of an iterative procedure. The Hartree-Fock (HF) method is one of the simplest wave function methods. It determines the best mono determinant approximation to the wave function by describing each electron in the mean field of all the other electrons and nuclei. The wave function is represented by a single Slater determinant in order to take into account the fact that it is antisymmetric. The main drawback of this approximation is the lack of electron correlation, which is a measure of how much the position of an electron is influenced by the position of the other electrons. The electron correlation energy is defined as the difference between the energy obtained by solving exactly the Schrödinger equation (E_S) and the Hartree-Fock energy (E_{HF}) in the limit of a complete basis set:

$$E_c = E_{HF} - E_S \tag{3.6}$$

The E_{HF} can, in general, account for 99% of the total energy of the system. However, it is often the missing 1% that is relevant to chemical processes.

Methods that take into account the E_c use the Hartree-Fock wave function as a starting point and expand the wave function into a multi-determinantal representation. The wavefunction, can be expressed as:

$$\Psi = a_0 \Phi_{HF} + \sum_i a_i \Phi_i \tag{3.7}$$

where the Φ_i are the determinant of the single, double, triple (etc.) excitations:

$$\Psi = a_0 \Phi_{HF} + a_i^a \Phi_i^a + a_{ij}^{ab} \Phi_{ij}^{ab} + a_{ijk}^{abc} \Phi_{ijk}^{abc} \tag{3.8}$$

where, in the term Φ_i^a one electron was excited from the electronic state i to the virtual state a. Configuration Interaction (CI) and Coupled Cluster (CC) methods are examples of techniques based on Eq. 3.7 and 3.8. The difference between the two is the way the coefficients a_i are calculated.

They are labelled according to the order of the highest excitation included in the expansion as CISD and CCSD when the sum is truncated to the double excitations, CISDT and CCSDT when excitation up to the triple excited states are included and so on.

Methods based on the perturbation theory use a different approach: the HF Hamiltonian is the starting point and then a perturbation is added, weighted by a parameter Λ:

$$\hat{H} = \hat{H}_0 + \Lambda \hat{H}' \tag{3.9}$$

where $\hat{H}'$ is the perturbation. An example of this class of methods is the Møller-Plesset perturbation theory, where the $\hat{H}_0$ is a sum of Fock operators. The electronic correlation is added starting from the doubly excited determinants (the order zero is just the sum of the eigenvalues and at order one it is the HF energy). The MP method is labelled according to the highest excitation included in the expansion (MP2, MP3, MP4, ...).

These methods give very accurate results when high order excitations are included and can lead to the correct solution to the Schrödinger equation for full-CI (where all excitations are included) and very large basis sets are employed. Until recent developments (discussed in the following) due to their computational cost they were mainly used as benchmark for other methods [35]. On textbooks, their scaling is reported to range from M^5 for CIS, CCSD and MP2 to M^{10} for CISDTQ, CCSDTQ and MP7, where M is the number of basis functions. However, new CCSD(T) methods based on the so called divide-expand-consolidate (DEC) method have recently been reported showing linear scaling [36]. However, the discussion of these methods is beyond the scope of this thesis.

3.1.3 Density Functional Theory

As opposed to the wave function approaches described above, there is a whole class of methods using the electron density as variable. These were developed following two theorems proposed by Hohenberg and Kohn [37] in 1964 and a computational scheme developed by Kohn and Sham [38] in 1965. The first theorem states that the energy and other observables can be obtained from just the electronic density ρ, without knowledge of the wavefunction. The density is a function of the *x, y, z* coordinates, instead of the four coordinates for each electron as in the wave function based methods. The second theorem states that the energy of the ground state (GS) can be found variationally:

$$E[\rho_{tr}] \geq E_0 \text{ for any } \rho \text{ such that } N = \int \rho(\mathbf{r})\, d\mathbf{r} \tag{3.10}$$

where $E[\rho_{tr}]$ is the energy of a trial density, N is the number of electrons and E_0 is the exact energy of the GS. The energy functional can be written as the sum of three terms:

$$E[\rho] = \hat{T}[\rho] + E_{ext}[\rho] + E_{ee}[\rho] \tag{3.11}$$

where $\hat{T}[\rho]$ is the kinetic energy, $E_{ext}[\rho]$ is the external potential and $E_{ee}[\rho]$ is the electron-electron interaction. The $E_{ext}[\rho]$ is the electron-nuclei interaction and is determined by the system under study. The other two terms are universal, unfortunately their functional form is unknown.

The formalism proposed by Kohn and Sham is the one used in modern DFT implementations. It relies on a fictitious system of N non interacting electrons, where the V_{ee} is replaced by a mean field potential. The N electrons are expressed in terms of so-called KS orbitals:

$$\rho(\mathbf{r}) = \sum_i^N |\phi_i(\mathbf{r})|^2 \tag{3.12}$$

The kinetic energy of such system of non interacting electrons is:

$$\hat{T}_s[\rho] = -\frac{1}{2} \sum_i^N < \phi_i(\mathbf{r}) | \nabla^2 | \phi_i(\mathbf{r}) > \tag{3.13}$$

The Coulomb component represents a significant contribution to the electron-electron interaction and can be calculated for the non interacting system as:

$$E_H[\rho] = \frac{1}{2} \int \frac{\rho(\mathbf{r}_1)\rho(\mathbf{r}_2)}{|\mathbf{r}_1 - \mathbf{r}_2|}\, d\mathbf{r}_1 d\mathbf{r}_2 \tag{3.14}$$

The differences in kinetic energy and electron-electron interaction arising from the use of the non interacting system are grouped in the so-called exchange-correlation functional $E_{xc}[\rho]$:

$$E_{xc}[\rho] = \big(\hat{T}[\rho] - \hat{T}_s[\rho]\big) + \big(E_{ee}[\rho] - E_H[\rho]\big) \tag{3.15}$$

The energy functional becomes:

$$E[\rho] = \hat{T}_s[\rho] + E_{ext}[\rho] + E_H[\rho] + E_{xc}[\rho] \tag{3.16}$$

By using the second HK theorem (Eq. 3.10), the energy is minimised with respect to the density until $\frac{dE}{d\rho} = 0$. Since the density is parametrised in terms of orbitals, the condition becomes $\frac{dE}{d\phi} = 0$ and the set of equations that are solved in the KS-DFT approach is:

$$\left[-\frac{1}{2}\nabla^2 + v_{ext}(\mathbf{r}) + \int \frac{\rho(\mathbf{r}')}{|\mathbf{r}-\mathbf{r}'|}\, d\mathbf{r}' + v_{xc}(\mathbf{r})\right] \phi_i(\mathbf{r}) = \epsilon_i \phi_i(\mathbf{r}) \tag{3.17}$$

where the $v_{ext}(\mathbf{r})$ terms represents the electron-nuclei interaction. These are N coupled differential equations (one for each electron), linked by the fact that the ρ depends on the ϕ_i and the potential depends on ρ. There is, therefore, no closed form solution and the N Eq. 3.17 have to be solved self consistently by iteration.

The exchange-correlation potential $v_{xc}(\mathbf{r})$ is constructed from the derivative of the exchange-correlation energy with respect to the electron density:

$$v_{xc}(\mathbf{r}) = \frac{\delta E_{xc}[\rho]}{\delta \rho(\mathbf{r})} \tag{3.18}$$

The knowledge of the exact $E_{xc}[\rho]$ would give the exact ground state energy. However, this term must be approximated because its formulation is unknown.

DFT calculations approximate the functional dependency according to different methods that can be classified according to the degree of locality of the xc functional:

- Local Density Approximation (LDA)

  As the name suggests, in this approximation, the value of the $E_{xc}[\rho]$ only depends on the local value of the charge density ρ. The contribution of the exchange and correlation energies can be separated into $E_x^{LDA}[\rho]$ and $E_c^{LDA}[\rho]$. The former can be calculated exactly from the homogeneous electron gas and the latter has been derived from QMC calculations [39]. LDA performs better on systems where the electron density varies slowly, such as metals. Calculation of structural properties, vibrational frequencies and phase stability usually give satisfactory results even at this level of approximation. Its main drawback is the evaluation of binding energies that are underestimated. The good performance of LDA can be ascribed to error cancellation: exchange energies are usually overestimated by about 10%, whereas correlation energies are underestimated by about 200%. Good results are obtained because the former is, in general, one order of magnitude larger that the second one.

- Generalised Gradient Approximation (GGA)

  Under this approximation the $E_{xc}[\rho]$ depends both on the charge density and its first derivative. GGA improves the calculated values of binding energy with respect the the LDA.

- Meta-GGA

  This is an extension of the GGA where the functional depends also on the kinetic energy density $\tau(\mathbf{r})$. This contributes to delivering better results because of the extra degree of freedom introduced.

All the methods described above suffer from the so-called self interaction error. This error arises from the KS description of the electron density: each electron interacts with N electrons instead of N-1. A well known consequence of this error is that valence band are shifted at higher energies giving smaller band gaps in semiconductors. In order to correct this error, methods called hybrid functionals have been developed and are widely used. They are based on the introduction of some Fock exchange E_x^{Fock}, which is the exact exchange energy for the Slater determinant. This gives better results in the calculation of semiconductor and insulator band gaps [40].

This study focuses on metal surfaces that are properly described by the GGA. This level of approximation was, therefore, chosen for the calculations discussed in this thesis. Further details about the methods used can be found in Section 3.6.

3.2 Periodic Systems

In order to simulate properties of macroscopic samples (the order of magnitude is the Avogadro's number $N_A = 10^{23}$) a very large number of atoms should be considered. Although some cluster simulation of materials are used, this approach is impractical for the simulation of bulk and surface properties of materials that are not nanosized. In the simulation of crystals, a different approach consists of using the periodicity of the structure. This is divided into a set of lattice points that are the mathematical description of the crystal and a motif (or basis), which can be a single atom, ion or molecule that is found at every point of the lattice.

The lattice can be represented in a very compact way as a set of vectors $\mathbf{a_1}$, $\mathbf{a_2}$ and $\mathbf{a_3}$ called the direct space lattice vectors (the reason for specifying direct will be clarified in the following). Any point in the lattice can then be represented by a set of three integer numbers u, v and z. The three lattice vectors define the so-called unit cell. There are seven types of fundamental unit cells: cubic, tetragonal, orthorhombic, monoclinic, rhombohedral and hexagonal. The motif can occupy the corner, side or center of the unit faces. The combination of the fundamental unit cell and the positioning of the motif generate the fourteen Bravais lattices [41] that can be used to describe any crystalline structure.

To any of these Bravais lattices correspond a reciprocal lattice, which can be defined in many ways. The most intuitive one is a lattice whose lattice vectors ($\mathbf{b_1}$, $\mathbf{b_2}$ and $\mathbf{b_3}$) respect the following orthogonality constraint with respect to the direct one:

$$\mathbf{a}_i \cdot \mathbf{b}_j = \delta_{ij} \tag{3.19}$$

This requirement is satisfied if:

$$\mathbf{b_1} = \frac{\mathbf{a_2} \times \mathbf{a_3}}{V} \qquad \mathbf{b_2} = \frac{\mathbf{a_3} \times \mathbf{a_1}}{V} \qquad \mathbf{b_3} = \frac{\mathbf{a_1} \times \mathbf{a_2}}{V} \tag{3.20}$$

where V is the volume of the cell. The reciprocal lattice is a Bravais lattice itself and any point can be described by:

$$\mathbf{K} = \sum_{j}^{j=3} m_j \, \mathbf{b}_j \tag{3.21}$$

Another representation of the reciprocal lattice is as a FT of direct space lattice. Therefore, quantities that are more easily calculated in reciprocal space such as crystalline orbitals and densities can easily be transferred to direct space.

By using the periodicity of reciprocal space it is easy to show that all quantities can be calculated inside a region called *First Brillouin Zone* (FBZ). An infinite number of points in the FBZ should be used, in theory. However, the wavefunctions are continuous in reciprocal space and a finite set of $\mathbf{k}$ points can be used. In order to get accurate results, the number of these points must be checked by convergence tests.

As last concept of this section, the Bloch's theorem is introduced. Named after the Swiss physicist Felix Bloch, it states that: "*the wave function of an electron $\Phi_{i,\mathbf{k}}(\mathbf{r})$ in a periodic potential can be written as*":

$$\Phi_{i,\mathbf{k}}(\mathbf{r}) = e^{i\mathbf{k}\cdot\mathbf{r}} \cdot u_i(\mathbf{r}) \tag{3.22}$$

where $u_i(\mathbf{r})$ is a function characterised by the same periodicity of the unit cell ($u_i(\mathbf{r} + \mathbf{R}) = u_i(\mathbf{r})$, $\mathbf{R}$ is a vector of the direct space) and $e^{i\mathbf{k}\cdot\mathbf{r}}$ is a wavelike component and $\mathbf{k}$ is a wavevector of the reciprocal space. In the following section, two different ways to represent $u_i(\mathbf{r})$ are discussed.

3.3 The Basis Set Approximation

3.3.1 Local Basis Set

In order for methods used to approximate the Schrödinger equation to be implemented on computers, the HF or KS one-electron equations can be either represented on a grid or in terms of a basis set. This latter approach is the most efficient one. The orbitals are expressed as a linear combination of functions:

$$\psi_i(\mathbf{r}) = \sum_{\mu} a_{i,\mu}\, \chi_\mu(\mathbf{r}) \tag{3.23}$$

where $\chi_\mu(\mathbf{r})$ is a function of the basis set and $a_{i,\mu}$ is the weight in the orbital μ in the eigenstate $\psi_i(\mathbf{r})$. Although in theory the basis set should be infinite, this approach is not applicable in practice. Therefore, the basis set is truncated in order to include enough functions to give accurate results. Also, the variational theorem suggests that as the flexibility of the basis set is increased the energy will decrease and (eventually) converge. Many types of local functions can be used, they are usually centered on atomic sites. The most widely used are *Slater Type Orbitals* (STOs) and *Gaussian Type Orbitals.* (GTOs). There are advantages and drawbacks for both methods. The STOs present a cusp (as the electronic density) in correspondence of the nuclei and the exponential decay moving away from the nuclei is slower. The latter has zero derivative in correspondence of the nuclei and faster decays. However, Gaussian functions are more easily integrated since the derivative of a Gaussian function is still a Gaussian function. For this reason GTOs are the most widely used and it is computationally less expensive to include more GTOs in the basis set to obtain the correct behaviour of the electronic density, than using STOs.

Local basis set are the method of choice for the simulation of molecules, or in other words, non periodic systems. Methods to make local functions periodic are available and extremely useful to simulate materials where the electrons are localised and can be described in terms of atomic orbitals, such as ionic materials. In this case, in order to make the local orbital periodic, Bloch Functions (BF) can be used, they are defined as:

$$\phi_\mu(\mathbf{r}, \mathbf{k}) = \sum_{g} \chi_\mu(\mathbf{r} - \mathbf{r_A} - \mathbf{g}) e^{i\mathbf{k}\cdot\mathbf{g}} \tag{3.24}$$

where χ_μ is a local orbital in the primitive cell centered on the atom A. All lattice vectors $\mathbf{g}$ up to a certain cutoff are included. These Bloch functions represent the basis for the construction of the wavefunction as:

$$\Psi_i(\mathbf{r},\mathbf{k}) = \sum_{\mu} a^{\mathbf{k}}_{i,\mu}\phi_{\mu}(\mathbf{r},\mathbf{k}) \tag{3.25}$$

3.3.2 Plane Wave Basis Set

The natural choice for the simulation of periodic systems characterised by the presence of delocalised electrons are plane waves. Recalling the Bloch's theorem $\Phi_i(\mathbf{r}) = e^{i\mathbf{k}\cdot\mathbf{r}} \cdot u_i(\mathbf{r})$, the cell periodic part is expanded into a finite number of plane waves (PWs):

$$u_i(\mathbf{r}) = \sum_{K} a_{i,\mathbf{K}}e^{i\mathbf{K}\cdot\mathbf{r}} \tag{3.26}$$

The wavefunction becomes:

$$\Psi_i(\mathbf{r},\mathbf{k}) = \sum_{\mathbf{K}} a_{i,\mathbf{k}+\mathbf{K}}e^{i(\mathbf{k}+\mathbf{K})\cdot\mathbf{r}} \tag{3.27}$$

In theory an infinite number of plane waves should be used. However, one of the advantages of the PW approach is that the accuracy of the calculation increases with the number of plane waves. It is therefore possible to truncate the summation according to a convergence procedure and select only the plane waves whose kinetic energy is below a defined cutoff:

$$E_{cut} \geq \frac{1}{2}|\mathbf{k}+\mathbf{K}|^2 \tag{3.28}$$

One of the PW basis set drawbacks is that very high energy waves must be included to describe the core electrons. This increases the number of **K** vectors to include in Eq. 3.28 and the computational cost. To avoid this, pseudopotential can be used to describe the core electrons.

3.3.3 Pseudopotential

The description of inner shell electrons can require the use of too many PWs. Also, the core electrons are not modified by the formation of chemical bonds and can be assumed to remain as they are in isolated atoms. How many electrons to include in the inner and outer shells must be carefully checked in order not to exclude electrons that actually take part in the bond formation. Once this separation has been determined, the nuclear potential $E_{ext}[\rho]$ in Eq. 3.16 can be modified in order to include the nucleus potential screened by the core electrons. The KS equations are then solved only for the valence part of the wavefunction.

The PW-PP approach is the most widely used in the simulation of metals and has been selected for this work.

3.4 Surface Modelling

Throughout the first part of this chapter the discussion was focused on bulk 3D properties. Although the bulk model can be successfully used to describe many properties, also surfaces are of great importance in materials science. Two methods to simulate surfaces are available:

- Cluster Approach

  A cluster of a fixed number of atoms is cut from the bulk. Different shapes and sizes of the cluster can be selected. The most common choice is using a Wulff construction [42] (see Section 3.5 for details on the Wulff construction) to determine the shape of a nanoparticle of a selected material and cut a cluster of the same shape. This approach is successfully used, but the results strongly depend on the size and shape of the cluster and several convergence tests must be carried out. Also, termination of the surfaces must be carefully checked in order not to have unphysical geometries without modifying the surface structure.

- Slab Approach

  According to this approach, a thin slab of material (usually tens of Å is cut form the bulk by using the Miller indices (h k l) of the plane of interest. The slab is periodic in the two directions parallel to the plane and has finite thickness along the direction perpendicular to the plane. An example of slab is depicted in Fig. 3.1. On the left hand side the unit cell is shown and on the right hand side the effect of 2D translational symmetry on such unit cell. If local BS sets are used, 2D periodic cells can be used. If PW basis sets are employed, the cell must be periodic in the three dimensions because of the 3D Fourier representation of quantities inherent in the PW approach. In this case a cell containing a portion of empty space between slabs is used. This results in an array of slabs and the distance among them must be large enough to have negligible interaction between neighbouring slabs. This is achieved through convergence tests. This was the method chosen for this study.

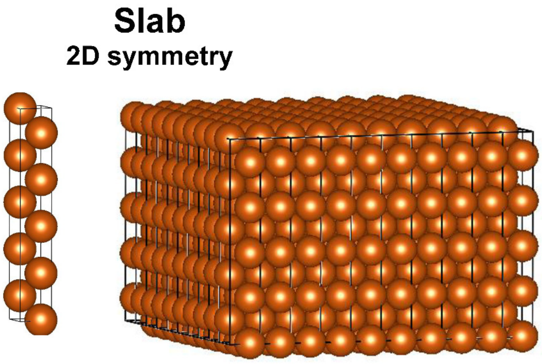

Figure 3.1: Left: primitive cell used to model a Cu (111) surface 10 layer slab. Right: the effect of translational symmetry on the primitive cell.

3.5 Properties

Band Structure and Surface Projected Band Structure

The band structure is a concept that arises from the Bloch's Theorem, where the wavefunction depends on two indices i and $\mathbf{k}$ as opposite to molecular calculations, where the energy of the MO only depends on the i index. In periodic simulations, the calculations are performed on the primitive cell and its interaction with all the other cells of the infinite crystal (or inside a sphere determined by the cutoff criteria) are included in the $\mathbf{k}$ term. The energy is continuous in $\mathbf{k}$ and discreet in i. Band structure diagrams are plotted as energy vs $\mathbf{k}$ index. They can also be calculated for lower dimensionality systems, such as slab models, but only along the periodic directions.

The comparison of the surface electronic structure with the bulk one is very useful to highlight changes arising from the perturbation introduced by the surface. Comparing a bulk and a surface band structure is not straightforward: the surface contains a larger number of atoms (and of electrons as a consequence) and could be seen as a supercell along the non periodic direction. The electronic states are "folded" in a supercell. There is a way to obtain a bulk band structure that can be directly compared to the surface one: the so-called surface projected band structure (SPBS). A brief description of the technique used to obtain the SPBS can be found in [43]. The detailed procedure in terms of rotation matrices, used in this study to calculate the SPBS and the coordinate of the $\mathbf{k}$ points used in the following can be found in Appendix A. The bulk electronic states are defined within the FBZ of the bulk crystal as $\epsilon_i(\mathbf{k}) \equiv \epsilon_i(\mathbf{k}_{||}, k_\perp)$ where $\mathbf{k}_{||} \equiv (k_x, k_y)$ and $k_\perp \equiv (k_z)$. The electronic states of the

2D periodic slab are defined within the FBZ of the surface unit cell as $\epsilon_i(\mathbf{k}_{||})$, where $\mathbf{k}_{||} \equiv (\mathbf{k_x}, \mathbf{k_y}, 0)$. In the calculation of the SPBS the same path chosen for the slab is used in the bulk calculation. This is achieved by creating a rotated bulk cell with two vectors in the surface plane in order to define suitable $k_\perp$, which is sampled at different values and the different $\bar{\epsilon}_i(\mathbf{k}_{||}, k_\perp)$ are reported at $\mathbf{k}_{||}$. An example of surface projected band structure of copper (111) and (100) surfaces in the region around $\mathbf{\Gamma}$ is reported in [44].

By comparing the SBS and the SPBS, new states can be found in energy gaps of the SPBS. These are the surfaces states. Another way to identify the surface states is through the PDOS discussed in the following.

Density of States and Projected Density of States

The Density of States (DOS) quantifies how many states can be found in a selected energy interval:

$$DOS(E) = \frac{2}{V_{BZ}} \sum_i \int_{BZ} \delta(E - \epsilon_i(\mathbf{k})) d\mathbf{k} \tag{3.29}$$

where the integration is over the volume of the FBZ. The contribution of each atomic (or pseudoatomic orbital if PW are used) to the wavefunction can be calculated as:

$$PDOS(E) = \frac{2}{V_{BZ}} \sum_i \sum_\nu \int_{BZ} c^*_{i,\nu}(\mathbf{k}) c_{i,\nu}(\mathbf{k}) S_{\mu\nu}(\mathbf{k}) \delta(E - \epsilon_i(\mathbf{k})) d\mathbf{k} \tag{3.30}$$

$c_{i,\mu}(\mathbf{k})$ and $c_{i,\nu}(\mathbf{k})$ are the coefficients of the eigenvector $\phi_i(\mathbf{k})$ with energy ϵ_i and $S_{\mu\nu}(\mathbf{k})$ is the overlap between the two AO (μ and ν). Each AO is labelled according to the atom where it is centered. By summing the contribution of all the AO of the atomic site A, the weight of the atom A on the wavefunction (specified i and $\mathbf{k}$) can be obtained. Therefore, a layer-by-layer PDOS of a slab can be plotted, an example of this are Fig. 5.3, 5.4 and 5.5. Also, by combining the information of the PDOS and the band structure, the states where the contribution of the top most layer is higher than a fixed threshold can be highlighted as the surface states (an example of this can be found in the above mentioned figures). This latter approach has the advantage, with respect to the PDOS, of being able to visualize the coordinate in $\mathbf{k}$ space where the surface state is, which is relevant in PE simulations reported here because of the constraint on the electron momentum discussed in Section 4.2.1.

Surface Energy

The surface energy is a measure of the perturbation introduced by the surface on the bulk structure. The E_{surf} can be calculated in two ways [45]:

$$E^{(1)}_{surf} = \frac{1}{2}\{E_{slab}(n) - [E_{bulk} \times (n)]\} \tag{3.31}$$

$$E^{(2)}_{surf} = \frac{1}{2}\{E_{slab}(n) - [E_{slab}(n) - E_{slab}(n-m)]\frac{n}{m}\} \tag{3.32}$$

Where $E_{slab}(n)$ is the total energy of the slab, E_{bulk} is the energy of the bulk cell and n is the number of atoms in the slab. The surface energy is one of the parameters that are used to test the convergence on the slab thickness. Eq. 3.32 has the advantage of a systematic error cancellation. However, it exhibits strong oscillation of the surface energy at increasing number of layers with respect to Eq. 3.31, as discussed in Ref. [46]. Therefore, in this work, Eq. 3.31 was used to calculate the surface energy of the slabs.

Work Function

The work function of a metal is the lowest energy needed to extract an electron from a particular surface. It corresponds to the energy difference between the Fermi energy and the vacuum level. In 2D periodic calculations, the vacuum level corresponds to the zero of the potential and the Fermi energy is, therefore, the WF. Instead, in PW calculations, where a 3D periodic cell must be used, the constant value of the potential between neighbouring slabs is used as zero of the potential. This value must be constant at the centre of the vacuum region. This is also a way to test the thickness of the vacuum region is large enough.

Wulff Construction

The Wulff construction [42, 47] can be used to determine the equilibrium shape of a crystallite of material. The method is based on the so-called Gibbs-Wulff theorem, which states that the length of a vector normal to a crystal plane is proportional to its surface free energy:

$$l_i = c_i \gamma_i \tag{3.33}$$

where l_i is the length of the vector, c_i is the proportionality factor and γ_i is the Gibbs free energy of the facet i. In this work, the Gibbs free energy was approximated through the surface energy as calculated in Eq. 3.31.

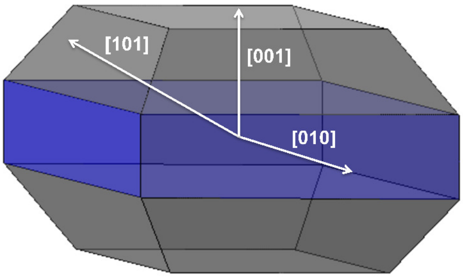

Figure 3.2: Example of a Wulff construction for an hcp system. The arrow are labelled according to the directions in the crystal.

An example of Wulff construction for an hcp crystal is reported in Fig. 3.2. The arrows are labelled according to their direction in the crystal. Crystal facets characterised by higher surface energy will grow faster, resulting in a smaller presence in the crystal surfaces. From the morphology of the crystallite an estimate of the surface area of each facet present in a polycrystalline sample can be calculated and facet dependent properties (such as WF and QE) can be averaged.

3.6 Computational Details

All the calculations reported in this thesis were based on DFT and after testing several approximations of the exchange-correlation functional, the PBE [48] functional was chosen. The CASTEP [49] software package was used. This code expands the wave function by means of PW and the core electrons are described through the PP approach. This code offers the possibility to generate the PP on-the-fly based on the method proposed by D. Vanderbilt [50].

The E_{cut} of the PW was tested on the bulk and slab cells. The variation in the total electronic energy per atom of the order of 10^{-5} eV was found for a plane wave energy cutoff of 500 eV. Sampling of the reciprocal space was performed according to a Monkhorst-Pack [18] sampling of the Brillouin zone (BZ). Convergence on the total energy (variations lower than 10^{-5} eV) are found for a sampling of 14 along each periodic direction for the bulk primitive cells. The slab cells are sampled along the periodic directions and only on one point along the direction perpendicular to the surface. For the surface primitive cells a sampling of 14 along the periodic directions was used. In the supercell calculations, the sampling is decreased according to the size of the cell (for example, in a 2x2 supercell a sampling of 7 will be sufficient to represent the accuracy of 14 in the primitive cell).

DFT calculations are performed at a temperature of 0 K. However, to facilitate convergence of the electronic states a smearing factor is introduced. This simulates the effect of temperature and allows electrons close to the Fermi level to occupy the lowest states of the conduction band. A smearing factor of 300 K has been used in this work.

Geometry optimisation was performed on all structures reported here by using the BFGS method [51–54]. Tolerance on the geometry optimisation is set to be lower than 10^{-5} eV/atom. For the bulk structures, the primitive cells are optimised by allowing the lattice parameter to vary. For the slab cells, the lattice parameters are kept fixed to the bulk optimised one and the position of atoms inside the cells are allowed to change. This is the standard approach when surface are simulated through the slab approach.

The adsorption energy of the external species was calculated with respect to their standard state: bulk for cesium and diatomic molecules (H_2 and O_2) for hydrogen and oxygen.

The thickness of the slab must be carefully converged with respect to variations of the total and surface energy, the geometry and electronic structure of the central layers. Also, the slab must be thick enough in order for these parameters not to be changed by the adsorption of external atoms or surface reconstruction. For the 10 layer slab, the displacement of the central layer is found to be less than 0.1% of the bulk interlayer spacing. Furthermore, the electronic structure of the central layers of the slab, calculated using the projection of the density of states (PDOS) on the central atoms, reproduces that of the bulk crystal. This demonstrates that the mean field potential in the centre of the slab replicates that in a layer of the bulk crystal. Adsorption of oxygen, hydrogen or cesium to the surface of the Mg (0001) ten layer slab (discussed in Chapter 7.4) produces negligible changes in the displacement and electronic structure of the central layer. These tests suggest that the 10 layer slab model is adequate for the study of changes in the QE due to surface modifications.

4

Photoemission Theories

Several photoemission theories have been developed in order to explain experimental data. They can be divided into two main groups: three step and one step theories. The main characteristics and differences between the two are briefly presented in this introductory section and discussed in more details in this chapter. The original formulation of the three step and one step models were proposed by C.N Berglund and W.E. Spicer [55] in 1964 and by J.B. Pendry [56] in 1976, respectively.

The Fermi golden rule can be seen as the starting point for both theories, as it is represented in Fig. 4.1. It describes the transition probability between two electronic states, where I refer to the initial and F to the final states, respectively. The generic operator Δ is the matrix element giving the probability for the coupling between the two states. The main difference between the two theories discussed here is how many steps are used to describe the photoemission process. According to the three step model (3SM), the photoemission process can be divided into three processes: excitation of an electron upon photon absorption, transport of the excited electron from the bulk to the surface and escape from the surface. These processes are considered to be independent and the probability for the three can be multiplied in a final expression for the emission probability. On the contrary, in the one step model (1SM), the three processes described above are represented by a single coherent quantum mechanical process. The operator Δ combines the probability for the three steps and the final state, which is a Bloch state in the original formulation of the 3SM and a time - reversed LEED state in the 1SM. This latter condenses all the scattering phenomena in the bulk and surface escape.

The 3SM gives satisfactory results for valence level spectroscopy, identifying the energy levels of the material at specific emission angles of the electrons, at the same time, the 1SM model is able to reproduce the intensity of the experimental peaks in photoemission experiment at a higher degree of accuracy. This is because the three steps do interfere with each others and this is taken into account in the 1SM.

The 1SM is, therefore, considered the state of the art in terms of photoemission simulations. However, in its original formulation and some further developments, the 1SM relied on the Green function methods in the KKR formalism [57]. These use the muffin-tin potential in the atomic sphere approximation. In this approximation, the potential of the materials is described by non overlapping (or slightly overlapping [57]) spheres centered on the atomic sites and a constant potential in the interstitial region, usually expanded in plane waves. This procedure efficiently describes the potential in the areas near the nuclei, but lacks a proper description in the interstitial region. Some recent developments are based on full potential calculations [58] (see Section 4.1 for further details).

Condensing the three steps for photoemission in one coherent quantum mechanical process is considered an advantage. However, this work aims at developing a method to systematically improve the efficiency of photocathode materials. In order to achieve this, it is fundamental to be able to disentangle the effect of alterations of the pristine material in terms of WF variations, addition or shift of states in the electronic structure and change in optical properties. In its formulation, the three step model, despite being theoretically less accurate than the one step model provides the perfect candidate as starting point. In its original formulation, however, it is based on bulk calculations. In order to include surface effects in the emission process, an extension of the 3SM is presented in the following, after a short discussion of the 1SM.

4.1 The One Step Model

The differences between the 1SM and 3SM were highlighted in the introduction to this chapter. In Pendry's formulation of photoemission, the photocurrent is derived from Fermi's golden rule:

$$I(\epsilon_f, \mathbf{k}_{||}) \propto \sum_j | < \epsilon_f, \mathbf{k}_{||} | \Delta | \epsilon_i, \mathbf{k} > | \tag{4.1}$$

where ϵ_f is the energy of the final state, *i.e.* upon absorption of the photon energy and ϵ_i is the initial state. $\mathbf{k}_{||}$ is the parallel component of the electron momentum, which is conserved during the transition from the k point $\mathbf{k}$. The electron-photon interaction is included in the Hamiltonian as:

$$\Delta = \frac{1}{2c}(\mathbf{p} \cdot \mathbf{A} + \mathbf{A} \cdot \mathbf{p}) \tag{4.2}$$

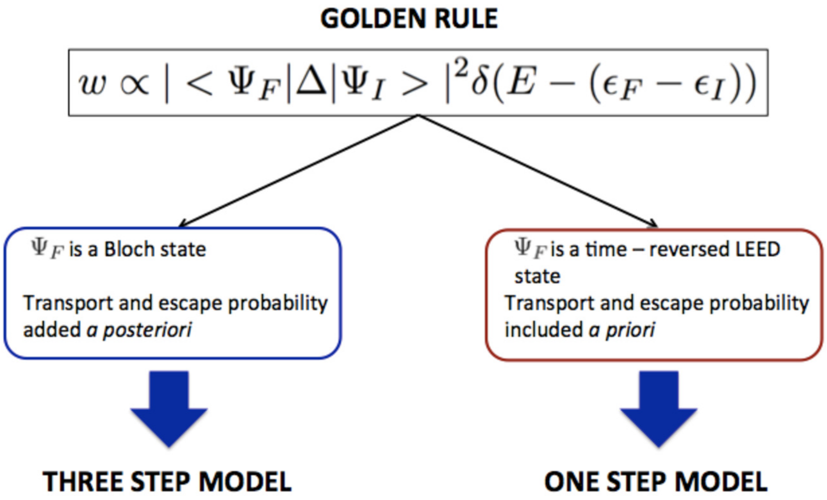

Figure 4.1: Differences between the two main photoemission theories.

$$\mathbf{A} = \mathbf{a}\ cos(\mathbf{q} \cdot \mathbf{r} - \omega t) \tag{4.3}$$

In order to consider the scattering states the electron couples with, to exit the crystal, a generalised form of the golden rule in terms of the retarded G^- and advanced G^+ Green's functions can be written as:

$$I(\epsilon_f, \mathbf{k}_{||}) = \frac{1}{\pi} Im < \epsilon_f, \mathbf{k}_{||}|G_2^+ \Delta G_1^+ \Delta^+ G_2^-|\epsilon_f, \mathbf{k} > \tag{4.4}$$

where the state of the electron at the detector is defined by its energy and momentum ϵ_f and $\mathbf{k}_{||}$. The retarded Green's function G introduces all the multiple-scattering properties of the materials at the final energy ϵ_f.

The first full-potential theory, which means the potential is not restricted the muffin tin method, was proposed in 1995 by Braun and coworkers [58, 59]. Relativistic effects have also been proposed as an extension to the original one step model [60] and become relevant when core electrons are studied.

As discussed in the introduction to this chapter, the method chosen for the simulations reported in this thesis is the three step model because of it represents a pragmatic approach when seeking to isolate the effects of surface chemistry in order to optimise photocathodes. Therefore, the extensions to the one step model of photoemission are beyond the purpose of this thesis and the discussion will move to the three step model and the inclusion of surface effects in its original formulation.

4.2 The Three Step Model

The three step model for photoemission was originally proposed by Berglund and Spicer [55, 61–64]. In this theory, the photoemission is regarded as the sequence of three independent processes: the optical excitation of an electron upon absorption of a photon with energy $\hbar\omega$, the transport of the excited electron to the surface and the escape of the electron through the surface barrier. The three steps are assumed to be independent and thus the distribution of photoexcited electrons is a simple product of the probability of each step contributing to the photoexcited flux:

$$I(E,\omega) = P(E,\omega)\,T(E)\,D(E) \tag{4.5}$$

where $P(E,\omega)$ is the distribution of photoexcited electrons of the bulk at photon energy $\hbar\omega$, $T(E)$ is the transmission function from the bulk to the surface and $D(E)$ is the escape function.

The absorption of a photon excites an electron from the valence band to the conduction band. Electrons excited above the vacuum energy are able to escape from the surface. If the excitation occurs to a conduction state that is below the vacuum energy, the electron will be thermally de-excited to the valence band.

After excitation the number of electrons transported to the surface is reduced by the inelastic electron-electron scattering. When assuming an isotropic scattering probability that only depends on the energy of the excited electron, the inelastic mean free path approximation can be used [64]. The 3SM, in its original formulation, assumes the excitation occurs in the bulk and the probabilities for the three steps depend only on the energy of the electron and the photon and not on the position of the electron in the material. However, for the purpose of understanding the relationship between surface structure and photoemission, it is here extended to surface simulations as discussed in the next section.

4.2.1 Extension And Implementation For Surface Modelling

Extending the 3SM to an explicit model of the surface electronic structure allows for a direct dependence of the escape probability on the depth inside the material where the excitation occurs.

The three steps are now discussed in details, including a fourth one, called here the step 0, which is the layer-by-layer decomposition of the electronic structure. This concept is needed in order to introduce a z-dependence of the properties used to calculate the photoemission in the formalism presented in this work.

Step 0: Layer-by-layer Decomposition of the Electronic Structure

Electron states are delocalised in crystals. However, an attempt to weight the emission probability by the depth of the electron in its initial state requires the localisation of the electronic states. The weights can be calculated according to several theoretical frameworks. Among these, the projection onto contributions from atom centered functions, such as AO or Wannier Functions [43, 65] is commonly used. In this work, the weights $W(i, A, \mathbf{k})$ were calculated by using the projection onto the AO used in the construction of the pseudopotential:

$$W(i, A, \mathbf{k}) = \sum_{\mu \in A} \sum_{\nu} c^{*}_{i,\nu}(\mathbf{k}) c_{i,\nu}(\mathbf{k}) S_{\mu\nu}(\mathbf{k}) \tag{4.6}$$

where i and A are the band and atom indices, respectively. The coefficients $c_{i,\nu}(\mathbf{k})$ and the overlap matrix $S_{\mu\nu}(\mathbf{k})$ are the same used to calculate the PDOS in Eq. 3.30 and discussed in Section 3.5. The contribution of each atom is obtained as a summation over all the orbitals μ centered on A.

The $W(i, A, \mathbf{k})$ is also used to calculate a layer-by-layer decomposition of the band structure. This procedure allows for an identification of the surface states in the band structure of the materials. This is done by highlighting in red the states characterised by a $W(i, A, \mathbf{k})$ (where A is an atom of the topmost layer of the slab) greater than a fixed threshold in the band structure (examples of this are reported in Fig. 5.3 to 5.5). This is a complementary approach to the PDOS, which is obtained as a summation over all the weights in a range of energy (see Eq. 3.30 in Section 3.5). In the photoemission theory discussed here, the band and $\mathbf{k}$ dependence are used in order to calculate all the layer-by-layer properties, such as light absorption, in order to obtain a layer-by-layer photoemission spectrum.

Step 1: Optical Excitation

The first step of the 3SM is the absorption of a photon with energy $\hbar\omega$. This energy is transferred to an electron, which is excited from the initial state i in the valence band to the final state f in the conduction band. While a crystalline orbital computed in the periodic potential of the lattice gives the best description for the initial state, the final state could be represented in different ways. For example, a plane wave would give a good description of the electron at a distance where the surface potential becomes weak, but it would not be accurate in the near surface region. If an inverse LEED state were used, the coupling would be with a scattering state that decays into the bulk and the same formalism of the 1SM would be applied. In this work, the final state is represented by a high energy crystalline orbital computed in the periodic potential of the lattice. The probability for the transition is the the square of the optical matrix element (OME), which accounts for the coupling of the valence band i and the conduction band f:

$$M(i, f, \mathbf{k}) =< \psi_{f,\mathbf{k}}|\mathbf{u} \cdot \mathbf{r}|\psi_{i,\mathbf{k}} > \tag{4.7}$$

where $\mathbf{u}$ defines the polarization of the electric field of the incident light and $\mathbf{r}$ is the momentum operator. Because of the near zero momentum of the photon, only vertical transitions (involving states belonging to the same $\mathbf{k}$ point) are considered.

A delta function is used to ensure the energy conservation. Transitions can only occur if the energy between the two states is equal to the photon energy:

$$\delta(E - (\epsilon_{f,\mathbf{k}} - \epsilon_{i,\mathbf{k}})) \tag{4.8}$$

The dielectric function describes the interaction of an electromagnetic field and a material [66]. It is a complex number that can be written as

$$\varepsilon = \varepsilon_1 + i\varepsilon_2 \tag{4.9}$$

A DFT approximation to the imaginary part of the dielectric function (ε_2) can be calculated in the random phase approximation [66] from first principles from the Kohn Sham orbitals as:

$$\varepsilon_2(E) = \frac{\pi e^2}{\varepsilon_0 V} \sum_i \sum_f \int_{BZ} | < \psi_{f,\mathbf{k}}|\mathbf{u} \cdot \mathbf{r}|\psi_{f,\mathbf{k}} > |^2 \delta(E - (\epsilon_{f,\mathbf{k}} - \epsilon_{i,\mathbf{k}}))d\mathbf{k} \tag{4.10}$$

where e is the electron charge, ε_0 is the vacuum permittivity and V is the volume of the unit cell.

In order to obtain a layer-by-layer decomposition of the optical properties the weight $W(i, A, \mathbf{k})$ is introduced in Eq. 4.10:

$$\varepsilon_2(E, l) = \frac{\pi e^2}{\varepsilon_0 V} \sum_i \sum_f \sum_{A \in l} \int_{BZ} | < \psi_{f,\mathbf{k}}|\mathbf{u} \cdot \mathbf{r}|\psi_{f,\mathbf{k}} > |^2 \delta(E - (\epsilon_{f,\mathbf{k}} - \epsilon_{i,\mathbf{k}}))W(i, A, \mathbf{k})d\mathbf{k} \tag{4.11}$$

where the third summation symbol sums over all atoms A belonging to the layer l in order to obtain a layer-by-layer decomposition rather than an atom-by-atom decomposition. This becomes relevant for calculations where more than one atom is present in the same layer.

The layer by layer decomposition of the real part of the dielectric function (ε_1) is calculated through the Kramers-Kronig relations [67] and it is layer-by-layer decomposed as the ε_2.

The layer by layer decomposition of the refractive index N may then be computed as:

$$N(E,l) = n(E,l) + ik(E,l) \tag{4.12}$$

where the layer dependence was introduced through the dielectric function as follows:

$$n(E,l) = \frac{1}{2}\left[\varepsilon_1^2(E,l) + \varepsilon_2^2(E,l)\right]^{\frac{1}{2}} + \varepsilon_1^2(E,l)^{\frac{1}{2}} \tag{4.13}$$

$$k(E,l) = \frac{1}{2}\left[\varepsilon_1^2(E,l) + \varepsilon_2^2(E,l)\right]^{\frac{1}{2}} - \varepsilon_1^2(E,l)^{\frac{1}{2}} \tag{4.14}$$

The optical absorption coefficient (units of m^{-1}) quantifies the portion of electromagnetic radiation absorbed by a portion of material:

$$\alpha(E,l) = \frac{2k\omega}{c} \tag{4.15}$$

where k is the imaginary part of the refractive index, ω is the frequency of the light at energy E and c is the speed of light. The value of $\alpha(E,l)$ is expected to be quite homogeneous for a thick slab of pure material (some differences could appear for the surface layer because if its perturbation on the electronic structure), but should change quite dramatically in presence of adsorbates or interfaces.

As the light beam travels through the material, it is absorbed by the upper layers of the slab. The intensity of light reaching a layer can be easily calculated through the Beer-Lambert law [31]:

$$I(E,l) = I(E,l-1)\, e^{-\alpha(E,l)t(l)} \tag{4.16}$$

where l is the layer label and $l-1$ is the layer above l, $t(l)$ is the thickness of the layer l. The portion of light reaching a certain layer, or in other terms, the number of photons will decrease as the beam travels through the material. Therefore, excitation from layers deep inside the slab will be lower than from the surface ones. However, this term is usually one order of magnitude larger [62, 63] than the electron escape depth, which is discussed in the next section.

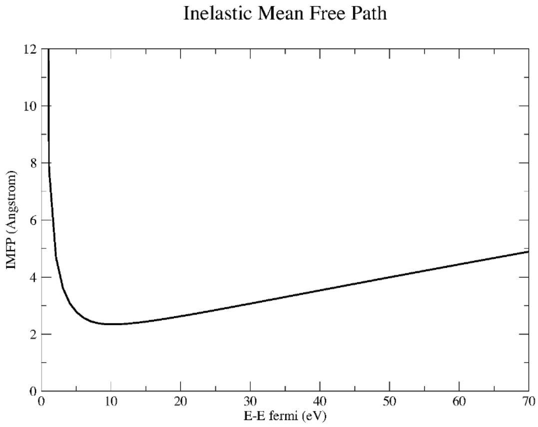

Figure 4.2: Example of IMFP curve.

Step 2: Transport to the Surface

Excited electrons can travel to the surface. As they do so they can undergo elastic and inelastic scattering with other excited and ground state electrons. This changes the direction and energy of the scattered electrons. Several theories about the inelastic scattering of electrons are available [68–72].

An explicit model of all the possible loss processes is beyond the scope of the current work. It is, however, possible to estimate the overall loss function and its energy dependence through a simple model based on the assumption that there is an average distance electrons travel in a material before an inelastic scattering event occurs. This distance is evaluated in electron energy-loss spectroscopy through an approach equivalent to the Lambert-Beer equation for light absorption:

$$I(d) = I_0 e^{\frac{-d}{\lambda(E)}} \tag{4.17}$$

where I_0 is the intensity of the beam reaching the surface, d is the distance inside the material, E is the photon energy and $\lambda(E)$ is the inelastic mean free path (IMFP). This latter gives the attenuation of the electron beam according to its energy, or in other words, the distance an electron beam can travel before its intensity is reduced to $1/e$.

It has been observed that the $\lambda(E)$ parameter can be described by a universal curve [73], which has the same shape for all materials, but different values for the positioning of the minimum. This curve is calculated from the imaginary part of the self energy as described in Ref. [73]. An example of this curve, for copper is reported in Fig. 4.2 calculated by using the approach described in [74].

The IMFP is slowly varying in the region of the minimum. Since this is the energy of the electrons giving near threshold emission (*i.e.* excitation at energy values just above the WF) for the substrates discussed in this work (see Section 6.3) in what follows the energy dependence has therefore been neglected and a constant IMFP was adopted for each substrate. This value was calculated as the average of the experimental and *ab initio* values found in literature [68–72]. These are 5.54 Å for copper, 6.13 Å for silver and 5.00 Å for magnesium.

Within this approximation the the probability for an electron to be emitted decreases exponentially with its depth inside the slab according to:

$$esc(E,l) = e^{\frac{-d(l)}{\lambda(E)}} \tag{4.18}$$

where $d(l)$ is the depth inside the slab where the electron is being excited.

Step 3: Escape from the Surface

The dominant factors determining the escape of excited state electrons from the surface are the work function and the value of the electronic momentum perpendicular to the surface which is constrained by momentum conservation in the initial excitation.

The electrons that reached the surface will escape from the sample if their energy is higher than the surface barrier. The height of the effective surface barrier is the difference between the energy of the electron and the work function of the surface (see Section 3.5 for the theory and details of the WF calculation). This is taken into account, in the final equation for photoemission, by summing over the final states whose energy is higher than the WF. Electrons can also be excited to the conduction band in the region below the WF energy, but they will be thermally de-excited instead of emitted.

The second factor to be considered is the conservation of the electron momentum. To a good approximation, the parallel component of the momentum is conserved during the emission [75, 76]:

$$(\mathbf{k}_{\parallel} + \mathbf{K}_{\parallel}) = \mathbf{q}_{\parallel} \tag{4.19}$$

where $\mathbf{k}$ and $\mathbf{q}$ are used to label the momentum of the electron inside the surface and in the vacuum, respectively. $\mathbf{K}_{\parallel}$ is a lattice vector of the reciprocal space, which has only parallel components. This compact notation $(\mathbf{k}_{\parallel} + \mathbf{K}_{\parallel})$ is used to highlight the fact that electrons, due to excitations at $\mathbf{k}$-vectors that are at higher order Brillouin Zones (BZ), are emitted at the same angle as the equivalent electrons in the First Brillouin Zone (FBZ).

The momentum component along the direction perpendicular to the surface $k_\perp$ (that here is assumed to be the z axis) is zero inside the slab because it has no periodicity along such direction. Since the $\mathbf{k}_\parallel$ is conserved during the transition, the energy absorbed from the photon will be transferred to the $k_\perp$ component and varies according to the energy of the final state E_f. The momentum component along the direction perpendicular to the surface upon excitation *i.e.* outside the slab $q_\perp$ is determined by the conservation of energy such that:

$$E_f = \epsilon_f(\mathbf{k}_\parallel, k_\perp) - E_v = \frac{\hbar^2}{2m}(\mathbf{k_\parallel^2} + q_\perp^2) \tag{4.20}$$

where the final energy E_f is equal to the energy of the final state above the vacuum energy ($\epsilon_f(\mathbf{k}_\parallel, k_\perp) - E_v$) and E_v is the vacuum energy. By rearranging Eq. 4.20, the value of $q_\perp$ can be determined:

$$q_\perp = \sqrt{\frac{2m}{\hbar^2}\left[\epsilon_f(\mathbf{k}_\parallel, k_\perp) - E_v\right] - {\mathbf{k}_\parallel}^2} \tag{4.21}$$

If the $q_\perp$ component is imaginary the electron is absorbed by the crystal and does not contribute to the quantum efficiency. This highlights an important feature of photoemission which is that the lower the final energy of the excited electron (*i.e.* the photon energy), the higher is the contribution to the QE from $\mathbf{k}$ points close to Γ because electrons with larger components along the x and y directions will not be emitted but absorbed by the substrate [77]. This effect can be observed in Fig. 6.1 to 6.3 where the states from where electrons can be emitted, at photon energy of 4.7 eV, are highlighted on the BS and PDOS.

The constraint on the electron momentum is taken into account in the equation for QE by means of a Heaviside step function:

$$H(q_\perp > 0) \tag{4.22}$$

reflecting the fact that that only final state electrons characterised by a positive momentum along the direction perpendicular to the surface contribute to the QE.

The effect of this restriction on the electron momentum is schematically shown in Fig. 4.3, where electrons excited from the same $\mathbf{k}$ point (same k_x and k_y) at three different photon energies is represented. E_{f1} is notionally sufficient energy to overcome the work function, but its $q_\perp$ component, calculated according to Eq. 4.21 is imaginary. This means that upon excitation, the electron is reflected inside the surface.

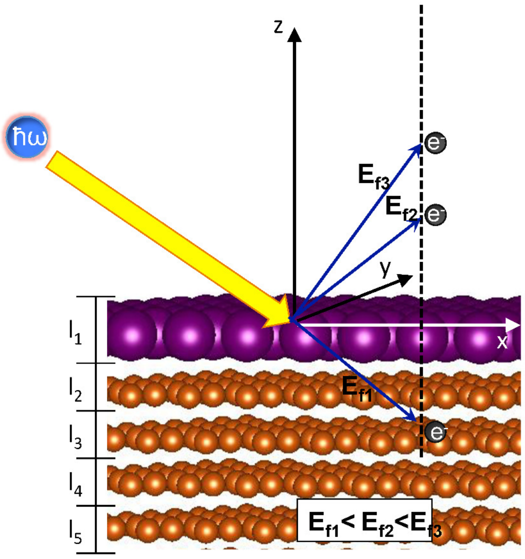

Figure 4.3: Schematic representation of the effect of the conservation of the momentum parallel to the surface during the electron emission.

E_{f2} provides a positive $\mathbf{q}_{\perp}$, which means the electron is emitted from the surface. The higher the E_f becomes, the closer to the z axis the electron is travelling (compare E_{f3} and E_{f2} in Fig. 4.3).

Through simple geometric considerations, the angle of emission can be calculated by knowing the value of $q_{\perp}$ and the total momentum $\mathbf{q}$. The maximum angle of emission for a fixed photon energy can be used to calculate the emittance of the electron beam. A. Schröder and coworkers have recently used simple arguments based on the effective electron mass, which reflects the curvature of the band to efficiently screen materials according to their predicted emittance [78, 79]. The same procedure can easily be included in the theory described here with two purposes: computing the angle resolved photoemission spectra (ARPES) and the emittance of the electron beam. Both these aspects will be implemented in the future of the project (see Chapter 10).

The Cell Invariance Problem

The constraint of the momentum described above can be used when primitive cells (for the surface, see Section 3.4) are used. In the simulation of low coverage of adsorbates supercells must be used. As the dimension of the direct lattice cell increases, the reciprocal space cell decreases accordingly to Eq. 3.20. This phenomenon is very well known [80] and can be described in terms of electronic states folding (or translation).

Most properties, such as DOS and optical properties are not affected by the bands folding because they are integrated over the BZ. However, it influences the PE spectra because of the constraint on the electron momentum. This depends directly on the coordinate of the **k** point from where the electron is emitted through Eq. 4.20 and 4.21. The higher the order of the supercell, the higher the emission, in particular at low photon energy because of the higher number of states folded at $\mathbf{\Gamma}$.

Techniques to identify which are the states that were folded are available [81–84]. They are based on the fact that the folded states undergo an antisymmetrization that is not present in the primitive cell.

These unfolding methods have not been implemented yet in the procedure used to obtain the results discussed in this thesis. Therefore, the momentum constraint has been applied to the calculations where the primitive cell could be used (clean surfaces). For the calculations where supercells had to be used, the constraint on the momentum was ignored and all electrons in the BZ are considered as being emitted from $\mathbf{\Gamma}$. This approximation can be used if variations in QE between clean and modified surfaces are discussed.

4.2.2 Equation for the Quantum Efficiency

In summary, in the 3SM, the equation used to calculate the QE based on the theory discussed above is:

$$QE(E,l) = \frac{\sum_{i=1}^{VBM} \sum_{f=WF}^{\infty} \int_{BZ} |M(i,f,\mathbf{k})|^2 \; \delta(E - (\epsilon_{f,\mathbf{k}} - \epsilon_{i,\mathbf{k}}) \; W(i,A,\mathbf{k}) \; I(E,l) \; esc(E,l) \; H(q_\perp > 0) \frac{d\mathbf{k}}{(2\pi)^3}}{\sum_{i=1}^{VBM} \sum_{f=VBM+1}^{\infty} \int_{BZ} |M(i,f,\mathbf{k})|^2 \; \delta(E - (\epsilon_{f,\mathbf{k}} - \epsilon_{i,\mathbf{k}}) \; W(i,A,\mathbf{k}) \; I(E,l) \frac{d\mathbf{k}}{(2\pi)^3}} \tag{4.23}$$

where VBM indicates the highest energy band in the valence band. The sum at the numerator includes all initial states in the valence band and the final states above the vacuum energy. The denominator takes into account all the processes than can absorb a photon with energy E. Therefore, all initial states from the valence band and all the final states in the conduction band are included.

5

Copper, Silver and Magnesium: Bulk and Surfaces

In this chapter an overview of the computed bulk and surface geometries and electronic structures of copper, silver and magnesium is presented. These were chosen because they are among the materials that are going to be tested in the VELA photoinjector for the CLARA FEL. Firstly their bulk properties will be reported and the most stable surfaces are discussed in the second part of the chapter.

5.1 Bulk Structure

Copper and silver crystals adopt the fcc cubic structure, which belongs to the space group $Fm\bar{3}m$ (number 225). Their primitive cells contain one atom and are characterised by the lattice vectors $\mathbf{a} = \mathbf{b} = \mathbf{c}$ and internal angles $\alpha = \beta = \gamma = 60^o$. Their conventional cells contain four atoms and have $\mathbf{a} = \mathbf{b} = \mathbf{c}$ and $\alpha = \beta = \gamma = 90^o$. Magnesium adopts the hcp structure, space group $P63/mcc$ (number 194), which is characterised by a primitive cell (that also correspond to the conventional cell) where $\mathbf{a} = \mathbf{b} \neq \mathbf{c}$, $\alpha = \beta = 90^o$ and $\gamma = 120^o$. Their crystal structures are depicted in Fig. 5.1. Structural optimisation was performed with respect to the lattice parameters and atomic coordinates of the bulk primitive cells. The experimental geometries obtained from X-ray powder diffraction [6–8] were used as the starting point. The optimised and experimental conventional lattice parameters (calculated using the consistent set of numerical and theoretical approximations discussed in Section 3.6) are reported in Table 5.1. The calculated lattice parameters show very good agreement with the experimental data. The highest difference is 1.6 % in the lattice parameter of silver. Calculation of the copper and magnesium lattice parameters reproduce the experimental ones within differences lower than 1 %. Previous calculations recently performed with DFT-PW methods differ of less than 2 % [85, 86] with respect to the lattice parameters obtained in this study. This confirms that the optimised bulk geometries obtained here are adequate for the generation of slabs to model the metal surfaces.

Table 5.1: Conventional cell lattice parameters for copper, silver and magnesium calculated using the DFT-PBE approach described in Section 3.6. Experimental measurements are obtained from X-ray powder diffraction experiments at room temperature [6–8]. All values are in Å.

	DFT-PBE (this study)	Exp.	$\Delta_{DFT-Exp}$
Copper	**a** = 3.630	3.615	0.41 %
Silver	**a** = 4.086	4.154	1.6 %
Magnesium	**a** = 3.190	3.209	0.60 %
	c = 5.182	5.211	0.56 %

5.2 Bulk Electronic Structure

The electronic structure of the materials at the optimised structure was calculated and is depicted in Fig. 5.2 as band structure and PDOS on the different angular momentum components calculated by using a Mulliken projection onto AO contributions (see Section 3.5 for details).

The copper band structure has been extensively compared to LDA and GW calculations and to experimental results following the analysis of Marini et al. [87]. The calculated electronic structure is in good agreement with previous calculations and experimental data. Also the silver and magnesium electronic states reproduce calculated data reported in the literature [88–92]. For example, the d-band of silver, which is about 5 eV in width, differs by 0.3 eV from previous APW calculations [93].

The PDOS show high contribution of d states at about -5.5 to -1.0 eV and -7.0 to -2.0 eV below the Fermi energy in copper and silver, respectively. The s band represents states that are homogeneously spread in the valence band starting from -8.0 eV and -9.0 eV below the Fermi energy for silver and copper, respectively. For magnesium all the contribution comes from s and p electrons. Its DOS for the valence band starts at -7 eV.

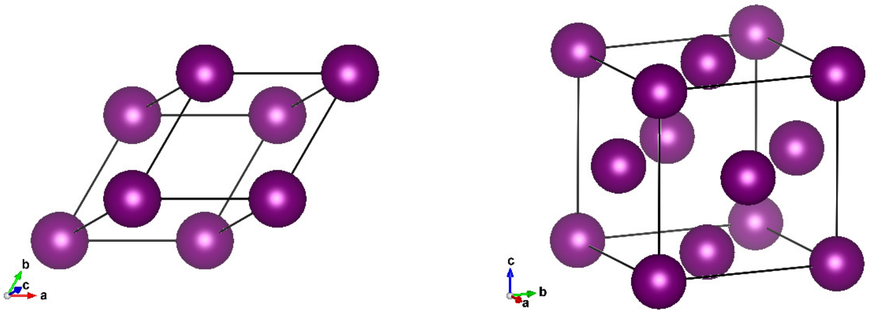

Cu/Ag primitive cell

Cu/Ag conventional cell

Mg primitive/conventional cell

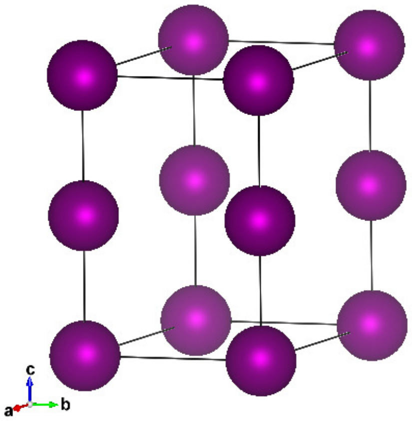

Figure 5.1: The bulk crystal geometry represented by means of the primitive and conventional cells for the materials used in this study. Top: copper and silver (fcc). Bottom: magnesium (hcp).

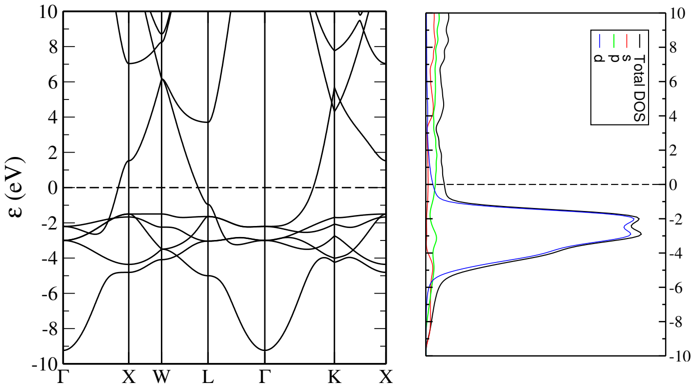
Copper

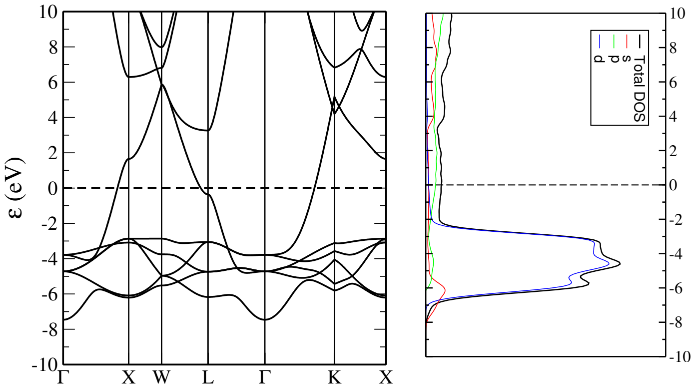
Silver

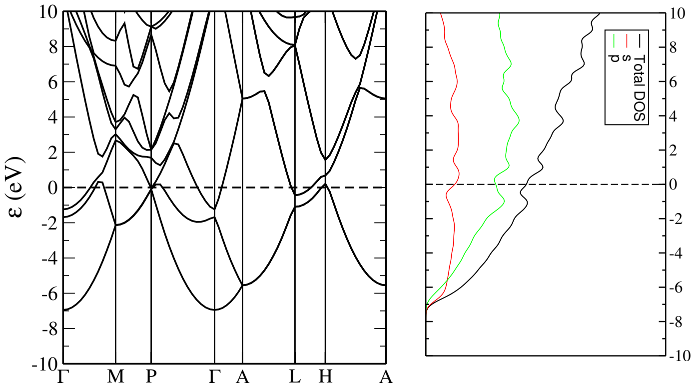
Magnesium

Figure 5.2: Electronic structure of copper, silver and magnesium: band structure (left) and projected density of states (right).

5.2.1 Surface Projected Bulk Band Structure

The SPBS has been calculated according to the procedure described in Section 3.5 and Appendix A.5.1.

The SPBS for all the surfaces discussed are depicted on the left hand side of Figures 5.3, 5.4 and 5.5. These are useful to highlight the presence of forbidden energy gaps in the bulk electronic structure and allow for an easier identification of surface states in the slab models (see Section 5.4).

5.3 Structure of the Low Index Surfaces

In order to simulate the behaviour of copper, silver and magnesium in photocathodes, the lower energy surfaces, which are the more likely to be present, of such metals are simulated using slab models. These are cut from the optimised bulk geometry discussed in Section 5.1. For Cu and Ag the (111), (110) and (100) surfaces were considered. For Mg the (0001), $(10\bar{1}0)$ and $(10\bar{1}1)$ were studied. Their structures are depicted in Fig. 5.6. The magnesium (0001) surface is used in Chapter 7.4 as the substrate to simulate the effect of adsorbates interacting on this material. This surface exhibits two different hollow sites: fcc and hcp. The adsorption energy of oxygen, hydrogen and cesium onto these two sites of metal surfaces has been widely investigated by using DFT-PAW [94] and DFT-GGA methods [95]. The fcc and hcp sites exhibit higher adsorption energies with respect to bridge and top interaction and differences between the two of them lower that 0.05 eV/molecule. The differences in the WF change upon external atoms adsorption are negligible for the two sites (of the order of 0.01 eV) [94, 95]. The hcp site was, therefore, chosen for all simulations of surfaces interacting with adsorbates, as it is discussed in Chapter 7.4.

Slab models are periodic along the x and y directions and consist of finite thickness along z (see Section 3.4). The thickness of the slab must be carefully checked through convergence tests. In the current study the surface energy, displacement and electronic environment of the central atoms were used. The atomic structure of the slab model is determined by energy minimisation keeping the lattice parameters fixed. This is the approach used in surface simulation and it reflects the fact that the perturbation introduced by the surface is not strong enough to change the lattice constant of the sample and the bulk one will be predominant. Atoms are allowed to move in three dimensions during the geometry optimisation. The surface energy of the 10 layer slabs is converged within 10^{-3} J/m^2. For the 10 layer slab, the displacement of the central

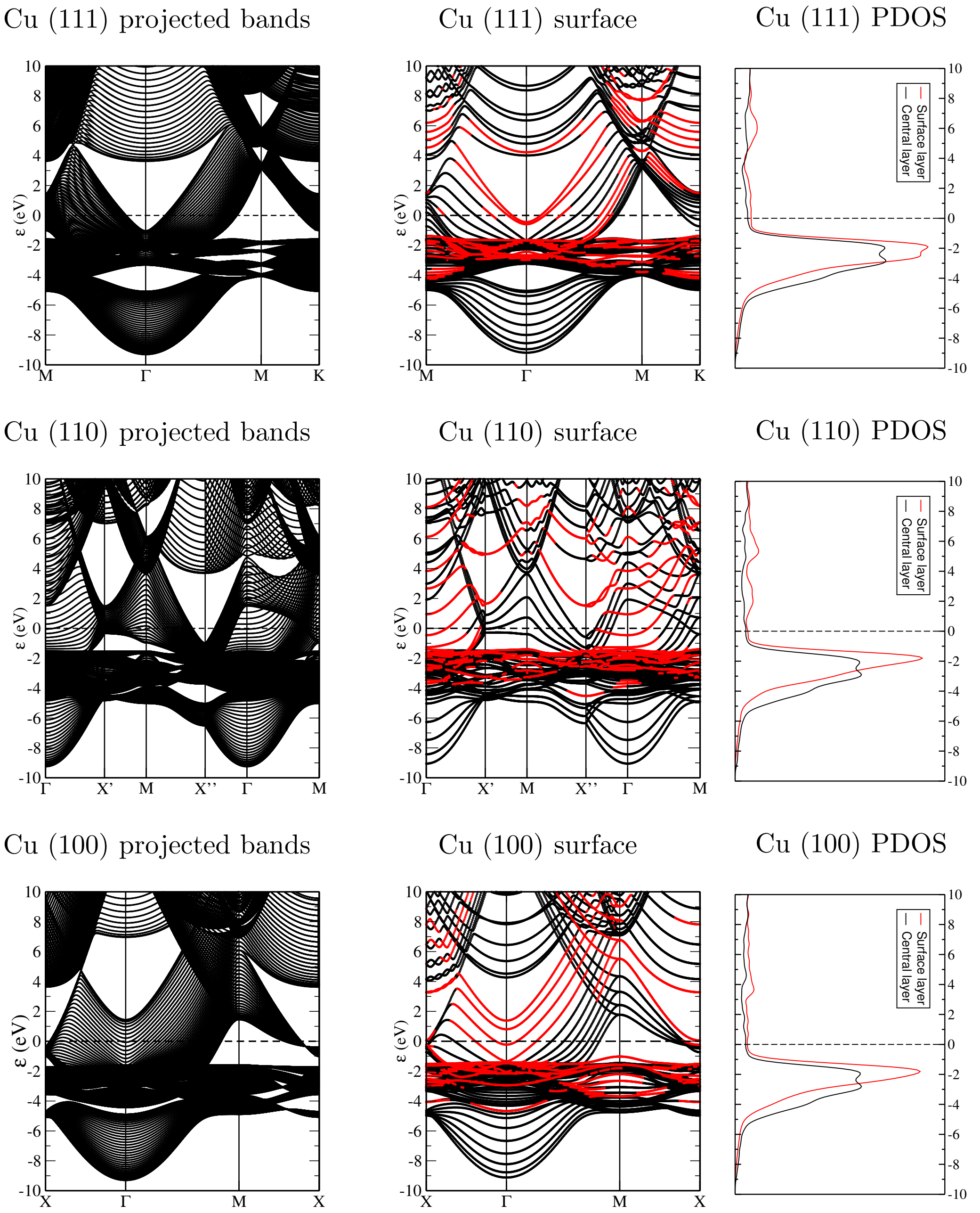

Cu (111) projected bands

Cu (111) surface

Cu (111) PDOS

Cu (110) projected bands

Cu (110) surface

Cu (110) PDOS

Cu (100) projected bands

Cu (100) surface

Cu (100) PDOS

Figure 5.3: Copper (111), (110) and (100) surfaces. Left: surface projected band structure. Middle: surface band structure. Right: surface and central layer PDOS. Surface states, identified according to the procedure described in Section 4.2.1 are depicted in red. States equally delocalised on the whole slab are shown in black.

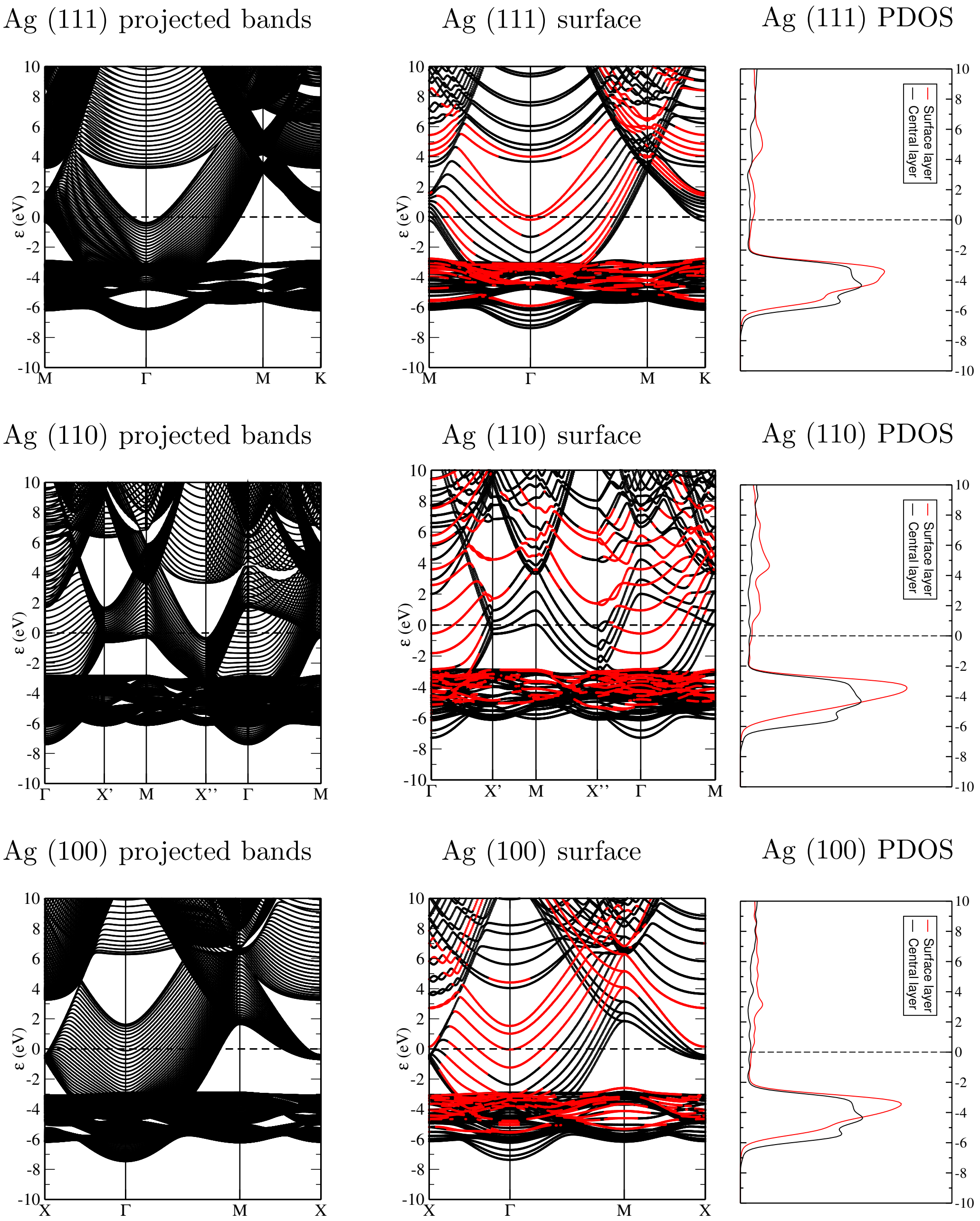

Figure 5.4: Silver (111), (110) and (100) surfaces. Left: surface projected band structure. Middle: surface band structure. Right: surface and central layer PDOS. Surface states, identified according to the procedure described in Section 4.2.1 are depicted in red. States equally delocalised on the whole slab are shown in black.

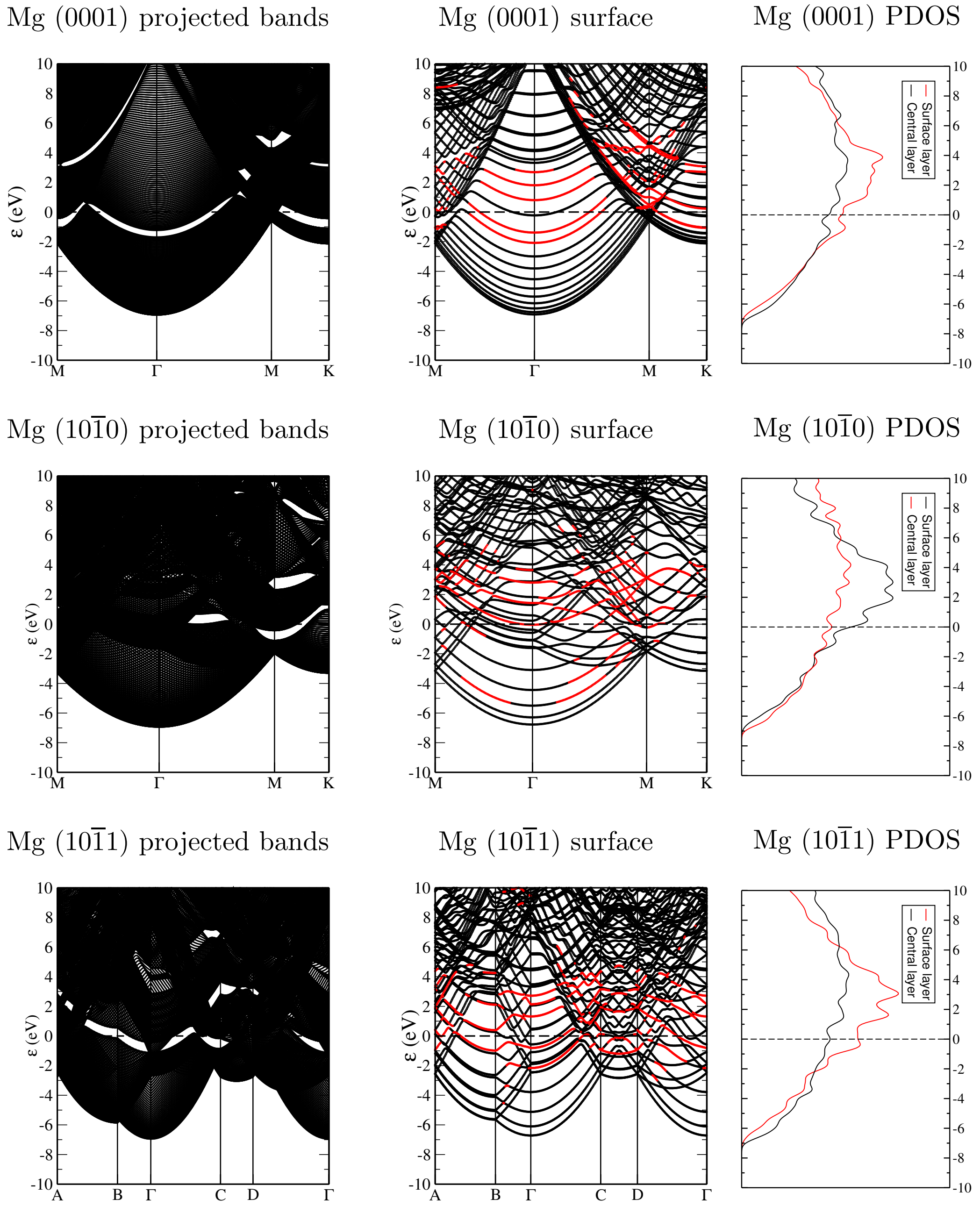

Figure 5.5: Magnesium (0001), (10$\bar{1}$0) and (10$\bar{1}$1) surfaces. Left: surface projected band structure. Middle: surface band structure. Right: surface and central layer PDOS. Surface states, identified according to the procedure described in Section 4.2.1 are depicted in red. States equally delocalised on the whole slab are shown in black.

Table 5.2: Lattice parameters, displacement of the first layer, surface energy, work function and percentage of each surface according to a Wulff construction for the Cu and Ag (111), (110) and (100) surfaces and Mg (0001), ($10\bar{1}0$) and ($10\bar{1}1$) surfaces.

	Cu			Ag			Mg		
	(111)	(110)	(100)	(111)	(110)	(100)	(0001)	($10\bar{1}0$)	($10\bar{1}1$)
$\mathbf{a}_{slab}$	2.567	2.567	2.567	2.937	2.937	2.937	3.193	3.193	3.193
$\mathbf{b}_{slab}$	2.567	3.630	2.567	2.937	4.154	2.937	3.193	5.185	6.089
γ	120	90	90	120	90	90	120	90	105.20
$\Delta s1^{st} layer$	-1.05	-6.96	-3.08	-2.36	-5.34	-0.88	0.02	-0.09	-0.01
$\Delta s2^{nd} layer$	-0.17	3.31	0.27	0.17	3.04	1.02	-0.01	0.06	0.01
$\Delta s3^{rd} layer$	0.05	-1.39	0.02	-0.18	-1.50	0.51	-0.01	-0.04	0.01
$\mathbf{E_{surf}}$ eV/atom	0.47	0.90	0.63	0.38	0.71	0.48	0.29	0.65	0.75
J/m^2	1.32	1.55	1.53	0.80	0.93	0.88	0.56	0.63	0.64
WF (eV)	4.50	4.13	4.27	4.25	3.42	3.72	3.49	3.28	3.40
%**Wulff**	69.1 %	9.10 %	21.8 %	62.9 %	9.84 %	27.3 %	28.0 %	50.0 %	22.0 %

layer is found to be less than 0.1 % of the bulk interlayer spacing. Furthermore, the electronic structure of the central layers, calculated using the projection of the density of states (PDOS) on the central atoms, reproduces that of the bulk crystal. This is confirmed by comparing the black line in the PDOS plots in Fig. 5.3, 5.4 and 5.5 to the bulk total DOS in Fig. 5.2. This demonstrates that the potential in the centre of the slab replicates that in a layer of the bulk crystal. Adsorption of oxygen, hydrogen or cesium to the surface of the 10 layer slab produces negligible changes in the displacement and electronic structure of the central layer. These tests suggest that the 10 layer slab model is adequate for the study of changes in the QE due to surface modifications.

The lattice parameters of the slabs are reported in Table 5.2 together with the displacement of the top three layers from the bulk positions. The (110) surface of Cu and Ag exhibit the larger shift along the z direction, where the top layer moves downwards of 6.96 % and 5.34 % of the bulk interlayer spacing, respectively. For the (111) surface of the fcc metals the displacements are of the order of 2 % for the first layer. Displacements for the magnesium (0001) surface are negligible (of the order of 0.2 % for the first layer). The displacement calculated in this study is confirmed by previous calculations using DFT-PW methods [96, 97] (and different PP: PBE, PW91 and the PAW method). For example, displacement of 5 % of the topmost layer of the Cu (111) surface are reported [96]. Also the top layer of Mg surfaces is reported to move of less than 0.1 % [97].

The computed surface energies of the slab models studied here are reported in Table 5.2. Copper and silver will be discussed first. For these two metals, the values obtained

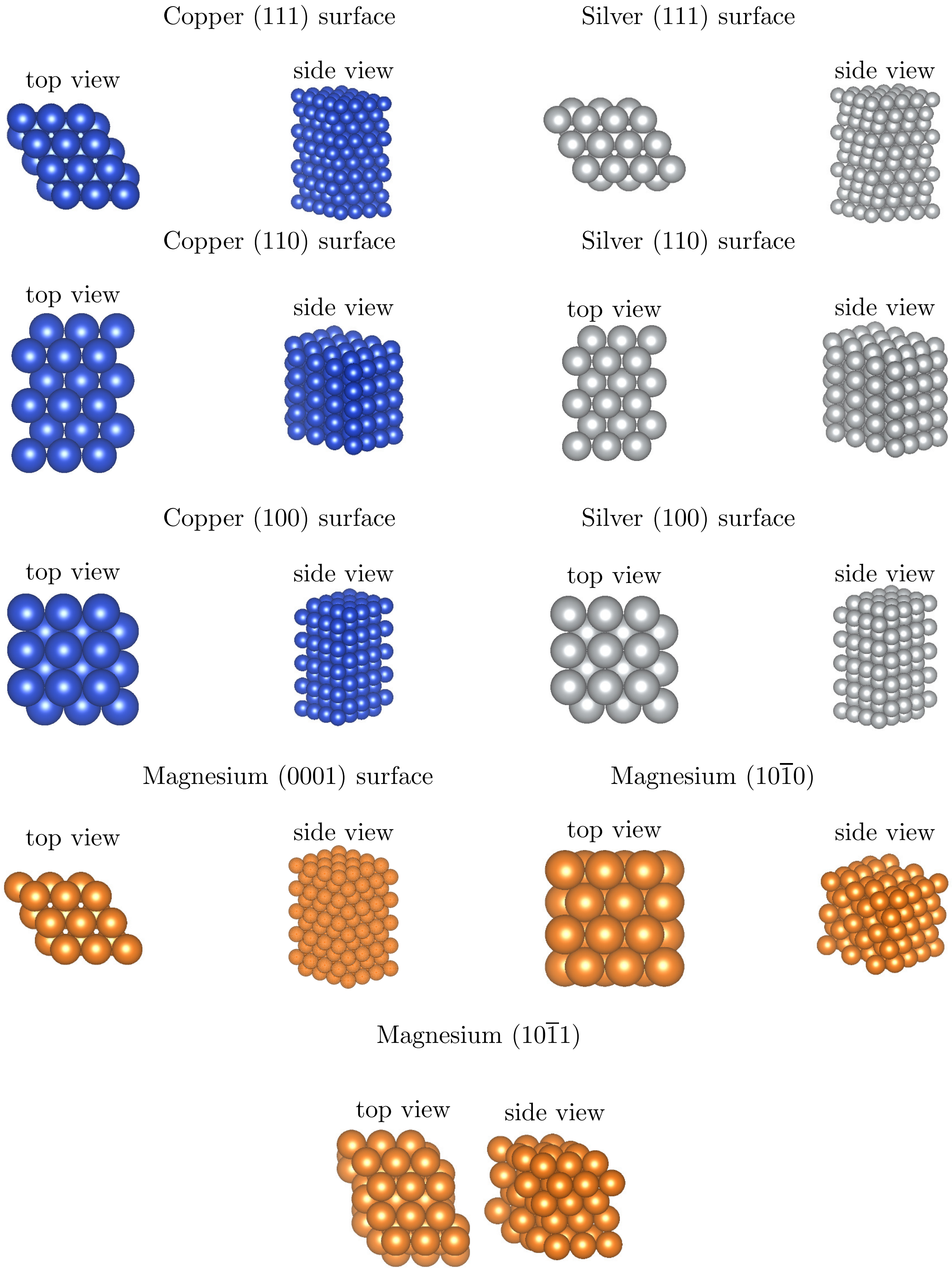

Figure 5.6: Structure of the 10 layer slabs used to model the surfaces of copper, silver and magnesium.

are somewhat lower than the those reported previously in the literature which were calculated at local density (LDA) or generalized gradient approximation (GGA) levels of theory using local basis sets [45] or linear muffin-tin orbitals in the atomic-sphere approximation (ASA) [98, 99]. This is to be expected as the variational freedom of the PW basis set used in the current study provides a more accurate description of the spread of electron density into the vacuum region which is, by necessity, constrained within the ASA or with standard local basis sets [100]. The surface energy of silver computed here is in agreement with other DFT-PW calculations [101] (maximum deviations of 8 %). As an additional test, a calculation using the Quantum Espresso code with the same exchange-correlation functional, **k** sampling grid and plane wave energy cutoff as the CASTEP calculations was performed. It yields an almost identical surface energy (differences lower than 5 x 10^{-3} J/m^2). Larger variations are seen when the pseudopotential is altered. This was tested for copper: using the projector augmented wave (PAW) method produces a variation of 6% in the surface energy relative to using the PBE pseudopotential. Despite these numerical discrepancies in the absolute surface energy, which are inherent in the pseudopotential approach, the relative surface energies of different facets are more consistently described, when compared to previous calculations [45, 98, 99]. For copper the (110) and (100) surfaces energies are 17% and 16% higher than the (111) one, respectively. Similar results are obtained for silver, where the (110) and (100) surfaces energies are 16% and 9% higher than that of (111), respectively. Magnesium (0001) surface energy has the lowest surface energy for this metal [89]. Furthermore, values calculated in the current study ($E_{surf} = 0.54$ J/m^2) are in accordance with DFT-PW calculations employing LDA pseudopotential [102], where values of 0.64 J/m^2 are found.

The equilibrium crystallite morphology can be estimated using the Wulff construction as described in Section 3.5. From the morphology an estimate of the surface area of each facet present in a polycrystalline sample can be calculated. The Wulff construction of a copper crystallite is displayed at the top of Fig. 5.7. The shape of this construction is in agreement with transmission electron microscopy (TEM) images of copper nanoparticles synthesized at low H_2 pressure [103]. Hydrogen is used in the experiment in Ref. [103] as a reducing agent in order to study the effect of water interaction with the copper crystallite. It is present at a pressure of 1.5 mbar while TEM images were recorded. The shape of such nanoparticles changes dramatically in the presence of oxidising or reducing agents. However, at low H_2 pressure it is expected to be comparable to simulations performed in vacuum [104]. The Wulff construction for silver is depicted at the middle of Fig. 5.7. It has the same shape of the copper one, with small differences in the relative abundance of the three surfaces. For both copper and silver, the major contribution to the surface area is due to the lowest energy surface, which is the (111) surface for both metals, representing 69% of the copper and 63% of the surface area of silver crystallites (see Table 5.2 for details). Since the (111) surface is the most stable for silver and therefore likely to be predominant in polycrystalline sample it is used in Chapter 8.3 as the basis for our calculations of the variations in QE induced by surface reconstruction. For magnesium, the Wulff construction differs from the copper and silver one because of the hexagonal symmetry of the crystal.

The work function of the surfaces reported in Table 5.2 was calculated as the difference between the Fermi energy and the average of the potential between neighbouring slabs (see Section 3.5 for details). For both copper and silver the (111) surface exhibits the highest work function, 4.50 eV and 4.25 eV, respectively. The surface having the lowest work function among the fcc metals is Ag the (110) surface, whose work function is 3.42 eV. However, as seen from the Wulff construction, this surface represents less than 10 % of a polycrystalline sample. The effect of such a low WF values, combined with high surface energy, on the photoemission is discussed in Section 6.1. Alkali earth metals, such as Mg are well known for their low work function values [99]. The Mg $(10\bar{1}0)$ surface shows, indeed, the lowest WF among the metals and facets studied here. It is comparable with the Ag (110) surface. However, for the Mg, such low WF surface represents 50 % of a polycrystalline sample.

Work function measurements for various copper surfaces were carried out by Gartland et al. [105]. The comparison with such results suggests that the work function calculated in the current PW-PP calculations using the GGA exchange-correlation functional is generally 0.3 eV below that determined from PE measurements. As it is well known [106], the predicted WF oscillates with slab thickness and so about 0.1 eV of this discrepancy may be due to the thin slab model. The remaining discrepancy is likely to be due to the choice of pseudopotential and the exchange-correlation potential.

In order to compare the calculated work function values to data obtained on polycrystalline samples, the average work function was calculated as the average over a crystallite by weighting the WF of each facet with its fractional contribution to the total surface area. The resulting work functions are 4.41 eV, 4.06 eV and 3.37 eV for copper, silver and magnesium, respectively. Commonly accepted values based on linear-muffin-tin-orbitals Green's function theory are in the range 4.4-5.3 eV for copper, 4.2-4.7 eV for silver and 3.7-3.9 eV for magnesium [88, 99, 107]. From photoemission experiments work function values between 4.3 eV and 5.1 eV for copper and between 4.2 eV and 4.7 eV for silver have been found in literature [108]. The commonly accepted

Copper

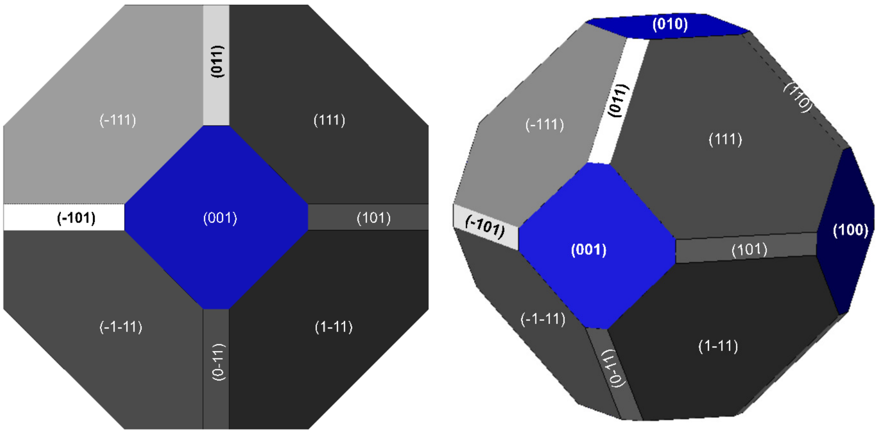

Silver

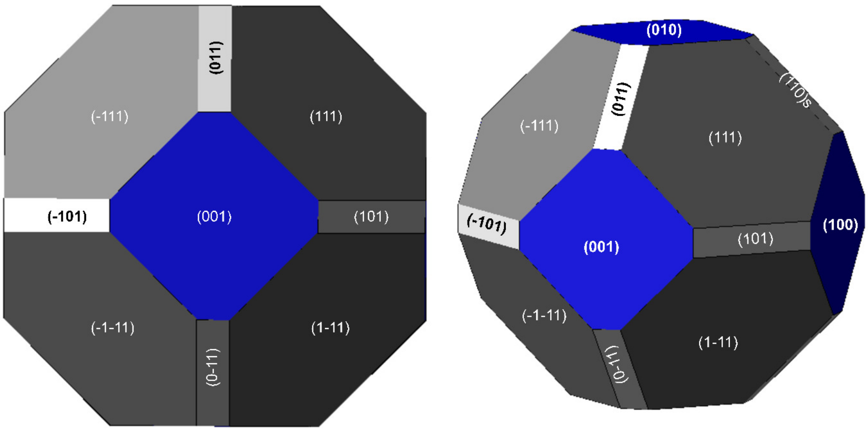

Magnesium

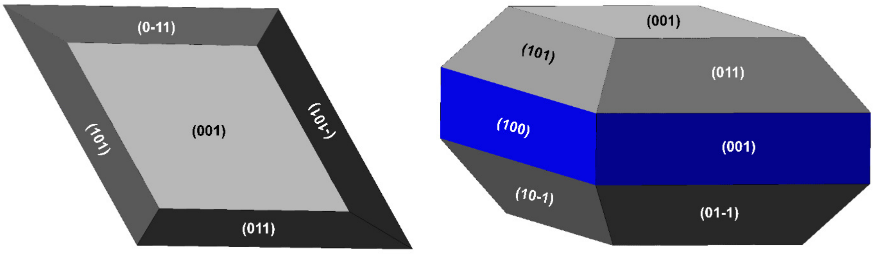

Figure 5.7: The Wulff construction of the equilibrium morphology for a copper, silver and magnesium crystallite (left: top view, right: side view).

experimental value is 3.84 eV for magnesium [108]. The reasons for the 0.3 eV discrepancy between the WF values reported here and other simulations based on local BS [88, 99, 107] is the same discussed above. The WF measurements show high sensitivity to the structure of the outermost layers of the sample [109]. For this reason obtaining atomically clean surfaces is essential if experimental results have to be compared to simulations.

5.4 Surface Electronic Structure

The PDOS on the first and central layer are reported on the right hand side of Figures 5.3, 5.4 and 5.5. This provides a visualisation of the overall effect of the perturbation introduced by the surface on the bulk electronic structure five layers below the surface. For copper, the PDOS on the surface layer shows a shift of the d bands by 0.1 eV towards the Fermi energy. Also, some extra s and p states are present in the range of energy between the Fermi level and the top of the d bands. For silver such a shift of the top of the d bands is not found. However, the bottom of the d bands is shifted closer to the Fermi level and more states, with respect to the central layer, are found between -3 eV and -4 eV. For magnesium, the presence of surface states just below the Fermi energy can be noted by the higher peak in the PDOS on the surface layer at -1 eV.

The surface band structures have been computed along the same path used in the SPBS (see A.5.1). The resulting band structures are depicted on central panel of Figures 5.3, 5.4 and 5.5, where the energy levels whose contribution from a surface layer is higher than 15% ($\mathbf{W}^{\mathbf{k}}_{i,l} > 15\%$, where l is the top layer, see Section 4.2.1), are highlighted in red. By comparing the surface band structure to the corresponding bulk projected one it is possible to determine that these states are not present in the latter confirming they are introduced by the surface.

The surface band structures calculated in this study are in overall good agreement with respect to those deduced from measurements of the surface electronic structure [110–117]. For example, the very well known state in the L gap of the copper (111) surface band structure is calculated to have an energy minimum at 0.45 eV below the Fermi level and crossing it at 0.28 Å^{-1} along the $\mathbf{\Gamma}$ to $\mathbf{M}$ direction in reciprocal space. This compares very well to the most recent values deduced from angle resolved photoemission experiments (ARPES) and confirmed by KKR band structure calculations [113], where the minimum energy is 0.37 eV and crossing of the Fermi level at 0.2 Å^{-1} along the Γ to M direction. The other surface state on the Cu (111) surface is near the K symmetry point. In this work this state is found at 2.7 eV which is comparable to the 3.0 eV found in ARPES experiments [114].

In summary, the first part of this chapter presented a detailed description of the bulk geometries and electronic structures of copper, silver and magnesium. The second part of this chapter aimed at describing the slab models used to simulate the photocathode surfaces. Their morphology and electronic properties were extensively discussed and will be used as starting point for the photoemission simulations in the next chapters.

6

Photoemission From Clean Surfaces

Photoemission from copper, silver and magnesium surfaces has been widely investigated both from the experimental and computational points of view [56, 57, 118–120]. However, most of these works focus on determining the initial state energy and positioning of the electronic levels. These experiments and simulations will therfore typically present data as graphs of intensity of emitted electrons at fixed photon energy vs. initial state energy. Several example of these are reported in literature either using DFT based calculations [120], or the one step model in the several implementations discussed in Chapter 4. These kind of computed spectra can be compared to the DOS of the materials or its band structure if an angle resolved photoemission (ARPES) experiment is performed. Also three step model based calculations have been used to interpret experimental data [62, 63]. However, these are based on the bulk electronic structure, whereas the measured photoemission, in general, is dominated by the electronic structure of the top few atomic layers of the crystal and therefore may be poorly reproduced by calculations of just the bulk electronic structure [62, 63].

The goal of this study is different with respect to the calculations discussed so far, because it aims at correlating the calculated electronic structure to the total quantum efficiency (QE) for realistic models of crystal surfaces. There are, therefore, two main goals: providing the experimentalist with a tool to screen various materials in order to choose the best candidates to be tested in photoinjectors and understanding the role surface chemistry and morphology play in the photoemission process.

Here, a simple model of the electronic structure (the DFT eigenvalues) is used in conjunction with a sophisticated model of the surfaces structure, composition and chemistry. More sophisticated theories (discussed in Section 4.1) should be used in order to recover the fine structure of a photoemission experiment, such as many body effects or the presence of satellites [121]. The strategy for the design of photoemitting materials requires the understanding of trends and mechanisms. The theory outlined in Chapter 4.2.2 imposes a compromise on the accuracy of the underlying model for the excitation and on the coupling to the scattering state in order to make sure that the variations in QE induced by surface engineering are captured by the model. The theory used must be sufficient to clearly distinguish the different mechanism that operate and it must be applicable in a standard way to large models of surfaces in order to recover their structures in realistic environments. The method is validated against trends of different substrate metals in this chapter and against different surface treatments in the next chapter.

6.1 Clean surfaces

Unreconstructed clean surfaces can be modeled using the primitive cell of a 2D periodic slab cut from the bulk crystal. The Brillouin zone folding is, therefore, not an issue in this case and the full approach presented in Chapter 4 can be used. The final equation derived in Section 4.2.2 for the layer-by-layer quantum efficiency is repeated here:

$$QE(E,l) = \frac{\sum_{i=1}^{VBM} \sum_{f=WF}^{\infty} \int_{BZ} |M(i,f,\mathbf{k})|^2 \ \delta(E-(\epsilon_{f,\mathbf{k}}-\epsilon_{i,\mathbf{k}}) \ W(i,A,\mathbf{k}) \ I(E,l) \ esc(E,l) \ H(q_\perp > 0) \frac{d\mathbf{k}}{(2\pi)^3}}{\sum_{i=1}^{VBM} \sum_{f=VBM+1}^{\infty} \int_{BZ} |M(i,f,\mathbf{k})|^2 \ \delta(E-(\epsilon_{f,\mathbf{k}}-\epsilon_{i,\mathbf{k}}) \ W(i,A,\mathbf{k}) \ I(E,l) \frac{d\mathbf{k}}{(2\pi)^3}} \tag{6.1}$$

There are three main properties of the material that will have the largest influence on the total number of emitted electrons, if simulated through this equation:

- **the work function** (WF) determines the photoemission onset. This is the lowest photon energy which gives a detectable signal of emitted electrons. This can be observed in the numerator of Eq. 6.1, where the sum runs over final states (f) above the WF. Electrons excited to states below this energy are thermally de-excited and do not contribute to the emission. As a rule of thumb it is, therefore, assumed that the lower the WF of the surface, the higher its QE (for photon energies higher that the WF). Although often quoted as a principle of cathode design, this rule is often insufficient to even produce the trends in the observed QE. For example, for Y vs. Mg photocathodes [122, 123].

- **the surface states** discussed in Section 3.5 are relevant because being localised on the surface, electrons excited from these states do not need to travel through the slab to be emitted. For such states the $\mathbf{esc}_{i,l}^{\mathbf{k}}$ term in Eq. 6.1 is larger leading to larger values of QE(E,l).

- **the constraint on the momentum** determines for each photon energy which are the states whose momentum component points outside the surface upon absorption. It is taken into account in the $\mathbf{H}(\mathbf{q}_{\perp} > 0)$ term of Eq. 6.1. This is a Heaviside step function, which means electrons not satisfying this constraint are excluded from emission. This constraint is applied to the clean surfaces because they can be modeled through their primitive cells.

The experimental set up for the QE measurement usually involves a monochromatic light [122, 123]. In order to compare the QE of different materials and crystal facets calculations were performed for a photon energy of 4.7 eV. This energy is used to approximate the energy of a photon emitted from a Ti:sapphire laser (4.66 eV for the third harmonic [124]). Furthermore, this is the wavelength that will be used in the CLARA FEL [2] photoinjector. The total QE anticipated from a polycrystalline sample, consisting of randomly oriented crystallites, at photon energy of 4.7, eV is averaged by using the fractional contribution of each facet according to the Wulff construction as described in Section 5.3 for the work function, whose values are also copied in Table 6.1 and discussed in the following.

In order to better understand the photoemission (PE) spectra, the concept of the *momentum DOS* is introduced. This is obtained by calculating a PDOS and applying a constraint on the momentum of the states to be included. Fig. 6.1, 6.2 and 6.3 provide an easy way to visualise the states contributing to the photoemission at photon energy of 4.7 eV. The shaded area in the BS (left hand side of the figures) represents the region where the momentum is too large to produce emission from the surface at such photon energy. In other words, the momentum component of the excited electron, upon absorption of the photon is negative see Eq. 4.21. The highest contribution usually comes from $\mathbf{\Gamma}$ and the contribution decreases moving away from the BZ centre according to the quadratic dependence on the coordinate of the $\mathbf{k}$ point (see Eq. 4.21). In the momentum DOS (right hand side of the figures) only the states leading to emission are accounted for. These graphs allow for an easy visualisation of the regions where the surface states will have an impact on the emission. If a surface modification (adsorbate or reconstruction) introduces states in this region, it will improve the efficiency of the photocathode. If the states are added to regions of the electronic structure where electrons are not emitted for the photon energy used in the photoinjector then no improvement will be observed.

This analysis of the electronic structure gives further insight into the role played by surface states in the emission process. In order to design surface structures to enhance the QE of photocathode materials, the region where additional states should be added must be taken into account according to this analysis. Among the surfaces studied here, the Cu (111) surface is the best example of this behaviour. The black curve corresponding to the topmost layer has the highest contribution. On the contrary, for silver surfaces the topmost layer is the one that has the lowest number of states contributing to the emission at 4.7 eV. This means that in silver the photon will be absorbed preferentially by states delocalised on the whole slab rather than on the topmost layer. The effect of this different localisation of states in the slab is discussed in the following.

The computed QE for all the surfaces discussed in Chapter 5.4 are reported in Fig. 6.4 and 6.5. Note that the QE scale used in the figures is the same for copper and silver 0 to 3x10^{-3}, whereas for magnesium the range is between 0 to 5x10^{-4}. Since the emission onset is determined by the WF, it is expected to be lower for magnesium surfaces. Indeed, the onset for the magnesium surfaces is between 3 and 3.5 eV. Among the fcc metals, the Cu (110) surface has the lowest onset being in the region around 3.5 eV.

Another noticeable difference is the shape of the plots. Copper and silver surfaces display low emission at threshold photon energies which starts with a low emission that increases throughout the range of photon energies studied here. For magnesium surfaces there is a maximum around 5 eV. This difference can be explained in terms of the different electronic structure for copper and silver with respect to magnesium. Copper and silver have filled d bands that are more localised than the s and p bands. These give rise to the flat bands in the energy range between around -1 eV and -4 eV for copper and -3 eV and -6 eV for silver (with respect to the Fermi energy). With increasing photon energy, more states will contribute to the emission. The momentum constraint (Eq. 4.21), means that the first states to be included will be the ones localised at $\mathbf{\Gamma}$, then the ones at larger $\mathbf{k}$ point coordinates, with the number of accessible states varying quadratically with the photon energy. When the photon energy becomes large enough also states at the border of the BZ will start emitting. Since magnesium does not have states in the valence band at large momentum components, once all the states near $\mathbf{\Gamma}$ are accessible for emission, a maximum is reached.

The computed QE at $\hbar\omega = 4.7$ eV is reported in Table 6.1. The computed QE follows the WF trends, which means a higher efficiency is found for lower WF facets. The only exception to this, in the surfaces simulated here, are the Ag (110) and (100)

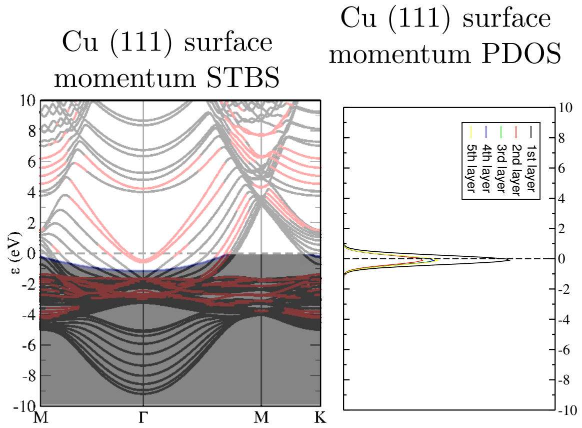
Cu (111) surface momentum STBS

Cu (111) surface momentum PDOS

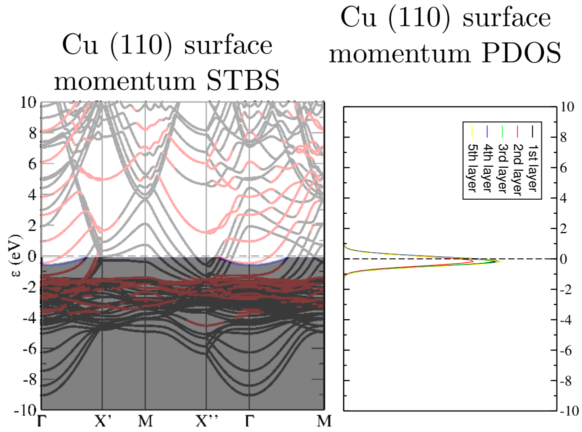
Cu (110) surface momentum STBS

Cu (110) surface momentum PDOS

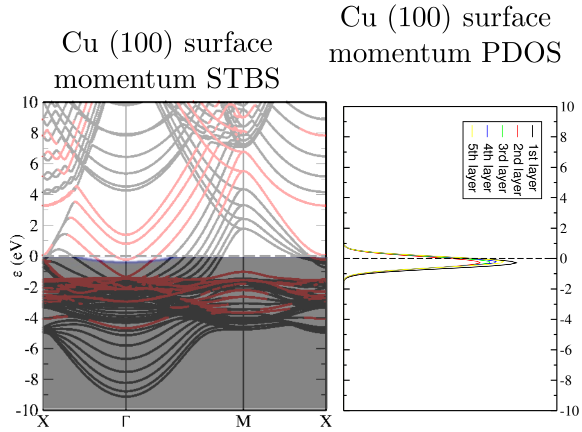
Cu (100) surface momentum STBS

Cu (100) surface momentum PDOS

Figure 6.1: Copper (111), (110) and (100) surfaces. Left: surface states band structures. The states not contributing to the photoemission at $\hbar\omega = 4.7$ eV were shaded. Right: layer-by-layer PDOS only states contributing to the photoemission at $\hbar\omega = 4.7$ eV are depicted. Surface states, identified according to the procedure described in Section A.5.1 are depicted in red. States equally delocalised on the whole slab are shown in black.

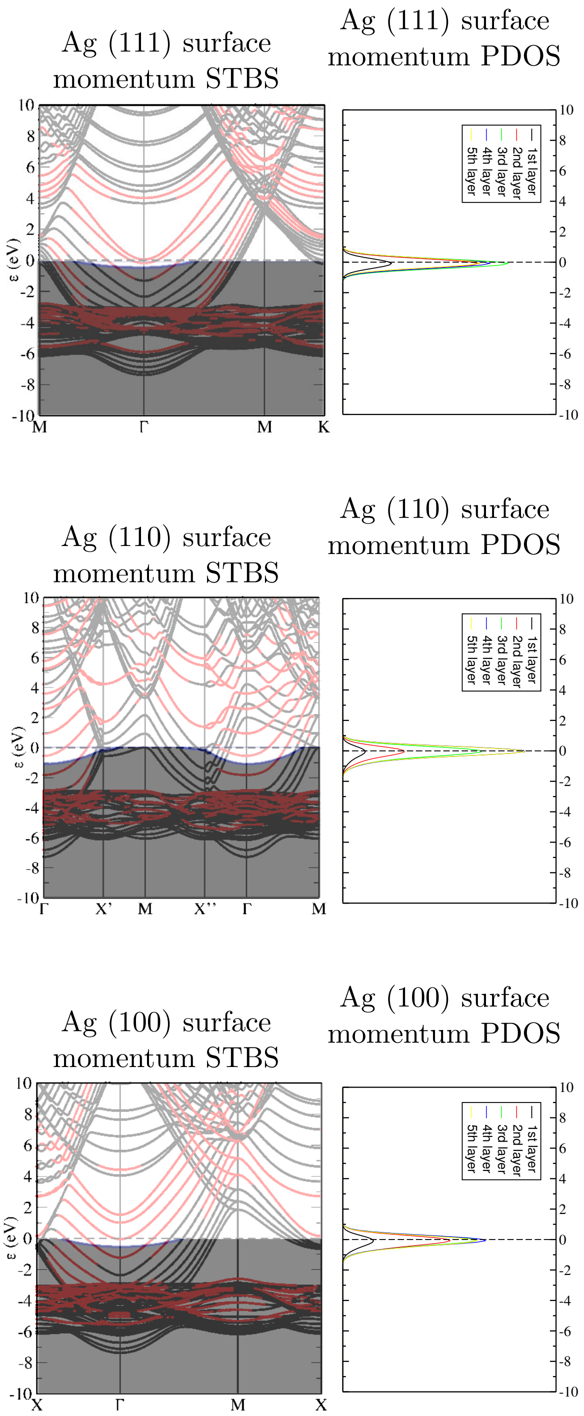

Figure 6.2: Silver (111), (110) and (100) surfaces. Left: surface states band structures. The states not contributing to the photoemission at $\hbar\omega = 4.7$ eV were shaded. Right: layer-by-layer PDOS only states contributing to the photoemission at $\hbar\omega = 4.7$ eV are depicted. Surface states, identified according to the procedure described in Section A.5.1 are depicted in red. States equally delocalised on the whole slab are shown in black.

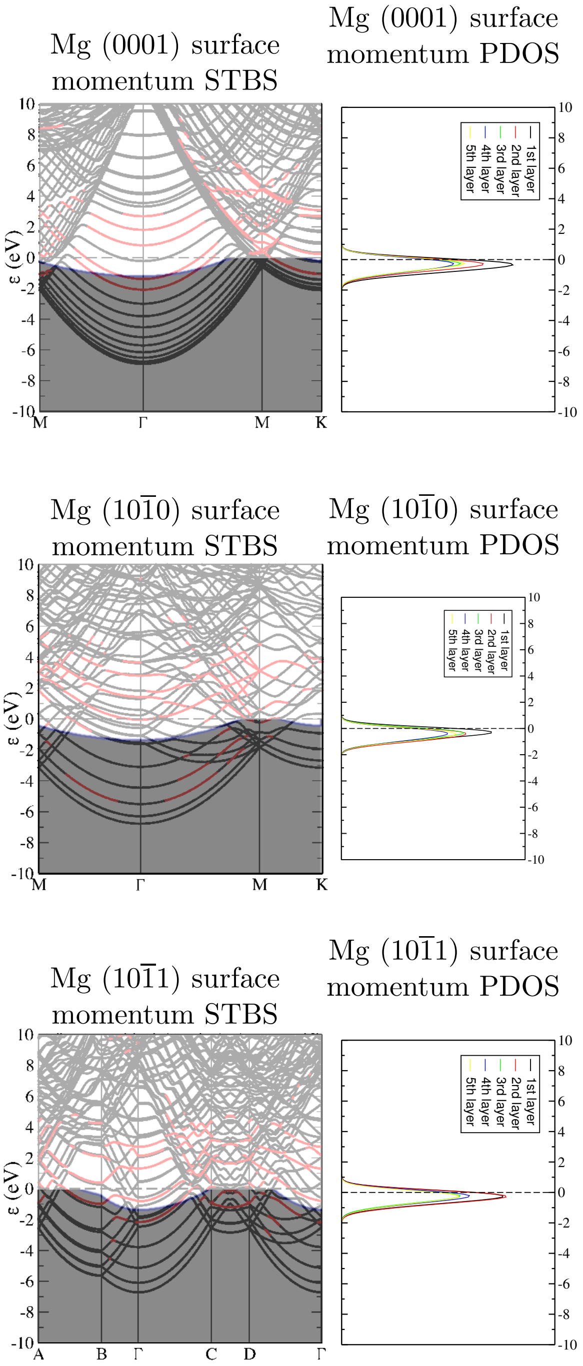

Figure 6.3: Magnesium (0001), (10$\bar{1}$0) and (10$\bar{1}$1) surfaces. Left: surface states band structures. The states not contributing to the photoemission at $\hbar\omega = 4.7$ eV were shaded. Right: layer-by-layer PDOS only states contributing to the photoemission at $\hbar\omega = 4.7$ eV are depicted. Surface states, identified according to the procedure described in Section A.5.1 are depicted in red. States equally delocalised on the whole slab are shown in black.

Table 6.1: Work function, QE at photon energy of 4.7 eV for the Cu and Ag (111), (110) and (100) surfaces and Mg (0001), (10$\bar{1}$0) and (10$\bar{1}$1) surfaces. Also the percentage of each crystal facet according to a Wulff construction is reported (see Section 5.3 for more details).

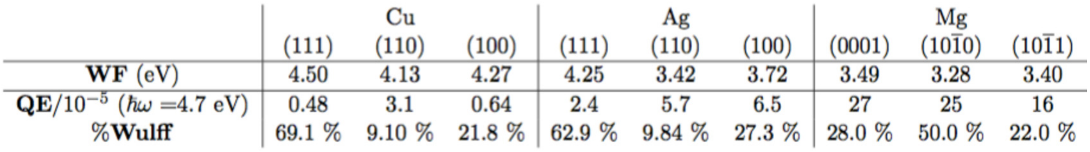

	Cu			Ag			Mg		
	(111)	(110)	(100)	(111)	(110)	(100)	(0001)	(10$\bar{1}$0)	(10$\bar{1}$1)
WF (eV)	4.50	4.13	4.27	4.25	3.42	3.72	3.49	3.28	3.40
QE/10^{-5} ($\hbar\omega$ =4.7 eV)	0.48	3.1	0.64	2.4	5.7	6.5	27	25	16
%**Wulff**	69.1 %	9.10 %	21.8 %	62.9 %	9.84 %	27.3 %	28.0 %	50.0 %	22.0 %

surfaces. Indeed, the quantum efficiency of the latter is slightly higher than the Ag (110) surface, despite its WF being higher.

The computed magnesium efficiency is the highest, which is on average one order of magnitude higher than the one of the other two metals, followed by silver and copper. However, the detailed variation requires explanations in terms of electronic structure and localisation on the surface layer. For example, the WF of the Cu (110) surface is about 0.7 eV higher than that of the Ag (110) surface one. However, the efficiency of the latter is only slightly higher than the former, much less than would be expected based on the difference in WFs. This behaviour can be explained looking at the momentum DOS in Fig. 6.1 and 6.2. The Cu (110) surface has a high number of states able to emit that are highly localised on the surface, whereas in the Ag (110) surface the contribution from the topmost surface layer is a relatively small proportion of the total emission as there are significant contributions from subsurface layers.

It is interesting to note that the QE for the same material can vary in a range of one order of magnitude according to the facet studied. Ideally, the data obtained here should be compared to facet dependant QE experiments that are not available at the moment, but further collaborations with experimental groups able to carry out this kind of experiments is being sought.

In order to compare these simulations to experimental data from a polycrystalline sample, an averaged QE was computed by using the fractional contribution of each facet according to a Wulff construction as reported in Table 5.2 and repeated in Table 6.1. The averaged QE was found to be 7.5 x 10^{-6} for copper, 3.8 x 10^{-5} for silver and 2.4 x 10^{-4} for Mg.

Another interesting example for copper, is the QE of the (110) surface, which is six times higher than QE of the (111) surface. However, the former only represents 9 % of a polycrystalline sample, whereas the latter represents 70 % of a nanoparticle

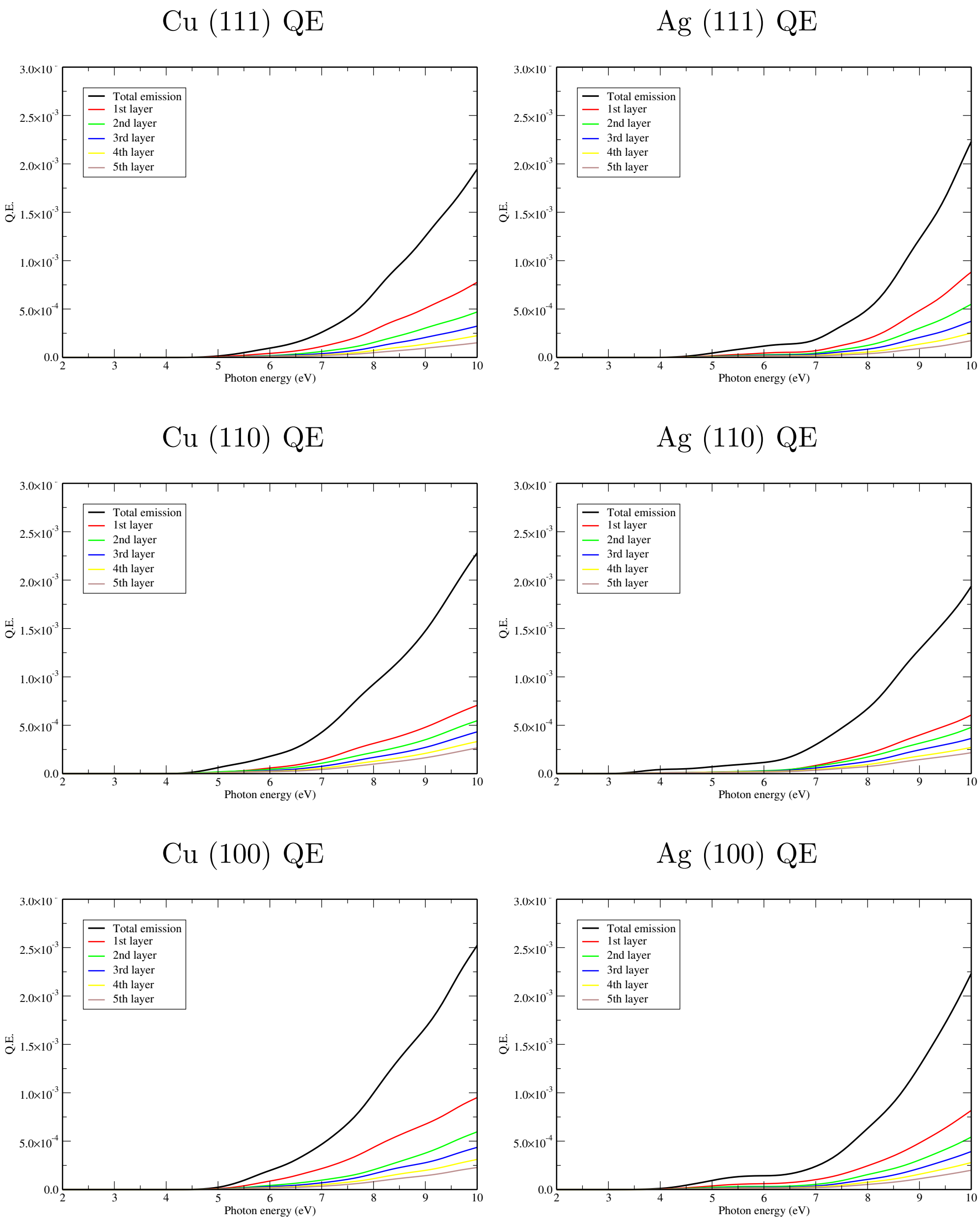

Cu (111) QE

Ag (111) QE

Cu (110) QE

Ag (110) QE

Cu (100) QE

Ag (100) QE

Figure 6.4: Calculated QE as a function of the photon energy for the three copper and silver surfaces. The energy axis is shown between 2 and 10 eV and the QE axis between 0 and 3 x 10^{-3}. This setup is maintained for all copper and silver QE plots reported here in order to provide an easier comparison among different graphs.

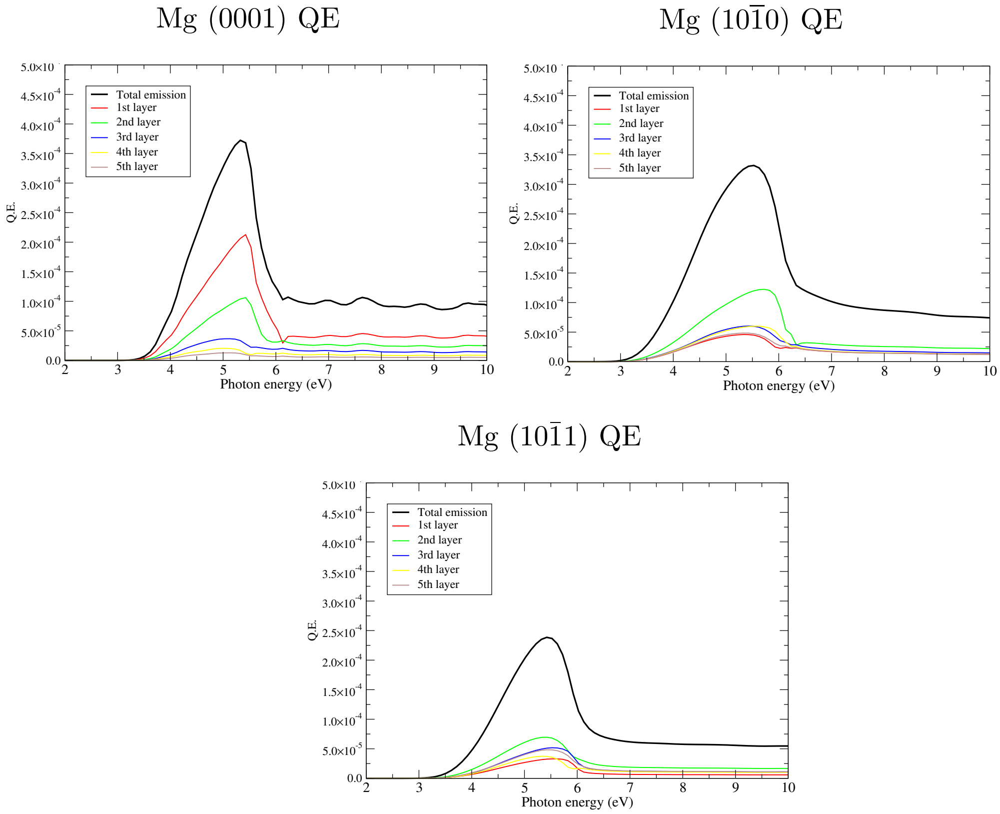

Figure 6.5: Calculated QE as a function of the photon energy for the three magnesium surfaces. The energy axis is shown between 2 and 10 eV and the QE axis between 0 and 5 x 10^{-4}. This setup is maintained for all the magnesium QE plots reported here in order to provide an easier comparison among different graphs.

of copper, according to the Wulff construction. Therefore, the first design strategy to improve the efficiency of photocathodes would be using single crystals exhibiting the most efficient surfaces.

Another aspect that can be investigated from the electronic structure of the material, in particular from the momentum DOS is the emittance of the material. This was briefly discussed in Section 4.2.1 and will be explored in the future of the project. These computed values are primarily intended to reveal trends in variations of QE with surface modification. They are, nevertheless, in general agreement with measurements of the absolute QE measurements made on these metals. These range between 10^{-6} and 10^{-3} measured for polished and mirror like samples in vacuum [118] for copper and silver. The QE of magnesium is higher and values between 10^{-4} and 10^{-3} are usually accepted for the wavelength range used here [118]. These results are in reasonable agreement with the quantum efficiency simulated in this work.

6.2 Electric Field Induced Modifications of Clean Surfaces

In this section, the effect of an external electric field on the photocathode surface is discussed. In photoinjectors, the photocathode is generally negatively biased. This creates an electric field which enhances the electron emission and accelerates them towards the LINAC. If the field is weak enough to have a negligible effect on the distribution of states on the near surface region its main effect may be modelled as a simple shift of the surface potential. This is equivalent to a reduction of the workfunction according to the Schottky effect. The so-called *effective WF* (Φ_{eff}) can be calculated [118, 125] according to:

$$\Phi_{eff} = \Phi_0 - e^{3/2}\sqrt{\frac{E}{4\pi\epsilon_0}} \tag{6.2}$$

where e is the electron charge, ϵ_0 is the vacuum permittivity and E is the electric field in units of V/m. This approximations holds for electric field values lower than 10^8 V/m [126]. In this approximation, the same electronic structure computed when no external field is applied is used. The only difference is a shift in the surface potential.

The difference between the WF and the effective WF was calculated at E field of 10, 20 and 100 MV/m for the copper (111) surface and is reported in Table 6.2. The lowering starts to become significant only for E fields of 100 MV/m, which lowers the WF by 0.38 eV. Also the QE at $\hbar\omega$ =4.7 eV is reported in Table 6.2. An external field of 20 MV/m, which is the one that is going to be used in the CLARA photoinjector [2]

Table 6.2: Work function change and quantum efficiency with respect to the clean surface at photon energy of 4.7 eV for external electric field of 10, 20, 1000 MV/m, for the copper (111) surface. QE_0 refers to the QE of the surface when no field is present.

	10 MV/m	20 MV/m	100 MV/m
ΔWF (eV)	-0.118	-0.168	-0.378
$\mathbf{QE/QE_0}$ ($\hbar\omega$ =4.7 eV)	1.4	2.1	6.0

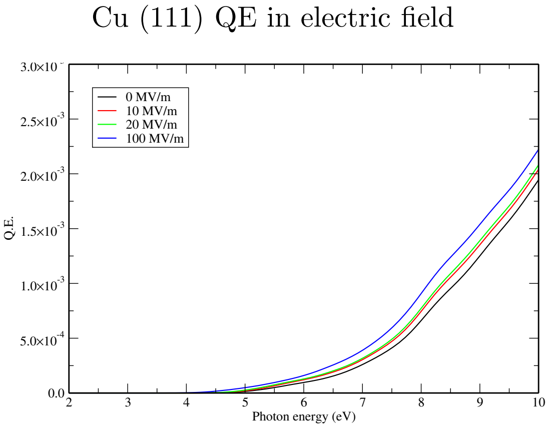

Figure 6.6: QE vs. photon energy plots for the copper (111) surface for electric fields of 10, 20 and 100 MV/m. Only the total emission is depicted. The emission in absence of the electric field is shown in black as a reference.

and is predicted here to enhance the QE by a factor of 2. For high intensity fields, such as the 100 MV/m used here the calculated enhancement is by a factor of 6.

The QE vs. photon energy plots for the three electric fields are depicted in Fig. 6.6. Only the total emission is shown. The black curve represents the QE in absence of external field and is depicted as a reference. In this approximation as expected, the shape of the curves does not change at increasing fields, only the emission onset is shifted towards lower photon energies.

6.3 Surface Stress

The effect of stress on the surface was simulated by running calculations where the lattice parameters are reduced by 1%, 5% and 10%. These values were chosen as a test case. The change in surface energy, WF and QE following these modifications is reported in Table 6.3.

Table 6.3: Surface energy and work function change and quantum efficiency with respect to the non compressed surface at photon energy of 4.7 eV for compression of 1%, 5% and 10%, for the copper (111) surface. QE$_0$ refers to the QE of the surface when at its relaxed geometry (no compression).

	1%	5%	10 %
$\mathbf{E_{surf}/E_{surf_0}}$ (J/m^2)	1.04	1.56	4.07
$\mathbf{\Delta WF}$ (eV)	-0.04	-0.14	+0.05
$\mathbf{QE/QE_0}$ ($\hbar\omega$ =4.7 eV)	1.7	9.0	4.9 x10^{-3}

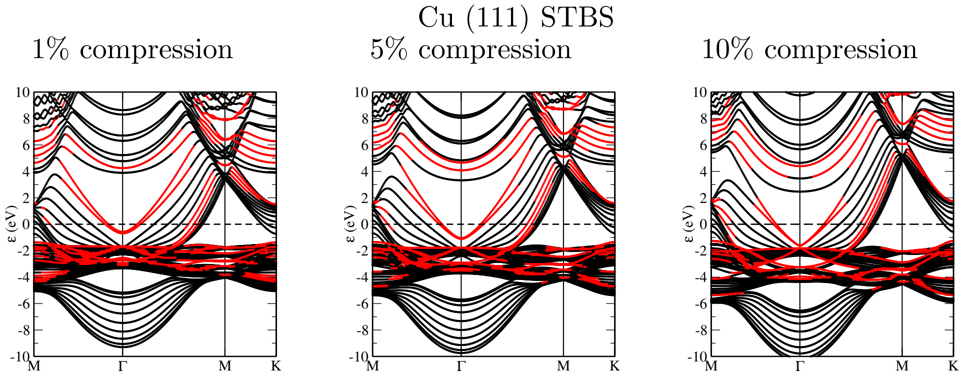

Figure 6.7: Copper (111) surface band structure for 1%, 5% and 10% compression. Surface states, identified according to the procedure described in Section A.5.1 are depicted in red. States equally delocalised on the whole slab are shown in black.

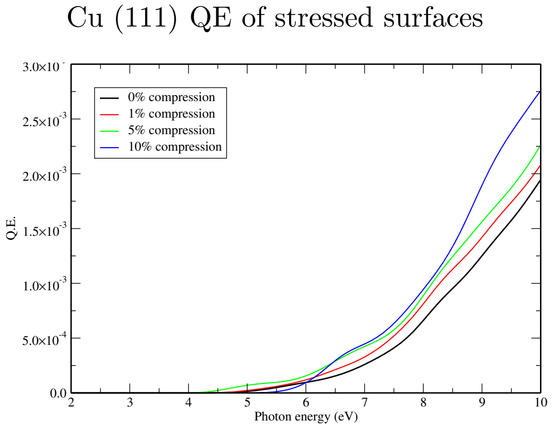

Figure 6.8: QE vs. photon energy plots for the copper (111) surface at compression of 1%, 5% and 10%. Only the total emission is depicted. The emission of the relaxed surface is shown in black as a reference.

The surface energy increases by only 4 % for a 1 % compression. Although the WF change is only of 0.04 eV, the QE increases by 70 %. The explanation for this behaviour can be found in the shift closer to the Fermi level of the two surface states in **Γ**, see Fig. 6.7. At 5 % compression the surface energy becomes noticeably higher, increasing by more that 50 % with respect to the relaxed one and its QE is nine times higher. At 10 % compression an inversion of trend is observed: the calculated QE is lower than the clean surface. Also, the surface energy of this structure is four times higher than the relaxed one, making it very unstable. In Fig. 6.8, the total QE vs. photon energy for the three compression and the relaxed one is depicted. Differences in the relative QE can be observed in the low photon energy region due to the shift of surface states near the **Γ** point.

These preliminary calculations on the effect of surface stress highlighted that the WF is rather insensitive to the amount of stress, whereas the positioning of surface states is affected. This could lead to design strategies based on the growth of metallic films on substrates which present a mismatch of the lattice with respect to the metal one in order to introduce the amount of stress leading to an increase of QE. This and other design strategies are discussed in more details in Chapter 9.

7

Chemistry at the Mg (0001) Surface

In the previous chapter, the three step model based on first principles calculations for computing the photoelectron yield, presented in Section 4.2.2 was validated in studies of clean copper, silver and magnesium surfaces. In order to achieve a more rational design of photoemitting materials, what is more valuable is the ability to generate trends to explain and predict the effect that surface modifications will have on the final emission process.

In this chapter, the changes induced on the surface properties by the presence of adsorbates at various coverages are discussed. In particular, we seek to disentangle the effects of the surface bond formation and charge transfer between the metal and adsorbed species for the three model systems that are studied here. In consultation with the ASTeC group, taking into account the practicality of materials that can be used and the systems currently being explored for use as photocathode materials, the adsorbates that were tested in the simulations presented here are oxygen, hydrogen and cesium. Oxygen was chosen as it is a well known contaminant of photocathodes in FELs. This is because materials are usually transported in air between the preparation chamber and the photoinjector and oxygen has a very high reactivity towards metal surfaces. It is also an excellent exemplar of a strongly interacting electron withdrawing species from the substrate. Hydrogen was simulated because it is always present in the photoinjector, even at high vacuum and so is likely to be present on any practical realisation of a photocathode. Cesium was chosen as it has been extensively studied as a candidate for enhancing the quantum efficiency [127] based on the fact that its low electronegativity suggests strong charge transfer to the substrate and thus a lowering of the WF [128, 129].

The discussion of the adsorbate effects will be restricted to the Mg (0001) surface, for which all aspects are discussed thoroughly. This facet was also chosen because of the large availability of experimental and computational data reported in the literature for the adsorption of the species discussed in this chapter. Coverages of 25 %, 11 % and 6 % were simulated.

7.1 Geometry and Energy of Adsorption

On the basal plane (0001) surfaces of hcp crystals, four high symmetry adsorption sites are available: hcp, fcc, on top and bridge as shown in Fig. 7.1. The top site (A in Fig. 7.1) is located above one of the atoms of the surface and has coordination of one. The bridge site (B in Fig. 7.1) is across two surface atoms and has coordination of two. The hcp site (C in 7.1) corresponds to the position characteristic of the bulk. The fcc site (D in Fig. 7.1) is the position that the atom of the next layer would occupy in a fcc crystal. The coordination of the first neighbours is the same for the latter two adsorption sites, the difference is in the second nearest neighbours, which is the arrangement of the atoms in the second layer below the adsorbate. The top and bridge configurations are reported to be unstable (for example, E_{ads}= 0.2 - 0.8 eV/atom for hydrogen, DFT-PW results [130]). Differences in the adsorption energy between the hcp and fcc sites of the order of 0.1 eV/atom, for all three of the adsorbates studied here, are reported in literature from DFT studies [130, 131]. This suggests that the local coordination is dominant in determining the binding energy and in what follows the adsorbate is therefore considered to be located in the hcp three fold hollow site of the surface.

Supercells are used in order to simulate coverages, Θ (defined as the coverage when all hcp sites are occupied) [43] lower than one. In total three supercells were chosen. Their size and the corresponding coverage is reported in Table 7.1. The surface energy of the clean supercell was calculated and it corresponds to $N \times E^{p}_{surf}$, where E^{p}_{surf} is the surface energy of the surface primitive cell for a certain surface and $N = \frac{n_p}{n_s}$ (n_p and n_s are the number of atoms in the primitive and supercell, respectively) gives the order of the supercell with respect to the primitive one.

Atoms in the slab (both substrate and adsorbate) are free to move in three dimensions during geometry optimisation. The optimised structures are depicted in Fig. 7.2. Only one adsorbate atom is present per unit cell. Therefore, the distance between adsorbates corresponds to the lattice parameter of the cell ($\mathbf{a} = \mathbf{b}$ for all supercell used).

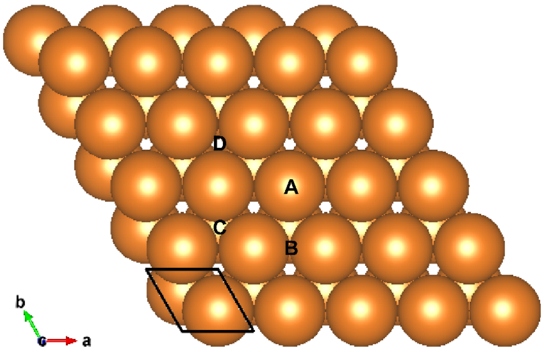
Mg (0001) adsorption sites

Figure 7.1: The four adsorption sites for the magnesium (0001) surface. **A**= top, **B**= bridge, **C**= hcp and **D**= fcc.

and it is reported in Table 7.1. Also the distance of the adsorbates from the surface (identified as the average z coordinate of the centre of the atoms in the topmost layer) is reported.

It is interesting to note that oxygen atoms, whose atomic and ionic radii are 0.66 Å and 1.26 Å respectively, are absorbed at 0.2 Å below the topmost metal layer for all the coverages studied here. The Mg-O bond length is only 12 % longer than the Mg-O bond length in crystalline bulk MgO (the XRD determined value is 1.75 Å for MgO, to compare with the 1.96 Å computed for the Mg-O distance between the adsorbed oxygen and the atoms on the topmost layer of the surface). The formation of subsurface oxygen layers has been reported in the literature and it is one of the steps for the oxidation of Mg surfaces, as discussed based on observations using XPS [131, 132] and previous DFT calculations [133–135].

Hydrogen atoms also occupy an interstitial position symmetric in the three fold hollow at about 0.8 Å above the surface layer [136] and has a 2.0 Å bond distance from the atoms in the hcp site.

Cesium, due to its large dimension (atomic radius of 2.98 Å [137] and ionic radius of 1.81 Å [138]) cannot penetrate the first layer as it can be observed from the bottom right panel in Fig. 7.2. Indeed, its bond distance from the atoms of the three fold hollow site is approximatively 5.0 Å .

The adsorption energies E_{ads} for the three adsorbates discussed in this chapter are calculated with respect to the elements in their standard state (diatomic molecule for oxygen and hydrogen and bulk for cesium) and they are reported in Table 7.1. Oxygen binds very strongly to the surface, with E_{ads} of about -5 eV/atom for all coverages.

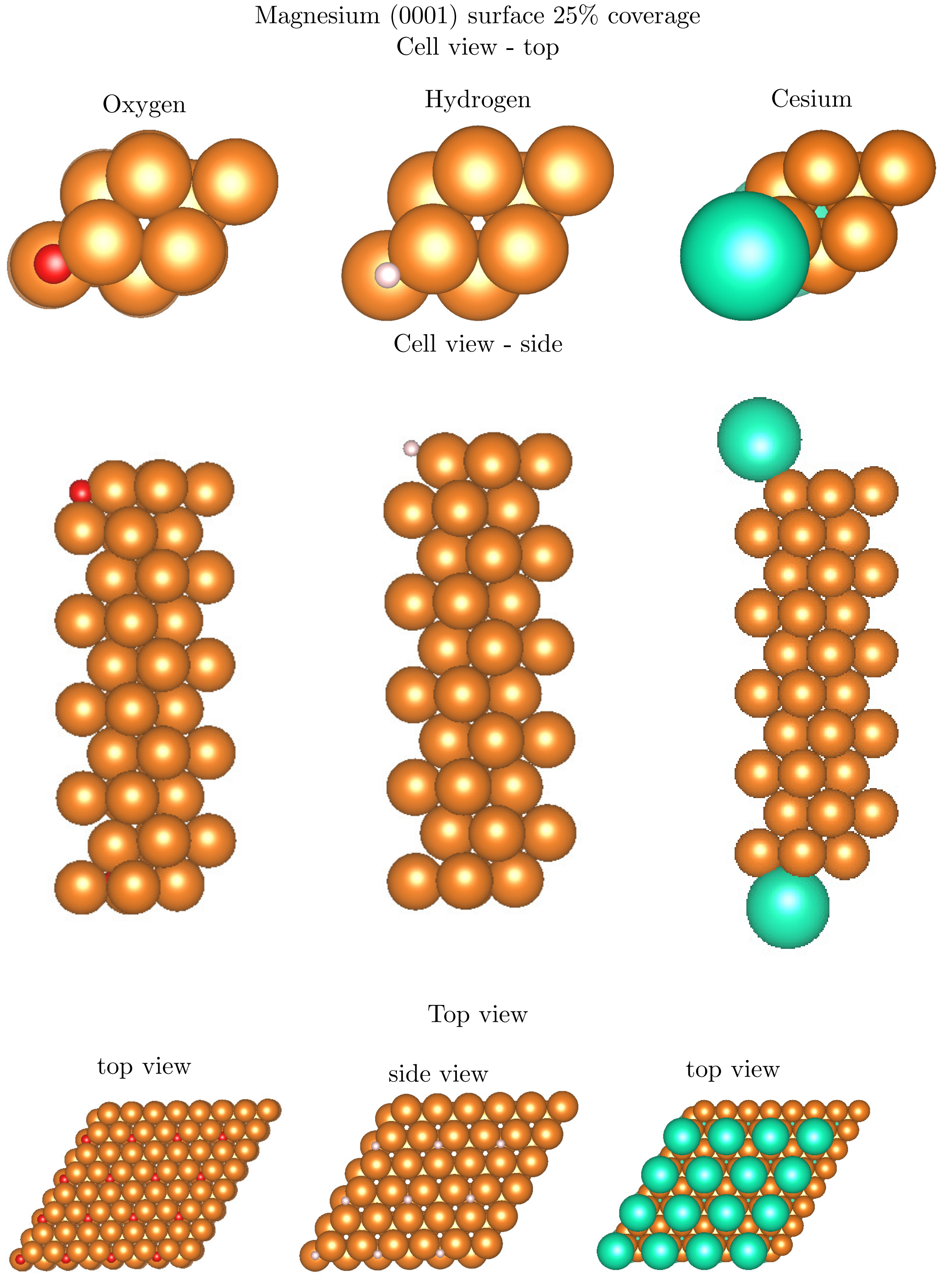

Figure 7.2: Structure of the supercells of magnesium interacting with oxygen, hydrogen and cesium used to model the adsorption on magnesium substrates at 25 % coverage. The van der Waals radius is used to depict the atoms. Magnesium atoms are depicted in orange, oxygen atoms are depicted in red, hydrogen atoms are depicted in white and cesium atoms are depicted in green.

Table 7.1: Adsorbate covered magnesium (0001) surface. The distance between adsorbates, the distance between the adsorbate and the surface top most layer (d_{surf}), the distance between one of the atoms of the three fold hollow of the hcp adsorption site ($d_{MgO-Ads}$), the adsorption energy (E_{ads}), change in WF and QE with respect to the clean surface are reported.

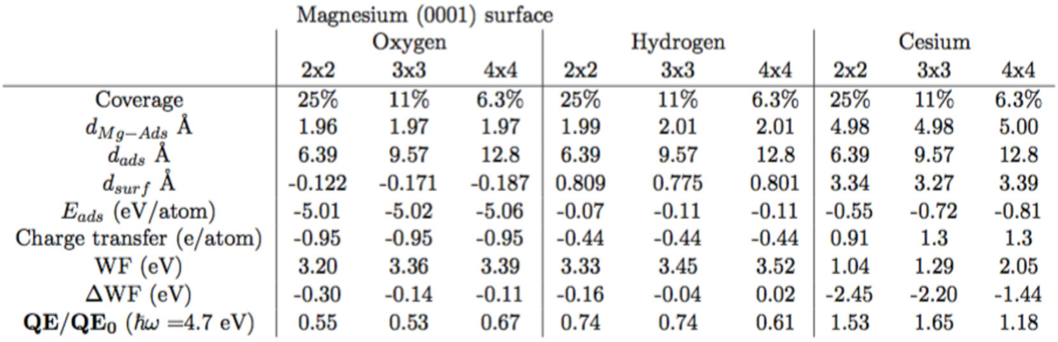

Magnesium (0001) surface

	Oxygen			Hydrogen			Cesium		
	2x2	3x3	4x4	2x2	3x3	4x4	2x2	3x3	4x4
Coverage	25%	11%	6.3%	25%	11%	6.3%	25%	11%	6.3%
d_{Mg-Ads} Å	1.96	1.97	1.97	1.99	2.01	2.01	4.98	4.98	5.00
d_{ads} Å	6.39	9.57	12.8	6.39	9.57	12.8	6.39	9.57	12.8
d_{surf} Å	-0.122	-0.171	-0.187	0.809	0.775	0.801	3.34	3.27	3.39
E_{ads} (eV/atom)	-5.01	-5.02	-5.06	-0.07	-0.11	-0.11	-0.55	-0.72	-0.81
Charge transfer (e/atom)	-0.95	-0.95	-0.95	-0.44	-0.44	-0.44	0.91	1.3	1.3
WF (eV)	3.20	3.36	3.39	3.33	3.45	3.52	1.04	1.29	2.05
ΔWF (eV)	-0.30	-0.14	-0.11	-0.16	-0.04	0.02	-2.45	-2.20	-1.44
QE/QE₀ ($\hbar\omega$ =4.7 eV)	0.55	0.53	0.67	0.74	0.74	0.61	1.53	1.65	1.18

Table 7.2: Electronegativity of the substrate and adsorbates discussed in this chapter, according to Pauling electronegativity scale [9].

	Mg	O	H	Cs
Electronegativity	1.31	3.44	2.20	0.79

This is similar to the adsorbtion energy reported in previous DFT-PW studies [133–135], (E_{ads} between -4.99 eV/atom and -5.22 eV/atom for different coverages [133]). Hydrogen adsorption is also a favourable process (negative adsorption energy), for the 11 % and 6 % coverages E_{ads} = -0.11 eV/atom is found. Previous literature reported E_{ads} between -0.2 eV/atom (DFT LDA results) and -0.5 eV/atom (for DFT PAW RPBE calculations) [139]. The adsorption energy for cesium is computed to be between -0.55 eV/atom at the 25 % coverage and -0.81 eV/atom for the 6 % coverage. The E_{ads} for cesium is much more coverage dependent than the oxygen and hydrogen. This can be explained in terms of their adsorption geometry. Since oxygen and hydrogen are positioned only a few tenth of Å at most from the centre of the surface layer, the interaction among adsorbate atoms is screened by the surface Mg atoms. In particular for oxygen, this mediation promotes the oxide formation at the surface as discussed in Refs. [133–135]. On the contrary, cesium atoms are adsorbed above the surface rather than as subsurface layers and the screening of the surface layer is not as strong as in the oxygen and hydrogen cases.

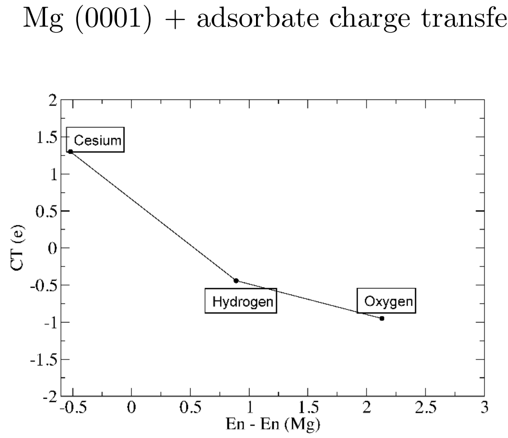

Figure 7.3: Charge transfer, calculated according to a Mulliken population analysis, for three adsorbates plotted as a function of the electronegativity difference with Mg for the 6 % coverage.

The charge transfer between the adsorbate and the substrate is another useful parameter to understand the type of substrate-adsorbate interaction. The electronegativity values of magnesium and the adsorbates are listed in Table 7.2. More electronegative atoms will withdraw electron charge from the surface and vice versa. This is confirmed by Fig. 7.3, where the charge transfer is plotted against the electronegativity of the adsorbed atoms with respect to the magnesium electronegativity. The electronegativity of oxygen, according to Pauling scale [9] is 2.13 units higher than the magnesium electronegativity. Therefore, each oxygen atom takes about 1 e of charge from the substrate, according to a Mulliken population analysis [140]. Also hydrogen is characterised by higher electronegativity than magnesium (0.89 units higher) and it tends to attract electrons from magnesium and about 0.5 e/atom is transferred. As for E_{ads} these values are not coverage sensitive because of the mediation of the Mg surface atoms. Cesium being less electronegative (0.52 units) than magnesium transfers between 0.9 and 1.3 e/atom to the surface. Since the transfer for the 11 % and 6 % coverages is the same, it appears this is the maximum charge that will be transferred at low coverages. However, studies on larger supercells should be carried out in order to test this hypothesis. The nearly linear trend found in the charge transfer (CT) vs. electronegativity plot (Fig. 7.3) is useful to predict the charge transfer of different adsorbates from their electronegativity, which is a tabulated value.

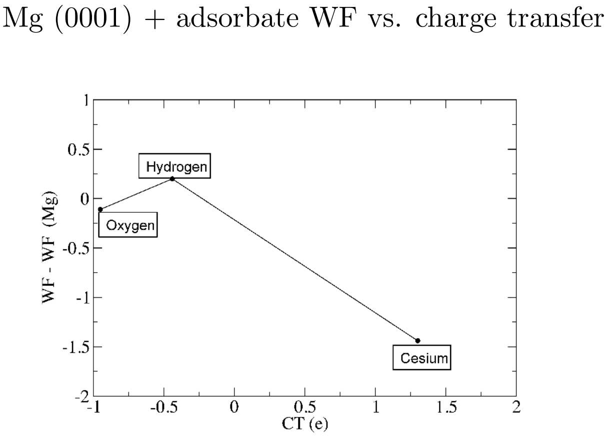

Figure 7.4: WF of the 6 % adsorbate covered Mg (0001) surfaces with respect to the the pristine surface as a function of the charge transfer induced by the adsorbate.

7.2 Work Function of the Adsorbate Covered Surfaces

The change in work function upon adsorption of oxygen, hydrogen and cesium on the Mg (0001) surface with respect to the pristine surface is reported in Table 7.1 and shown in Fig. 7.5.

In previous studies [141], the WF trend was computed to follow the CT trend: adsorbates transferring electrons to the substrate would create a dipole with the positive part pointing outside the surface and decrease the WF and vice versa. The Mg (0001) surface simulated here, represents an exception to this trend as shown in Fig. 7.4, where the WF vs. CT is depicted.

In contrast to the near linear correlation of the CT with the electronegativity difference (Fig. 7.3), the variation in the WF does not have a simple monotonic behaviour as a function of the CT (Fig. 7.4). It appears that other effects influence the change in WF as discussed in the following. For the adsorption of oxygen and hydrogen, despite the substrate to adsorbate charge transfer, the computed work function for the Mg (0001) surfaces covered with these two adsorbates is lower than the one computed for the pristine surface. This can be explained in terms of the dipole that is created by the adsorbate atoms. Since the adsorbed oxygen atoms form a sub-layer, the resulting dipole has the positive part pointing outside the surface. The WF change is more coverage dependent than the E_{ads}: a 25 % coverage of oxygen reduces the WF of the Mg (0001) surface by 0.3 eV and the lowering is 0.11 eV for the 6 % coverage. The effect of hydrogen is interesting because for the 25 % coverage, the WF change is computed

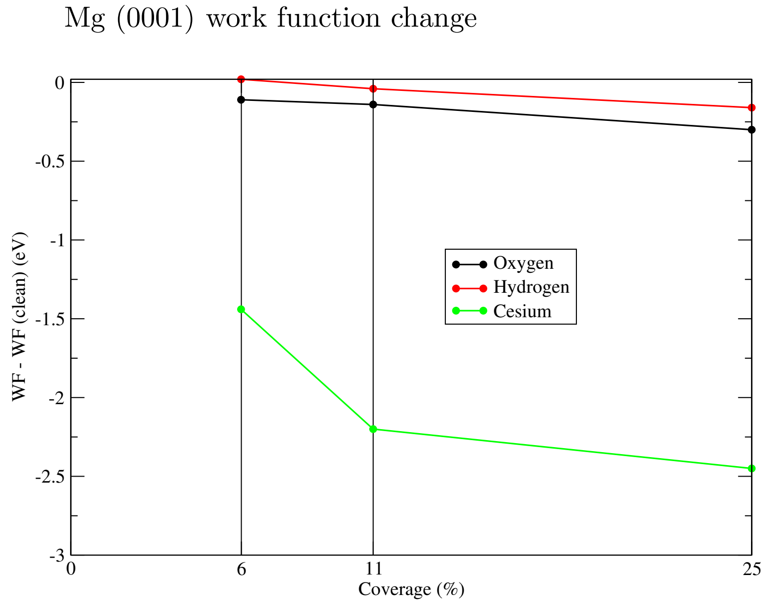

Figure 7.5: Adsorbate induced work function change as a function of the coverage for the O, H and Cs on the magnesium (0001) surface with respect to the pristine surface.

to be -0.16 eV, whereas, for the 6 % coverage an increase in WF is computed, however very small in magnitude: 0.02 eV. On the contrary, cesium atoms as they are adsorbed above rather than below the topmost layer, lower the WF of about -2.5 eV for the 25 % coverage and still -1.44 eV for the 6 % coverage. Further studies on lower coverages must be carried out in order to understand the range of coverages for which the WF lowering is significative for the Cs adsorption. Studies on lower coverage reported here suggest that the effect is significative also at low coverage, which makes it an interesting type of surface modification in order to increase the QE.

From the correlation between WF and CT discussed in this section it appears a model based on simple electrostatic could be developed for species that are adsorbed above the surface layer and form a dipole (either pointing inside or outside the surface) that is positioned above the topmost layer rather than as intra-layer. This simple model could be used to screen different adsorbates according to their atomic/ionic radius, which will determine whether they are adsorbed above the top most layer or as a subsurface layer and their CT, which was computed to depend on their electronegativity. Further studies to confirm this simple model can be considered to be predictive will be carried out.

7.3 Electronic Structure of the Adsorbate Covered Surfaces

The difficulty connected to the interpretation of the band structure of supercells has been discussed in section 4.2.1. Therefore, for the coverages studied here, the DOS and PDOS are used instead of the band structure to describe the changes in the electronic structure of the Mg (0001) surface induced by the adsorbates. The PDOS on the adsorbate atoms allows for an easy visualisation of the energy range where the additional states are introduced by the adsorbate. However, the information about the **k** point where the extra states are localised is lost. The PDOS on the adsorbate layer and the topmost Mg atom are depicted in Figure 7.6 for the 25% coverage of the three adsorbates. The clean surfaces PDOS on the Mg surface atom is shown for the sake of comparison.

The additional states introduced by the adsorbates will:

1. increase the QE if they are introduced in the valence band or in the conduction band above the vacuum energy

2. have no effect on the QE if they lie in the conduction band at energies lower than the vacuum energy

3. decrease the QE if they shift surface states present in the valence band of the clean surface to lower energy

The additional states introduced by the oxygen are localised at -5 eV with respect to the Fermi level. By comparing the PDOS on the first layer of the substrate it is possible to see that there is a lowering in the number of states with respect to the clean surface (see Fig. 7.6). For hydrogen the situation is very similar to the oxygen one: additional adsorbate state at -6 eV with respect to the Fermi level and lowering of the Mg surface states (compare the black and green curves in the top panel of Fig. 7.6). Therefore, both oxygen and hydrogen are representative of point three in the list above. Cesium states are more dispersed in energy than the oxygen and hydrogen ones, they are computed to be between -1 eV and +4 eV with respect to the Fermi level. Also, the adsorption of cesium increases the PDOS on the surface Mg atom, as can be noted by the the difference between the green and black curves in the plot at the bottom of Fig. 7.6. This is the effect discussed at point one in the list above. These effects on the computed QE are discussed in the following.

Mg (0001) + 25 % O

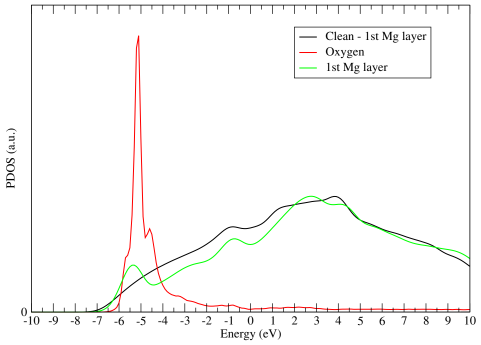

Mg (0001) + 25 % H

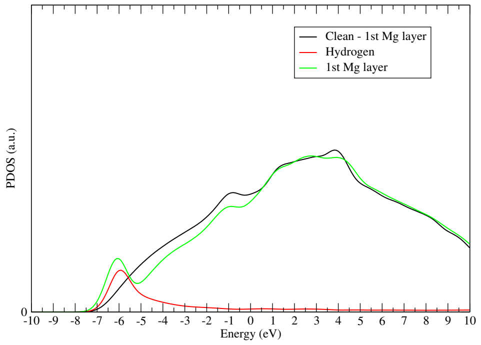

Mg (0001) + 25 % Cs

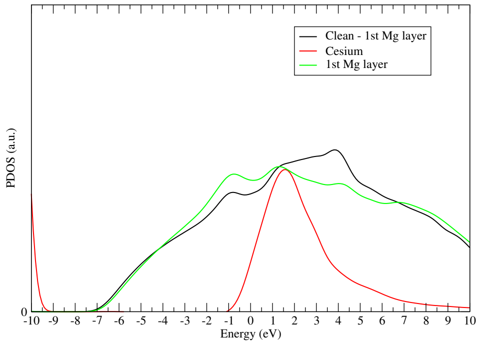

Figure 7.6: PDOS for the adsorbate covered Mg (0001) surface. The structures represented correspond to a 25 % coverage of adsorbates. States projected on the adsorbate atoms are shown in red, states projected on the substrate top most layer are shown in green and states projected on the top most layer of the clean surface are shown in black.

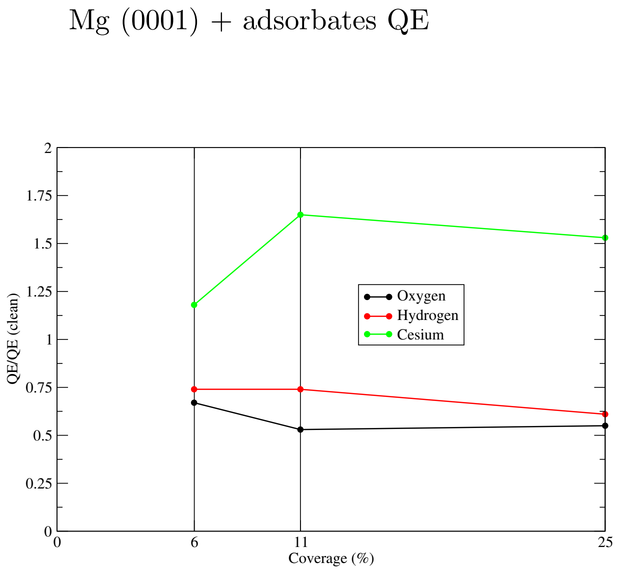

Figure 7.7: Adsorbate induced QE change as a function of the coverage for the O, H and Cs on the magnesium (0001) surface. Values are normalised with respect to the QE of the clean surface.

7.4 Quantum Efficiency of the Adsorbate Covered Surfaces

The QE change induced by the adsorbates with respect to the clean surface is discussed in this section. In order to calculate the QE of supercells, one more approximation with respect to the clean surface has to be used. This is due to the bands folding discussed in Section 4.2.1. Therefore, the term $H(q_\perp > 0)$ of Eq. 6.1 is neglected and emission is allowed from any **k** point. This approximation will not affect the conclusion drawn here which rely on trends of the same surface as clean and interacting with various coverages of adsorbates.

The total QE normalised with respect to the quantum efficiency of the clean surface (QE_0) is reported in Table 7.1 for all the coverages studied here. The QE simulations reveal the combined effects of the WF and electronic structure variations. For example, the oxygen covered Mg (0001) surfaces exhibit lower WF combined with less surface states and the latter has the larger influence. Indeed, the total QE is half the one computed for the clean surface for the 25 % coverage and still 33 % lower for the 6 % coverage. The same situation is found for hydrogen, even if the effect is less noticeable, being the reduction only 26 % for all coverages. The cesium over-layer both lowers the WF and introduces more states on the Mg surface layer, which means both effects lead to an increased QE situation. Therefore, the computed QE is higher than the one calculated for the pristine surface. However, the effect rapidly decreases with coverage: a 50 % increase is calculated for the 25 % coverage, but only a 18 % increase is computed for the 6 % coverage as expected by the smaller effect of the low coverage on the WF and lower number of states active for the photoemission.

This initial investigation of the influence of surface chemistry on the QE, using the theoretical approach and its implementation in the current work has provided some general insights into the influence of the presence of adsorbates on the QE of photoemitting materials. Often the WF is used in order to screen which material could give a higher QE. However, disentangling the two major effects and their variation with coverage has revealed that the density of surface states has a dominant effect on the QE and must be considered in conjunction with expected changes in WF in order to design more efficient photocathode materials. Also the importance of the atomistic details of the adsorption mode and that some ions may be sub surface was highlighted.

The conclusions about the influence of surface chemistry on the QE that can be drawn at this stage are summarised in Chapter 9.

8

Stepped Silver Surfaces

In this chapter we report on a preliminary study of the influence of other types of surface modifications on the QE of emitting materials, in addition to the presence of adsorbates, which was discussed in Chapter 7. The role of some particular surface reconstructions on the electronic properties and work function of silver surfaces is used as an exemplar of metal photocathode reconstructions.

There are several kinds of surface reconstructions (as summarised in this review [142]) and their relevance in many different fields is largely recognised and used to enhance materials properties through nanoengineering of surfaces [143,144]. A reconstruction is an altered periodicity relative to that implied by the bulk crystal structure [142]. These can be produced by:

- an ordered array of adatoms, which are atoms of the same species of the substrate on top of a surface;
- a vicinal cut, which is found between two surfaces when a bulk material is cut at a small angle with respect to the direction of a fixed surface;
- missing rows from a surface layer;
- mechanical (eg: strain) or chemical interactions that lead to spontaneous rearrangement of the surface layer.

In this chapter, stepped silver surfaces are discussed in terms of their geometry, surface energy, electronic structure and work function.

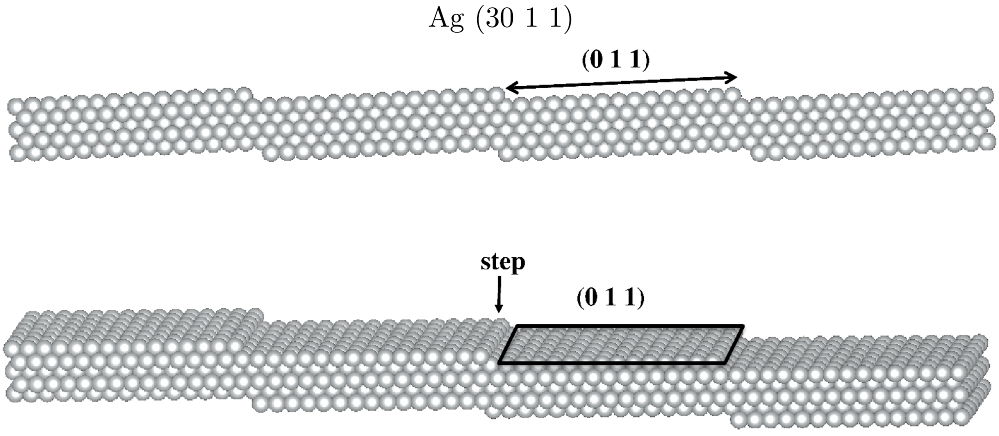

Figure 8.1: Structure of the Ag (30 1 1) surface.

8.1 Geometry and Surface Energy

In order to simulate the steps at a Ag (111) surface, the series of the Ag (x11) surfaces, where x is an odd number between 3 and 9, was selected. These are vicinal surfaces [145], which refers to the fact that they are obtained when a bulk material is cut along an angle with respect to a certain surface, the (111) in this case. In the limit where x becomes very large, the geometry of the (011) surface is recovered. The steps exhibit the (111) surface geometry. This is shown in Fig. 8.1, where the Ag (30 1 1) surface is depicted and the regions corresponding to the Ag (011) surface are highlighted. In the Ag (30 1 1) surface the steps are occupying only one every sixteen available surface sites leaving large portions of the Ag (011) surface unchanged as (011) plateaux.

The structure of the slabs used to simulate the vicinal surfaces discussed in this chapter is shown in Fig. 8.2. The flat regions correspond to the (011) surface and larger portions of this surface can be observed in the (911) surface among the ones studied here. The number of steps per unit area increases going from the (911) surface, where a step is found every six atoms of the (011) surface to the (311) surface, where a step is found every two (011) surface atoms.

The atoms at the steps have lower coordination with respect to the atoms of the pristine (111) surface. Therefore, the vicinal surfaces are expected to have higher surface energy compared to the atomically flat one. The surface energy of the slabs discussed in this chapter is reported in Table 8.1, where it is compared to the Ag (111)

Ag (311)

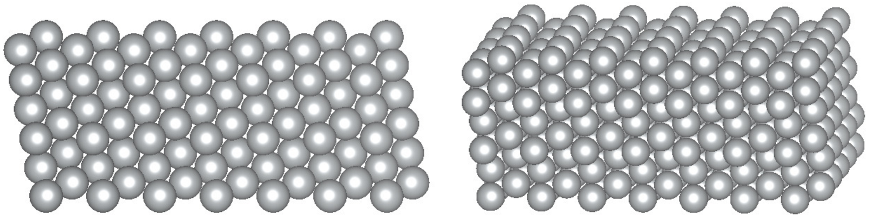

Ag (511)

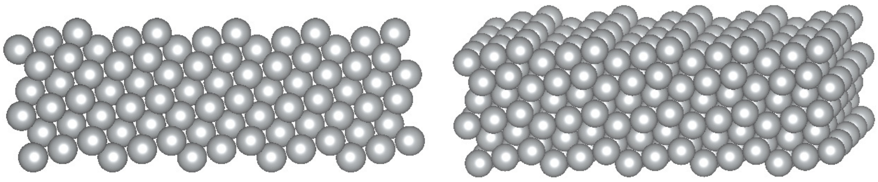

Ag (711)

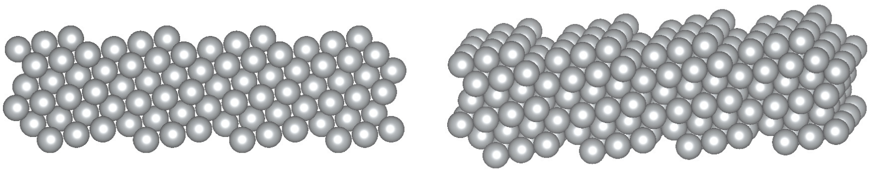

Ag (911)

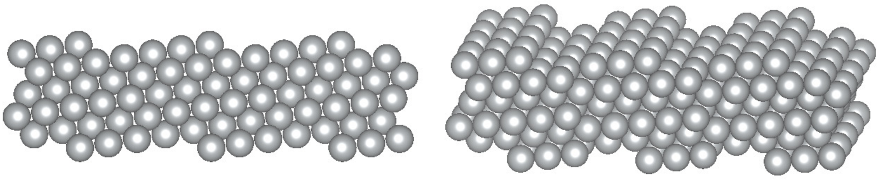

Figure 8.2: Structure of the slabs used to model the vicinal surfaces of silver discussed in this chapter.

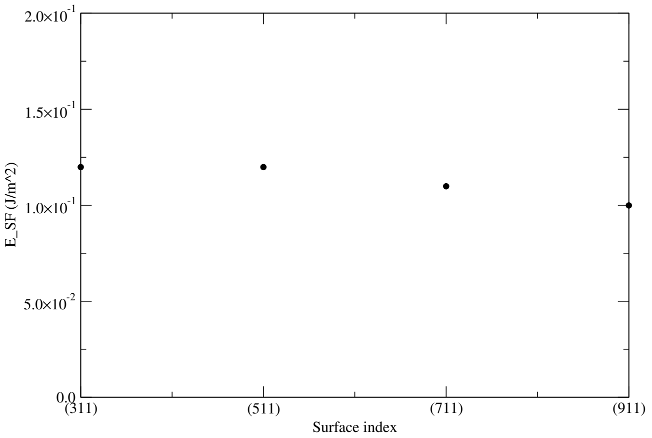

Figure 8.3: Step formation energy per unit area for the Ag (x11) stepped surfaces.

surface energy.

The surface energy of the stepped surfaces can be expressed as:

$$E_{surf}(x11) = \frac{A(111)}{A(x11)} \times E_{surf}(111) + E_{SF}/A(x11) \tag{8.1}$$

where E_{SF} is the step formation energy. The E_{SF} for the vicinal surfaces studied here is plotted in Fig. 8.3. The step formation energy per unit area is higher for the (311) surface. For the (x11) surfaces discussed, the E_{SF} is comparable to the thermal energy at room temperature (25.7 meV per degree of freedom). Therefore, steps are expected to form spontaneously on the Ag (111) surface as it increases its entropy.

As discussed above, at increasing x, the (x11) surface will exhibit the (011) surface properties. Therefore, the expected trend is a lowering of the surface energy, towards the (011) surface energy value, for increasing value of x. Indeed, the (311) and (511) surfaces have similar surface energy and for the (711) and (911) surfaces a decreased surface energy is computed.

Table 8.1: Surface energy and work function for the Ag (x11) stepped surfaces. Also the surface energy and work function for the pristine Ag (111) is reported.

	(111)	(311)	(511)	(711)	(911)
$\mathbf{E_{surf}}$ (J/m^2)	0.80	0.92	0.92	0.91	0.90
$\mathbf{E_{SF}}$ (J/m^2)	-	0.11	0.12	0.10	0.09
WF (eV)	4.25	3.93	4.11	4.14	4.07

8.2 Electronic Structure

In order to observe the modifications on the electronic structure of the (111) surface introduced by the steps, the total DOS and the PDOS on the first layer of the vicinal surfaces discussed above was calculated and is shown in Fig. 8.4. Also the (111) DOS and PDOS on the first layer is shown as the thick black line in the figure. Differences between the electronic structure of the vicinal surfaces and the pristine one are small. An increased number of states in the region between -3 eV and -5 eV with respect to the Fermi energy can be observed in the DOS (left panel of Fig. 8.4). Through the PDOS on the surface layer, this increase can be attributed to the topmost layer highlighting the presence of extra surface states introduced by the steps. However, this increase is small if compared to the height of the peak.

According to this analysis, the presence of steps simulated through the vicinal surfaces chosen in this chapter is not expected to significantly change the electronic structure of the Ag (111) surface.

8.3 Work Function

The presence of steps changes the potential at the surface and therefore it is expected to change the WF of the surface. The work function of the Ag (x11) surfaces was computed and is reported in Table 8.1 as its absolute values and as difference with respect to the WF of the Ag (111) surface ($\mathrm{WF}_{Ag(111)} = 4.25$ eV). These differences are also plotted in Fig. 8.5. For all the surfaces discussed in this chapter the presence of steps decreases the WF. However, such change is small in magnitude, between 0.11 eV and 0.33 eV.

In conclusion, the presence of steps on the Ag (111) surface increases the surface energy of few tenth of J$/m^2$, which makes them stable at room temperature. The most interesting effect due to the introduction of steps is the lowering of the WF. As it was

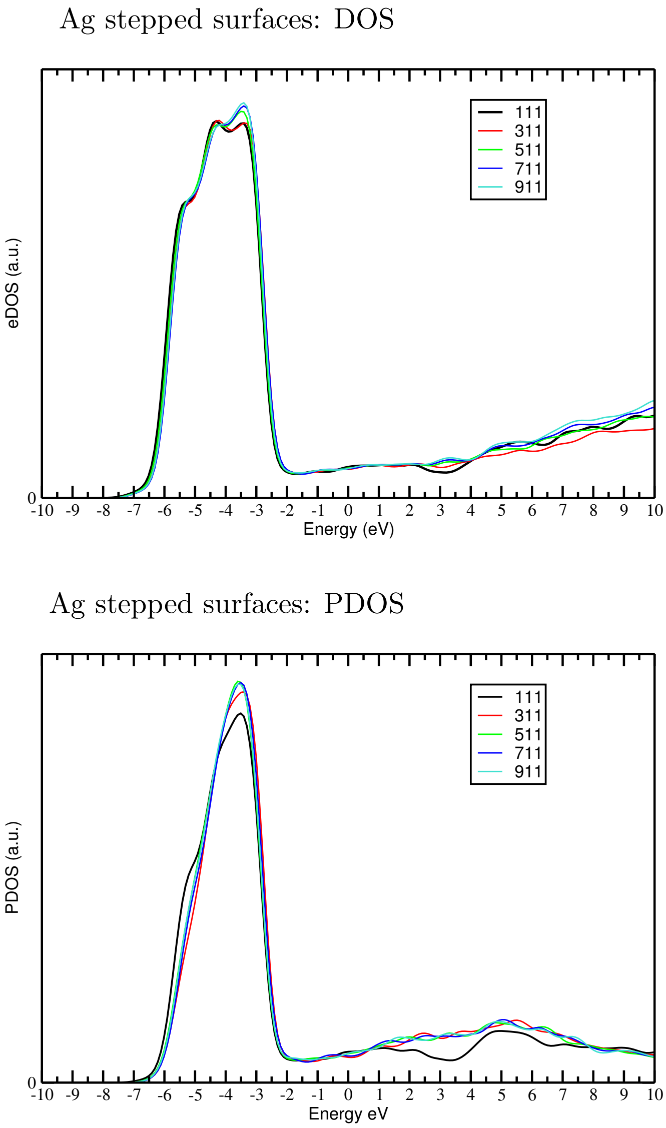

Figure 8.4: Electronic structure of the the Ag (x11) stepped surfaces. Top: total DOS. Bottom: PDOS on the topmost atomic layer. The Ag (111) surface DOS and PDOS are shown in black in the top and bottom panels, respectively.

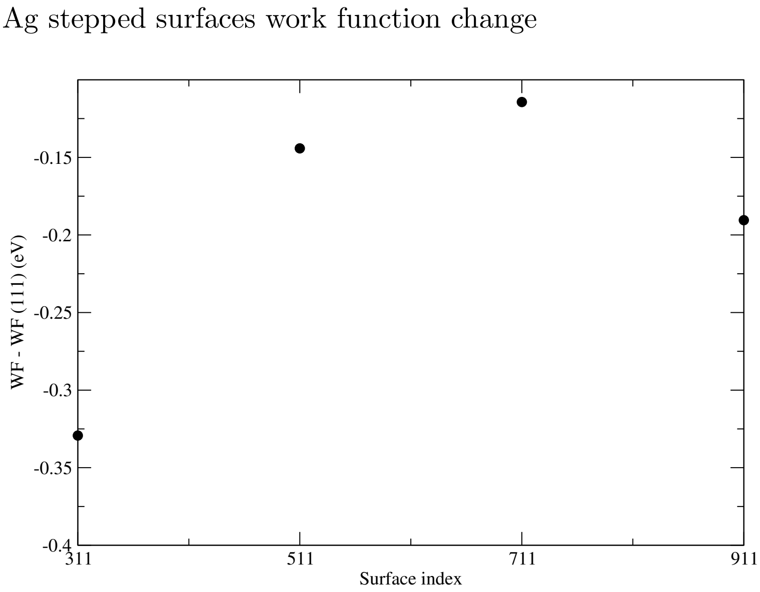

Figure 8.5: Work function change for the Ag (x11) stepped surfaces with respect to the Ag (111). The surfaces are reported according the increasing concentration of steps per surface unit.

discussed in Chapter 6.3, also small variations in the WF can lead to large variations in the QE.

The surface reconstruction is a wide and very promising field to tune the properties of materials thanks to the very advanced techniques available nowadays, such as atomic force microscopy-based lithography techniques [146]. This chapter is only meant to show another path apart from the adsorption of species on the surface that could be taken to generate more efficient materials for photocathode applications. More detailed studies on stepped surface and other types of reconstructions should be undertaken in order to be able to provide reliable information able to help experimentalists in the synthesis of new materials. Nevertheless, in this chapter it was proved that a systematic approach to surface reconstructions, such as the study of series of the vicinal surfaces is able to highlight trends and what kind of properties will be influenced by the reconstruction. In the future of this project other reconstructions on Ag surfaces and other materials will be studied.

9

Towards the Efficient Design of Materials

In this chapter the findings of this work are summarised and their potential application to photocathode design is explored. It can be imagined as the answer to the question from a photocathode scientist asking: “what can I learn from the photoemission simulations presented here to help me select better materials or surfaces in order to achieve higher performances for my photocathodes?”

The first outcome of this work is not a guideline itself, but it is a tool in the form of a piece of theory that fills the gap between highly accurate photoemission theories applicable to simple systems and what is required for the design of materials, which is being able to describe the real conditions where the material is operating. The development and implementation of this theory took half of the time employed in this project (about 1.5 years). The advantage of this tool, with respect to previous theories is being able to take into account the effect of surface modifications on the QE of material. Also, it allows for a disentangling of the different effects on the final computed QE, which is essential in order to understand what are the relevant factors impacting the efficiency and therefore providing guidelines for the design of new materials. The disadvantage is a loss of accuracy due to the relatively simple treatment of the coupling of excitations with the scattering states of the surface (the inverse LEED states).

Considerations of changes in the WF alone is often used to select the best photoemitting materials, based on the assumption that a higher QE corresponds to a lower WF. In this study it was found that the WF has certainly a major role in the selection of photoemitting materials. However, other factors, such as the electronic structure of the material must also be considered.

In Chapter 5 the structure of the substrates simulated in this work (copper, silver and magnesium) is thoroughly discussed in terms of geometry, energetics and electronic structure. The three most stable surfaces for the three substrates are simulated through the thin slab approach and their properties are discussed. Among the most relevant ones, the WF is computed and their surface states are highlighted in the band structure and PDOS. The photoemission theory developed here is facet dependent, in order to calculate the averaged properties (such as WF and QE) to compare to the measurements on a polycrystalline sample, an approach based on the Wulff construction is proposed. The Wulff construction is used to build a polyhedra predicting the shape of a nanocrystal and the fractional contribution from each surface can be calculated.

In Chapter 6 the tool is tested on clean surfaces and results are compared to experimental data. The QE computed through this method is only intended to generate trends among different materials or the same surface before and after surface modifications. Obtaining the exact photoemission spectra is not the goal of this project. Nevertheless, the computed QE is in general agreement with the experimental measurements of QE for the materials studied here.

Two external factors that can modify the efficiency of clean surfaces are simulated at the end of this chapter: the effect of an external electric field and the compression of the material along the plane parallel to the surface. The former is simulated as a lowering of the work function through Schottky effect and it corresponds to an increase of the QE that is significant starting from fields of 20 MV/m, for which the QE is twice as high as the pristine surface one. Typical fields in photoinjectors are in the range of 20 MV/m. When an external electric field is applied, the change is only on the work function and not on the electronic structure. On the contrary, the electronic structure is changed by the compression of the material in the direction parallel to the surface. A shift of surface states was reported together with changes in the WF. The latter is, however, not significative for compressions of 1 % and become significative only at high compression. The QE variation is noticeable already at 1 % compression, where an increase of 70 % was computed. This latter finding is interesting from the design point of view. The introduction of strain on the surfaces does impact the QE. One way to introduce strain on the surface is growing thin layers of the photoemitting materials on a substrate, which can distort the lattice of the former because of a small mismatch of the lattice parameters between the two. This is just a first evidence this approach could be used to enhance the QE of materials and further studies will be carried out in this direction.

In Chapter 7 the influence of modifying the chemistry at the Mg (0001) surface was simulated through adsorption of oxygen, hydrogen and cesium atoms. The manipulation of surface chemistry is potentially a flexible and powerful way to tune the surface properties of materials. Oxygen and hydrogen were chosen because they are well know contaminant of photocathode surfaces and cesium is used experimentally in order to decrease the WF and increase the QE of photoemitting materials. The outcome from these preliminary simulations on the adsorption of external species is that variations in the WF alone is not a good predictor of the trends of QE according to the method discussed here (at least on Mg (0001) surfaces). Interestingly, the oxygen adsorption, which is known to increase the work function in most materials, has the opposite effect on Mg. This was explained in terms of its geometry of adsorption. The first atoms adsorbed on the Mg surface occupy hcp three follow holes and penetrate into the first layer of Mg atoms forming a precursor of the MgO structure. The electronic structure of this surface presents a lowering in the number of surface states, which explains the reduction in the computed QE. The adsorption of hydrogen causes minor changes in the work function and an overall decrease of photoactive surface states, resulting as for the oxygen in a lower efficiency with respect to the pristine surface. Cesium atoms are absorbed on the surface and cannot penetrate the first layer of Mg atoms because of their large atomic radius. This adsorbate withdraws electron density from the substrate and significantly lowers the work function, also it increases the density of states on the first Mg layer. The overall effect is an increase in the QE.

The range of possible chemical modifications is very large and these simple models provide only a preliminary survey of the effects of adsorbates on the QE of metal photocathodes. For example, the interaction of oxygen on magnesium surfaces is very interesting and subsurface layers of oxygen should be simulated. Also, MgO layers on Mg or other metals are an interesting field and will certainly be one of the future paths for this collaboration. Hydrogen has minor effects, but being present also at high vacuum it is worth further investigation.

The behaviour of cesium is expected to be representative of the alkali metals from the electronegativity point of view. Their lower electronegativity with respect to magnesium and other photoemitting materials (copper and silver for example) is expected to increase the QE through charge transfer effects. Therefore, the adsorption of smaller atoms such as Li on Mg surfaces should be investigated. As it was reported in Chapter 7, the dimension of the adsorbate has a crucial role in the WF and QE change. In this context, the simulation of Li atoms adsorbed on the surface would be an interesting to observe the effect of small electropositive atoms.

Also, once a model to predict how higher efficiency can be obtained in terms of charge transfer and positioning of the adsorbates on the surface, more complex molecules could be tested from the computational point of view using the model presented here. The best candidates can then be tested in operational environment in order to see if they are suitable for the high vacuum and strong laser pulses the photocathode is subject to in the photoinjector. These kind of combined computational and experimental tests will be carried out in the near future of the project (1-2 years).

The other interesting and largely tunable tool for surface modifications is reconstruction. Surface reconstructions have large impact on the surface potential and electronic structure of surfaces. Indeed, materials can be engineered for different applications through surface reconstructions. Also, surfaces in real conditions are not atomically flat, a certain (quantifiable through AFM experiments) amount of roughness is always present and this should be taken into account to provide reliable information about QE predictions. The first type of surface reconstruction tested here are steps on the Ag (111) surface, modelled through the series of the Ag (x11) vicinal surfaces. It was found that the surface energy of these surfaces is approximatively 0.1 J/m^2 higher than the Ag (111) surface one. The presence of steps slightly modifies the electronic structure through an increase of surface states close to the Fermi level and the WF is in general lower than the pristine surface.

The next step in the simulation of surface modifications will be modelling the adsorption of external species on the reconstructed surfaces. Also the role of interfaces between the metal and its oxide will be investigated. The knowledge gained from this first part of the project has already been shared with the ASTeC group, where experiments based on the findings reported here are being designed. Future simulations are expected to produce further insights on which are the most promising ways to engineer the photocathode surfaces in order to obtain more efficient materials.

10

Conclusions and Future Work

The purpose of this thesis has been delivering the photocathode community with a tool able to screen different materials and surface modifications in order to discover more efficient materials in a rational way rather than by the trial and error approach.

The reasons for the need of more efficient and reliable photoemitting materials has been pointed out in the introduction and further explained in the *Context and Background* chapter. A wide R&D program is taking place worldwide in order to deliver photocathodes able to satisfy the requirements of new generation light sources for high brightness of the electron bunch. These experimental and computational efforts are justified by the the new frontiers that are being reached through the new light sources.

After introducing the underlying theory of materials simulations, different approaches to photoemission simulations were discussed in Chapter 4 highlighting their advantages and limitations. The photoemission model developed in this work, based on an extension of the three step model to surface simulations was discussed in the same chapter. This model aims at simulating materials in real conditions and provide information able to design photocathodes in a rational way. In this context the ability to generate trends in order to guide the experimentalists into the field of surface chemistry and reconstruction is more important than being able to reproduce the experimental photoemission spectra of simple systems, for which other theories should be used.

In Chapters 5 the structural and electronic properties of copper, silver and magnesium surfaces were explored from the computational point of view. These are the materials that are going to be tested as photocathodes for CLARA and their properties are of great interest. Their geometry, surface energy, work functions and Wulff plots were computed and discussed in Chapter 5.

Chapters 6 to 8 contain the outcomes of the use of the model presented in Chapter

4 on the clean metal surfaces (Chapter 6) and some of the first applications to the study of surface chemistry and reconstructions (Chapters 7 and 8, respectively). The findings reported in these chapters have already been summarised in a photocathode design oriented way in the previous chapter and, therefore, will not be repeated here.

As for every research project, the one presented here was limited by time constraints. The development of a tool able to give insights in the QE of materials was the first goal of the collaboration between ASTeC and the CMS group at Imperial College and it was achieved in this first part of the project. However, other aspects of the emitted electron beam should be explored in order to achieve higher efficiency photocathodes. Because of the encouraging results obtained by this first part of the project, the ASTeC group and CMS group decided to continue working on the development of the tool discussed here and its use to guide the design of photocathodes. The ASTeC group recently obtained interesting data on the transverse emittance through their system called TESS (Transverse Energy Spread Spectrometer). The next step from the theoretical side is the inclusion of the emittance simulation in the code. At that stage the QE simulations will be able to deliver not only the QE vs wavelength, but also the corresponding emittance at that wavelength.

At the same time, the tool discussed here is mature enough to be used in order to start to screen efficiently other materials and surface modifications. These new results will guide the photocathode scientist of the ASTeC group at first and scientist among the whole photocathode field to design the materials for the next generation of XFELs.

Appendix A

Projected bulk band structure

A.1 Redefinition of Lattice Vectors

The primitive cell is defined by the lattice vectors **a**, **b** and **c**. The direct-lattice vectors can be represented by a matrix **A**

$$\mathbf{A} = \begin{bmatrix} A1_x & A1_y & A1_z \\ A2_x & A2_y & A2_z \\ A3_x & A3_y & A3_z \end{bmatrix}$$

If the cell is redefined with the condition that the lattice vectors **a** and **b** are in the specified plane and the reference frame is rotated so that this corresponds to the xy plane.

The redefined lattice vectors, two of which belong to the specified plane, can be represented by a matrix **B**:

$$\mathbf{B} = \begin{bmatrix} B1_x & B1_y & B1_z \\ B2_x & B2_y & B2_z \\ B3_x & B3_y & B3_z \end{bmatrix}$$

The transformation matrix for the transformation of **A** to **B** can be represented by a matrix **R** :

$$\mathbf{R} = \begin{bmatrix} r_{11} & r_{12} & r_{13} \\ r_{21} & r_{22} & r_{23} \\ r_{31} & r_{32} & r_{33} \end{bmatrix}$$

so that:

$$\mathbf{B} = \mathbf{R}\ \mathbf{A}$$

$$\begin{bmatrix} B1_x & B1_y & B1_z \\ B2_x & B2_y & B2_z \\ B3_x & B3_y & B3_z \end{bmatrix} = \begin{bmatrix} r_{11} & r_{12} & r_{13} \\ r_{21} & r_{22} & r_{23} \\ r_{31} & r_{32} & r_{33} \end{bmatrix} \begin{bmatrix} A1_x & A1_y & A1_z \\ A2_x & A2_y & A2_z \\ A3_x & A3_y & A3_z \end{bmatrix}$$

R can be expressed as a product of **F** and **P**:

$$\mathbf{R} = \mathbf{F}\ \mathbf{P}$$

$$\begin{bmatrix} r_{11} & r_{12} & r_{13} \\ r_{21} & r_{22} & r_{23} \\ r_{31} & r_{32} & r_{33} \end{bmatrix} = \begin{bmatrix} f_{11} & f_{12} & f_{13} \\ f_{21} & f_{22} & f_{23} \\ f_{31} & f_{32} & f_{33} \end{bmatrix} \begin{bmatrix} p_{11} & p_{12} & p_{13} \\ p_{21} & p_{22} & p_{23} \\ p_{31} & p_{32} & p_{33} \end{bmatrix}$$

P is the coefficients matrix for the linear combination of the original lattice vectors to define the new lattice vectors (for the redefined cell). **F** represents the rotation of the redefined cell so that the specified plane is in the xy plane. The determinant of the matrix **F** is equal to 1, since it is a rotation matrix.

It is useful to define the matrix **C**, which is obtained by multiplying **P** and **A**:

$$\mathbf{C} = \mathbf{P}\ \mathbf{A}$$

$$\begin{bmatrix} C1_x & C1_y & C1_z \\ C2_x & C2_y & C2_z \\ C3_x & C3_y & C3_z \end{bmatrix} = \begin{bmatrix} p_{11} & p_{12} & p_{13} \\ p_{21} & p_{22} & p_{23} \\ p_{31} & p_{32} & p_{33} \end{bmatrix} \begin{bmatrix} A1_x & A1_y & A1_z \\ A2_x & A2_y & A2_z \\ A3_x & A3_y & A3_z \end{bmatrix}$$

The **C** matrix correspond to the redefined cell before rotation of the frame in order to place the specified plane in the xy plane.

In summary,

$$\mathbf{B} = \mathbf{F}\ \mathbf{P}\ \mathbf{A}$$

and

$$\mathbf{R} = \mathbf{F}\ \mathbf{P}$$

and

$$\mathbf{C} = \mathbf{P}\ \mathbf{A}$$

so the following can be written:

$$\mathbf{B} = \mathbf{R}\ \mathbf{A}$$

$$\begin{bmatrix} B1_x & B1_y & B1_z \\ B2_x & B2_y & B2_z \\ B3_x & B3_y & B3_z \end{bmatrix} = \begin{bmatrix} r_{11} & r_{12} & r_{13} \\ r_{21} & r_{22} & r_{23} \\ r_{31} & r_{32} & r_{33} \end{bmatrix} \begin{bmatrix} A1_x & A1_y & A1_z \\ A2_x & A2_y & A2_z \\ A3_x & A3_y & A3_z \end{bmatrix}$$

In order to redefine the lattice vectors of a cell, the transformation matrix **R** is applied to the original lattice vectors.

A.2 Conversion from Fractional Coordinates to Cartesian

Fractional coordinates and Cartesian coordinates of atoms can be represented by vectors **f** and **r**, respectively.

In the primitive cell, the fractional coordinates $\mathbf{f_p}$ can be converted into Cartesian coordinates $\mathbf{r_p}$:

$$\mathbf{r_p} = \mathbf{A}^{\mathrm{T}}\ \mathbf{f_p} \tag{A.1}$$

In the same way in the redefined cell, the fractional coordinates $\mathbf{f_r}$ can be converted into Cartesian coordinates $\mathbf{r_r}$:

$$\mathbf{r_r} = \mathbf{B}^{\mathrm{T}}\ \mathbf{f_r} \tag{A.2}$$

A.3 Conversion from Cartesian Coordinates to Fractional

In the primitive cell, the Cartesian coordinates $\mathbf{r_p}$ can be converted into fractional coordinates $\mathbf{f_p}$:

$$\mathbf{f_p} = (\mathbf{A}^{\mathrm{T}})^{-1}\,\mathbf{r_p} \tag{A.3}$$

In the same way in the redefined cell, the Cartesian coordinates $\mathbf{r_r}$ can be converted into fractional coordinates $\mathbf{f_r}$:

$$\mathbf{f_r} = (\mathbf{B}^{\mathrm{T}})^{-1}\,\mathbf{r_r} \tag{A.4}$$

A.4 Redefinition of Cartesian Coordinates

The position of the atoms in the primitive cell are defined by the atomic coordinates given by the matrix $\mathbf{r_p}$:

$$\mathbf{r_p} = \begin{bmatrix} x_1 & x_2 & \cdots & x_i \\ y_1 & y_2 & \cdots & y_i \\ z_1 & z_2 & \cdots & z_i \end{bmatrix}$$

where i is equal to the number of atoms per cell.

When the cell is redefined, the atomic coordinates are also redefined. The atomic coordinates in the redefined cell can be represented by a matrix $\mathbf{r_r}$:

$$\mathbf{r_r} = \begin{bmatrix} x'_1 & x'_2 & \cdots & x'_i \\ y'_1 & y'_2 & \cdots & y'_i \\ z'_1 & z'_2 & \cdots & z'_i \end{bmatrix}$$

It is useful to define a new set of coordinates, labelled with the **c** subscript. These coordinates are referred to the redefine cell before rotation of the frame in order to place the specified plane in the xy plane; that is the cell called **C** in A.1. The transformation between Cartesian and fractional coordinates in the redefined (but not rotated cell) is the same used in Section A.2 and A.3

$$\mathbf{r_c} = \mathbf{C}^{\mathrm{T}}\,\mathbf{f_c} \tag{A.5}$$

and

$$\mathbf{f_c} = (\mathbf{C}^{\mathrm{T}})^{-1}\,\mathbf{r_c} \tag{A.6}$$

$\mathbf{r_c}$ is equal to $\mathbf{r_p}$ since the atomic positions are not changed by the redefinition of the cell (before the rotation); $\mathbf{f_c}$ is equal to $\mathbf{f_r}$ since the fractional coordinates are referred to the cell independently of its orientation. Therefore, Equation A.6 can be written as:

$$\mathbf{f_r} = (\mathbf{C}^{\mathrm{T}})^{-1}\,\mathbf{r_p} \tag{A.7}$$

This link between coordinates in the primitive and redefined cells allows for the derivation of all possible relations between coordinates. It is possible to calculate the fractional coordinates in the redefined cell in terms of the fractional coordinates in the primitive cell;

$$\begin{aligned}
\mathbf{f_r} &= (\mathbf{C}^{\mathrm{T}})^{-1}\mathbf{r_p} && \text{(A.8)}\\
&= (\mathbf{C}^{\mathrm{T}})^{-1}\mathbf{A}^{\mathrm{T}}\,\mathbf{f_p} && \text{(A.9)}\\
&= (\mathbf{P}\mathbf{A}^{\mathrm{T}})^{-1}\mathbf{A}^{\mathrm{T}}\,\mathbf{f_p} && \text{(A.10)}\\
&= (\mathbf{A}^{\mathrm{T}}\mathbf{P}^{\mathrm{T}})^{-1}\mathbf{A}^{\mathrm{T}}\,\mathbf{f_p} && \text{(A.11)}\\
&= (\mathbf{P}^{\mathrm{T}})^{-1}\,(\mathbf{A}^{\mathrm{T}})^{-1}\mathbf{A}^{\mathrm{T}}\,\mathbf{f_p} && \text{(A.12)}\\
&= (\mathbf{P}^{\mathrm{T}})^{-1}\,\mathbf{f_p} && \text{(A.13)}
\end{aligned}$$

the Cartesian coordinates in the redefined cell in terms of the fractional coordinates in the primitive cell

$$\begin{aligned}
\mathbf{r_r} &= \mathbf{B}^{\mathrm{T}}\,\mathbf{f_r} && \text{(A.14)}\\
&= \mathbf{B}^{\mathrm{T}}\,(\mathbf{P}^{\mathrm{T}})^{-1}\,\mathbf{f_p} && \text{(A.15)}
\end{aligned}$$

and finally, the Cartesian coordinates in the redefined cell in terms of the Cartesian coordinates in the primitive cell

$$\begin{aligned}
\mathbf{r_r} &= \mathbf{B}^{\mathrm{T}}\,\mathbf{f_r} && \text{(A.16)}\\
&= \mathbf{B}^{\mathrm{T}}\,(\mathbf{P}^{\mathrm{T}})^{-1}\,\mathbf{f_p} && \text{(A.17)}\\
&= \mathbf{B}^{\mathrm{T}}\,(\mathbf{P}^{\mathrm{T}})^{-1}\,(\mathbf{A}^{\mathrm{T}})^{-1}\,\mathbf{r_p} && \text{(A.18)}\\
&= \mathbf{B}^{\mathrm{T}}\,\mathbf{F}^{\mathrm{T}}\,(\mathbf{R}^{\mathrm{T}})^{-1}\,\mathbf{R}^{\mathrm{T}}\,(\mathbf{B}^{\mathrm{T}})^{-1}\,\mathbf{r_p} && \text{(A.19)}\\
&= \mathbf{B}^{\mathrm{T}}\,\mathbf{F}^{\mathrm{T}}\,(\mathbf{B}^{\mathrm{T}})^{-1}\,\mathbf{r_p} && \text{(A.20)}\\
&= (\mathbf{FB})^{\mathrm{T}}\,(\mathbf{B}^{\mathrm{T}})^{-1}\,\mathbf{r_p} && \text{(A.21)}\\
&= (\mathbf{B}^{-1}\mathbf{FB})^{\mathrm{T}}\,\mathbf{r_p} && \text{(A.22)}\\
&= \mathbf{T}\,\mathbf{r_p} && \text{(A.23)}
\end{aligned}$$

In order to define the atomic coordinates in the redefined cell, the transformation matrix $\mathbf{T}$ is applied to the atomic coordinates in the original primitive cell.

$$\mathbf{r_r} = \mathbf{T}\ \mathbf{r_p}$$

$$\begin{bmatrix} x'_1 & x'_2 & \cdots & x'_i \\ y'_1 & y'_2 & \cdots & y'_i \\ z'_1 & z'_2 & \cdots & z'_i \end{bmatrix} = \begin{bmatrix} t_{11} & t_{12} & t_{13} \\ t_{21} & t_{22} & t_{23} \\ t_{31} & t_{32} & t_{33} \end{bmatrix} \begin{bmatrix} x_1 & x_2 & \cdots & x_i \\ y_1 & y_2 & \cdots & y_i \\ z_1 & z_2 & \cdots & z_i \end{bmatrix}$$

In summary, the coordinates in the redefined cell are related to the coordinates in the primitive cell by the following equations:

$$\begin{aligned}
\mathbf{f_r} &= (\mathbf{P}^{\mathrm{T}})^{-1}\ \times\ \mathbf{f_p} && \text{(A.24)}\\
\mathbf{f_r} &= (\mathbf{C}^{\mathrm{T}})^{-1}\,\mathbf{r_p} && \text{(A.25)}\\
\mathbf{r_r} &= \mathbf{B}^{\mathrm{T}}\ \times\ (\mathbf{P}^{\mathrm{T}})^{-1}\ \times\ \mathbf{f_p} && \text{(A.26)}\\
\mathbf{r_r} &= \mathbf{T}\ \times\ \mathbf{r_p} && \text{(A.27)}
\end{aligned}$$

The coordinates may differ from the ones calculated with CRYSTAL because of the constrain of atoms being within the -0.5 and 0.5 fractional coordinates. This may displace atoms from one cell to another. Therefore, even if the atom is always in the same position its coordinates can change of an integer number of lattice parameters.

A.5 Reciprocal Space

The same derivation can be applied to the reciprocal space lattice vectors and points. The reciprocal lattice cell, corresponding to the primitive cell **A** in the direct space, is defined by the lattice vectors $\mathbf{a}^*$, $\mathbf{b}^*$ and $\mathbf{c}^*$. The reciprocal-lattice vectors can be represented by a matrix $\mathbf{A}^*$:

$$\mathbf{A}^* = \begin{bmatrix} A1_x^* & A1_y^* & A1_z^* \\ A2_x^* & A2_y^* & A2_z^* \\ A3_x^* & A3_y^* & A3_z^* \end{bmatrix}$$

When the direct-lattice cell is redefined, also the reciprocal lattice is changed. The redefined reciprocal-lattice cell $\mathbf{B}^*$ is derived from the primitive one by applying the $\mathbf{R}^*$ matrix to $\mathbf{A}^*$:

$$\mathbf{B}^* = \mathbf{R}^*\mathbf{A}^*$$

$$\begin{bmatrix} B1_x^* & B1_y^* & B1_z^* \\ B2_x^* & B2_y^* & B2_z^* \\ B3_x^* & B3_y^* & B3_z^* \end{bmatrix} = \begin{bmatrix} r_{11}^* & r_{12}^* & r_{13}^* \\ r_{21}^* & r_{22}^* & r_{23}^* \\ r_{31}^* & r_{32}^* & r_{33}^* \end{bmatrix} \begin{bmatrix} A1_x^* & A1_y^* & A1_z^* \\ A2_x^* & A2_y^* & A2_z^* \\ A3_x^* & A3_y^* & A3_z^* \end{bmatrix}$$

The $\mathbf{R}^*$ matrix is the transposed inverse of the **R** matrix:

$$\mathbf{R}^* = (\mathbf{R}^{\mathrm{T}})^{-1} \tag{A.28}$$

In the same way it is useful to define $\mathbf{F}^*$ and $\mathbf{P}^*$ as:

$$\mathbf{F}^* = (\mathbf{F}^{\mathrm{T}})^{-1} \tag{A.29}$$

$$\mathbf{P}^* = (\mathbf{P}^{\mathrm{T}})^{-1} \tag{A.30}$$

In summary,

$$\mathbf{R}^* = (\mathbf{R}^{\mathrm{T}})^{-1} = \mathbf{F}^* \times \mathbf{P}^* = (\mathbf{F}^{\mathrm{T}})^{-1} \times (\mathbf{P}^{\mathrm{T}})^{-1} \tag{A.31}$$

As for the direct space coordinates, it is possible to transform the Cartesian coordinates to fractional coordinates and vice versa by using:

$$\mathbf{r}_{\mathbf{p}}^* = \mathbf{A}^{*\mathrm{T}}\, \mathbf{f}_{\mathbf{p}}^* \tag{A.32}$$

$$\mathbf{f}_{\mathbf{p}}^* = (\mathbf{A}^{*\mathrm{T}})^{-1}\, \mathbf{r}_{\mathbf{p}}^* \tag{A.33}$$

In the redefined cell, the $\mathbf{B}^*$ matrix must be used:

$$\mathbf{r}_{\mathbf{r}}^* = \mathbf{B}^{*\mathrm{T}}\, \mathbf{f}_{\mathbf{r}}^* \tag{A.34}$$

$$\mathbf{f}_{\mathbf{r}}^* = (\mathbf{B}^{*\mathrm{T}})^{-1}\, \mathbf{r}_{\mathbf{r}}^* \tag{A.35}$$

The relationship between coordinates in the primitive and redefined cell can be derived as in A.4, where the vectors and matrices referred to the direct lattice must be replaced by the corresponding one in the reciprocal space, as indicated previously in this paragraph. The final relations are here reported without the complete derivation:

$$\mathbf{f}^*_\mathbf{r} = (\mathbf{P}^{*\mathrm{T}})^{-1}\, \mathbf{f}^*_\mathbf{p} = \mathbf{P}\, \mathbf{f}^*_\mathbf{p} \tag{A.36}$$

$$\mathbf{f}^*_\mathbf{r} = (\mathbf{C}^{*\mathrm{T}})^{-1}\, \mathbf{r}^*_\mathbf{p} = \mathbf{C}\, \mathbf{r}^*_\mathbf{p} \tag{A.37}$$

$$\mathbf{r}^*_\mathbf{r} = \mathbf{B}^{*\mathrm{T}}\, (\mathbf{P}^{*\mathrm{T}})^{-1}\, \mathbf{f}^*_\mathbf{p} = \mathbf{B}^{*\mathrm{T}}\, \mathbf{P}\, \mathbf{f}^*_\mathbf{p} \tag{A.38}$$

$$\mathbf{r}^*_\mathbf{r} = \mathbf{T}^*\, \mathbf{r}^*_\mathbf{p} \tag{A.39}$$

A.5.1 Differences Between Slab and Bulk Redefined Reciprocal Lattice Cells

Before discussing how the band structure of a surface can be compared to a bulk projected one, a short summary of the key transformation between direct and reciprocal space is reported. The reciprocal lattice vectors $\mathbf{a}^*$,$\mathbf{b}^*$ and $\mathbf{c}^*$ can be built from the direct space cell according to

$$\mathbf{a}^* = \frac{2\pi}{V}\mathbf{b} \wedge \mathbf{c} \tag{A.40}$$

$$\mathbf{b}^* = \frac{2\pi}{V}\mathbf{a} \wedge \mathbf{c} \tag{A.41}$$

$$\mathbf{c}^* = \frac{2\pi}{V}\mathbf{a} \wedge \mathbf{b} \tag{A.42}$$

where the volume is

$$V = \mathbf{c} \cdot \mathbf{a} \wedge \mathbf{b} = c_x(a_y b_z - a_z b_y) - c_y(a_x b_z - a_z b_x) + c_z(a_x b_y - a_y b_x) \tag{A.43}$$

For the following discussion it is useful to define the expansion of the vectorial product:

$$\mathbf{a}^* = \frac{2\pi}{V}\begin{vmatrix} \hat{\mathbf{u}}_x & \hat{\mathbf{u}}_y & \hat{\mathbf{u}}_z \\ b_x & b_y & b_z \\ c_x & c_y & c_z \end{vmatrix} = \frac{2\pi}{V}[(b_y c_z - b_z c_y)\hat{\mathbf{u}}_x - (b_x c_z - b_z c_x)\hat{\mathbf{u}}_y + (b_x c_y - b_y c_x)\hat{\mathbf{u}}_z] \quad (A.44)$$

$$\mathbf{b}^* = \frac{2\pi}{V}\begin{vmatrix} \hat{\mathbf{u}}_x & \hat{\mathbf{u}}_y & \hat{\mathbf{u}}_z \\ a_x & a_y & a_z \\ c_x & c_y & c_z \end{vmatrix} = \frac{2\pi}{V}[(a_y c_z - a_z c_y)\hat{\mathbf{u}}_x - (a_x c_z - a_z c_x)\hat{\mathbf{u}}_y + (a_x c_y - a_y c_x)\hat{\mathbf{u}}_z] \quad (A.45)$$

$$\mathbf{c}^* = \frac{2\pi}{V}\begin{vmatrix} \hat{\mathbf{u}}_x & \hat{\mathbf{u}}_y & \hat{\mathbf{u}}_z \\ a_x & a_y & a_z \\ b_x & b_y & b_z \end{vmatrix} = \frac{2\pi}{V}[(a_y b_z - a_z b_y)\hat{\mathbf{u}}_x - (a_x b_z - a_z b_x)\hat{\mathbf{u}}_y + (a_x b_y - a_y b_x)\hat{\mathbf{u}}_z] \quad (A.46)$$

When the bulk cell is redefined and rotated in order to have the **a** and **b** vectors in the xy plane, the $\mathbf{a}^*$ and $\mathbf{b}^*$ vectors of the reciprocal lattice may not be in the x^*y^* plane. [1]

Three types of cells are discussed: the bulk primitive (**A**), the bulk redefined (**B**) and the slab (**S**) cells. The bulk redefined cell is the one where the direct lattice vectors are defined in order to have the **a** and **b** vectors in the xy plane. The slab cell is built directly from the bulk redefined cell by removing the periodicity along the z direction; the **c** vector is, therefore, transformed in the unit vector along the $\hat{\mathbf{u}}_z$ direction, as given below. The reciprocal lattices of the three types of cells are also reported. Their derivation is discussed in the following.

---

[1] The vectorial product defines a new vector that is orthogonal to two other vectors (**r** and **s**). The resultant vector $\mathbf{v} = (v_x\hat{\mathbf{u}}_x + v_y\hat{\mathbf{u}}_y + v_z\hat{\mathbf{u}}_z)$ is calculated as

$$\mathbf{v} = \mathbf{r} \wedge \mathbf{s} = \begin{vmatrix} \hat{\mathbf{u}}_x & \hat{\mathbf{u}}_y & \hat{\mathbf{u}}_z \\ r_x & r_y & r_z \\ s_x & s_y & s_z \end{vmatrix} = (r_y s_z - r_z s_y)\hat{\mathbf{u}}_x - (r_x s_z - r_z s_x)\hat{\mathbf{u}}_y + (r_x s_y - r_y s_x)\hat{\mathbf{u}}_z$$

This is a general relationship and when applied to Eq. A.44, A.45 and A.46 it is clear that the unit vectors in the direct space coincide with the ones in the reciprocal space. The axis frame xyz coincide, therefore, with $x^*y^*z^*$.

$$\mathbf{A} = \begin{bmatrix} a_x & a_y & a_z \\ b_x & b_y & b_z \\ c_x & c_y & c_z \end{bmatrix} \qquad \mathbf{A}^* = \begin{bmatrix} a_x^* & a_y^* & a_z^* \\ b_x^* & b_y^* & b_z^* \\ c_x^* & c_y^* & c_z^* \end{bmatrix} \tag{A.47}$$

$$\mathbf{B} = \begin{bmatrix} a'_x & a'_y & 0 \\ b'_x & b'_y & 0 \\ c'_x & c'_y & c'_z \end{bmatrix} \qquad \mathbf{B}^* = \begin{bmatrix} a'^*_x & a'^*_y & a'^*_z \\ b'^*_x & b'^*_y & b'^*_z \\ 0 & 0 & c'^*_z \end{bmatrix} \tag{A.48}$$

$$\mathbf{S} = \begin{bmatrix} a'_x & a'_y & 0 \\ b'_x & b'_y & 0 \\ 0 & 0 & 1 \end{bmatrix} \qquad \mathbf{S}^* = \begin{bmatrix} a'^*_x & a'^*_y & 0 \\ b'^*_x & b'^*_y & 0 \\ 0 & 0 & 2\pi \end{bmatrix} \tag{A.49}$$

Since in the matrices representing **B** and **S** cells some of the elements are zeros, the construction of their reciprocal lattices will be simplified.

- **Bulk primitive**: this is the general case, all the components in equations from A.44 to A.46 can be different from zero. Therefore $\mathbf{a}^*$, $\mathbf{b}^*$ and $\mathbf{c}^*$ can have components along the three $\hat{\mathbf{u}}_x$, $\hat{\mathbf{u}}_y$ and $\hat{\mathbf{u}}_z$ directions.

- **Bulk redefined** [2]:

$$\mathbf{a}'^* = \frac{2\pi}{V} \begin{vmatrix} \hat{\mathbf{u}}_x & \hat{\mathbf{u}}_y & \hat{\mathbf{u}}_z \\ b'_x & b'_y & 0 \\ c'_x & c'_y & c'_z \end{vmatrix} = \frac{2\pi}{V}[(b'_y c'_z)\hat{\mathbf{u}}_x - (b'_x c'_z)\hat{\mathbf{u}}_y + (b'_x c'_y - b'_y c'_x)\hat{\mathbf{u}}_z] \tag{A.50}$$

$$= 2\pi \left[\frac{b'_y c'_z}{c'_z(a'_x b'_y - a'_y b'_x)} \hat{\mathbf{u}}_x - \frac{b'_x c'_z}{c'_z(a'_x b'_y - a'_y b'_x)} \hat{\mathbf{u}}_y + \frac{b'_x c'_y - b'_y c'_x}{c'_z(a'_x b'_y - a'_y b'_x)} \hat{\mathbf{u}}_z \right] \tag{A.51}$$

---

[2] It is important to notice that the volume of the redefined cell is

$$V = c'_z(a'_x b'_y - a'_y b'_x)$$

since the a_z and b_z in Eq. A.43 are equal to 0.

$$= 2\pi \left[\frac{b'_y}{a'_x b'_y - a'_y b'_x} \hat{\mathbf{u}}_x - \frac{b'_x}{a'_x b'_y - a'_y b'_x} \hat{\mathbf{u}}_y + \frac{b'_x c'_y - b'_y c'_x}{c'_z (a'_x b'_y - a'_y b'_x)} \hat{\mathbf{u}}_z \right] \tag{A.52}$$

$$\mathbf{b}'^{*} = \frac{2\pi}{V} \begin{vmatrix} \hat{\mathbf{u}}_x & \hat{\mathbf{u}}_y & \hat{\mathbf{u}}_z \\ a'_x & a'_y & 0 \\ c'_x & c'_y & c'_z \end{vmatrix} = \frac{2\pi}{V} [(a'_y c'_z) \hat{\mathbf{u}}_x - (a'_x c'_z) \hat{\mathbf{u}}_y + (a'_x c'_y - a'_y c'_x) \hat{\mathbf{u}}_z] \tag{A.53}$$

$$= 2\pi \left[\frac{a'_y c'_z}{c'_z (a'_x b'_y - a'_y b'_x)} \hat{\mathbf{u}}_x - \frac{a'_x c'_z}{c'_z (a'_x b'_y - a'_y b'_x)} \hat{\mathbf{u}}_y + \frac{a'_x c'_y - a'_y c'_x}{c'_z (a'_x b'_y - a'_y b'_x)} \hat{\mathbf{u}}_z \right] \tag{A.54}$$

$$= 2\pi \left[\frac{a'_y}{a'_x b'_y - a'_y b'_x} \hat{\mathbf{u}}_x - \frac{a'_x}{a'_x b'_y - a'_y b'_x} \hat{\mathbf{u}}_y + \frac{a'_x c'_y - a'_y c'_x}{c'_z (a'_x b'_y - a'_y b'_x)} \hat{\mathbf{u}}_z \right] \tag{A.55}$$

$$\mathbf{c}'^{*} = \frac{2\pi}{V} \begin{vmatrix} \hat{\mathbf{u}}_x & \hat{\mathbf{u}}_y & \hat{\mathbf{u}}_z \\ a'_x & a'_y & 0 \\ b'_x & b'_y & 0 \end{vmatrix} = \frac{2\pi}{V} [(a'_x b'_y - a'_y b'_x) \hat{\mathbf{u}}_z] \tag{A.56}$$

$$= 2\pi \left[\frac{a'_x b'_y - a'_y b'_x}{c'_z (a'_x b'_y - a'_y b'_x)} \hat{\mathbf{u}}_z \right] \tag{A.57}$$

The $\mathbf{c}'^{*}$ vector is directed along the $\hat{\mathbf{u}}_z$ direction. This is intuitive since the $\mathbf{a}'$ and $\mathbf{b}'$ vectors are in the xy plane and the $\mathbf{c}'^{*}$ is orthogonal to them by definition. Interestingly, the $\mathbf{a}'^{*}$ and $\mathbf{b}'^{*}$ may not be in the $x^{*}y^{*}$ plane, due to the non-zero component along $\hat{\mathbf{u}}_z$; this point is particularly useful when calculating the projected band structure.

- **Slab cell** [3]:

---

[3] The volume of the slab cell is

$$V = a'_x b'_y - a'_y b'_x$$

since the a_z and b_z in Eq. A.43 are equal to 0 and c_z is the unit vector along the $\hat{\mathbf{u}}_z$ direction.

$$\mathbf{a}'^{*} = \frac{2\pi}{V}\begin{vmatrix} \hat{\mathbf{u}}_x & \hat{\mathbf{u}}_y & \hat{\mathbf{u}}_z \\ b'_x & b'_y & 0 \\ 0 & 0 & 1 \end{vmatrix} = \frac{2\pi}{V}[(b'_y \cdot 1)\hat{\mathbf{u}}_x - (b'_x \cdot 1)\hat{\mathbf{u}}_y] \tag{A.58}$$

$$= 2\pi\left[\frac{b'_y}{a'_x b'_y - a'_y b'_x}\hat{\mathbf{u}}_x - \frac{b'_x}{a'_x b'_y - a'_y b'_x}\hat{\mathbf{u}}_y\right] \tag{A.59}$$

$$\mathbf{b}'^{*} = \frac{2\pi}{V}\begin{vmatrix} \hat{\mathbf{u}}_x & \hat{\mathbf{u}}_y & \hat{\mathbf{u}}_z \\ a'_x & a'_y & 0 \\ 0 & 0 & 1 \end{vmatrix} = \frac{2\pi}{V}[(a'_y \cdot 1)\hat{\mathbf{u}}_x - (a'_x \cdot 1)\hat{\mathbf{u}}_y] \tag{A.60}$$

$$= 2\pi\left[\frac{a'_y}{a'_x b'_y - a'_y b'_x}\hat{\mathbf{u}}_x - \frac{a'_x}{a'_x b'_y - a'_y b'_x}\hat{\mathbf{u}}_y\right] \tag{A.61}$$

$$\mathbf{c}'^{*} = \frac{2\pi}{V}\begin{vmatrix} \hat{\mathbf{u}}_x & \hat{\mathbf{u}}_y & \hat{\mathbf{u}}_z \\ a'_x & a'_y & 0 \\ b'_x & b'_y & 0 \end{vmatrix} = \frac{2\pi}{V}[(a'_x b'_y - a'_y b'_x)\hat{\mathbf{u}}_z] \tag{A.62}$$

$$= 2\pi\left[\frac{a'_x b'_y - a'_y b'_x}{a'_x b'_y - a'_y b'_x}\hat{\mathbf{u}}_z\right] = 2\pi\hat{\mathbf{u}}_z \tag{A.63}$$

It can be seen, in Eq. from A.50 to A.63, that the $\mathbf{a}'^{*}$ and $\mathbf{b}'^{*}$ components along the $\hat{\mathbf{u}}_x$ and $\hat{\mathbf{u}}_y$ are the same in the $\mathbf{B}^{*}$ and $\mathbf{S}^{*}$ cells. In the $\mathbf{B}^{*}$ cell, the $\mathbf{c}'$ vector enters in the definition of the $\mathbf{a}'^{*}$ and $\mathbf{b}'^{*}$ vectors. However, in the $\hat{\mathbf{u}}_x$ and $\hat{\mathbf{u}}_y$ directions its contribution is canceled out by the volume acting as normalization factor. In the $\mathbf{S}^{*}$ cell the $\mathbf{c}'$ is the unit vector in the $\hat{\mathbf{u}}_z$ direction. This means that the $\mathbf{a}'^{*}$ and $\mathbf{b}^{*}$ vectors do not contain any $\mathbf{c}'$ components. But at the same time the volume of the slab cell does not contain $\mathbf{c}'$ contributions. It is important to notice that even if the length of the vectors may be different, the a'^{*}_x a'^{*}_y b'^{*}_x and b'^{*}_y are the same in the slab cell and in the bulk redefined.

In summary, the main point is that a **k** point expressed as fractional coordinates of the $\mathbf{B}^*$ cell has, in general, different fractional coordinates if expressed as fractions of the $\mathbf{S}^*$ cell, due to the differences in the cell vectors of the $\mathbf{B}^*$ and $\mathbf{S}^*$ cells. This is relevant when comparing band structures of bulk and surfaces. In the next section a method to perform such transformation is provided.

Calculation of the Surface Projected Band Structure

The method to transform a **k** point path expressed as fractional coordinates of the $\mathbf{S}^*$ cell to a path expressed as fractional coordinates of the $\mathbf{A}^*$ cell will be discussed below. This is of particular interest when calculating the surface projected band structure, where the same **k** points in the surface and in the bulk cells must be used. The procedure is reported here:

- Select a 2D **k** point path in the reciprocal space, using the fractional coordinates of the surface Brillouin zone (which is bidimensional by definition)

$$\mathbf{f}^*_{\mathbf{S}} = \begin{bmatrix} f^*_a \\ f^*_b \\ 0 \end{bmatrix} \tag{A.64}$$

- Find the absolute coordinates of the selected points by using:

$$\mathbf{r}^*_{\mathbf{S}} = (\mathbf{S}^*)^{\mathbf{T}} \mathbf{f}^*_{\mathbf{S}} \tag{A.65}$$

$$= \begin{bmatrix} a'^*_x & b'^*_x & 0 \\ a'^*_y & b'^*_y & 0 \\ 0 & 0 & 2\pi \end{bmatrix} \begin{bmatrix} f^*_a \\ f^*_b \\ 0 \end{bmatrix} \tag{A.66}$$

$$= \begin{bmatrix} (a'^*_x f^*_a) + (b'^*_x f^*_b) \\ (a'^*_y f^*_a) + (b'^*_y) f^*_b) \\ 0 \end{bmatrix} = \begin{bmatrix} r^*_x \\ r^*_y \\ 0 \end{bmatrix} \tag{A.67}$$

As expected, in the slab, the **k** points corresponding to a path where $f_c = 0$ are in the x^*y^* plane.

It is possible to demonstrate [4] that the reciprocal lattice in the x^*y^* plane is the same in the slab and bulk redefined cells. The link between the slab and bulk redefined cell is, therefore, in these Cartesian coordinates of the **k** points.

$$\mathbf{r}^*_{\mathbf{B}} = \mathbf{r}^*_{\mathbf{S}} \tag{A.68}$$

- The Cartesian coordinates can be expressed as fractional coordinates of the redefined reciprocal bulk cell, $\mathbf{B}^*$ by using

---

[4] The direct space lattice can be represented as the product of three Dirac delta functions :

$$f(\mathbf{r}) = f(\mathbf{x},\mathbf{y},\mathbf{z}) = \sum_{t=-\infty}^{\infty} \delta(\mathbf{r}-\mathbf{r_t}) = \sum_{\mathbf{m}=-\infty}^{\infty}\sum_{\mathbf{n}=-\infty}^{\infty}\sum_{\mathbf{p}=-\infty}^{\infty} \delta(\mathbf{r}-\mathbf{ma})\delta(\mathbf{r}-\mathbf{nb})\delta(\mathbf{r}-\mathbf{pc})$$

The reciprocal lattice can be obtained through a Fourier transform of the direct lattice. For an infinite model it results in:

$$T[f(\mathbf{r})] = f(\mathbf{r}^*) = f(\mathbf{x}^*,\mathbf{y}^*,\mathbf{z}^*) = \frac{1}{\mathbf{a}\wedge\mathbf{b}\cdot\mathbf{c}}\sum_{h=-\infty}^{\infty}\sum_{k=-\infty}^{\infty}\sum_{l=-\infty}^{\infty} \delta(a\mathbf{r}^*-h)\delta(b\mathbf{r}^*-k)\delta(c\mathbf{r}^*-l)$$

A bidimensional lattice can be expressed as

$$f(\mathbf{r}) = f(\mathbf{x},\mathbf{y}) = \sum_{t=-\infty}^{\infty} \delta(\mathbf{r}-\mathbf{r_t}) = \sum_{\mathbf{m}=-\infty}^{\infty}\sum_{\mathbf{n}=-\infty}^{\infty} \delta(\mathbf{r}-\mathbf{ma})\delta(\mathbf{r}-\mathbf{nb})\delta(\mathbf{r})$$

and its reciprocal lattice, derived as above, is:

$$f(\mathbf{r}^*) = f(\mathbf{x}^*,\mathbf{y}^*) = \frac{1}{\mathbf{a}\wedge\mathbf{b}}\sum_{h=-\infty}^{\infty}\sum_{k=-\infty}^{\infty} \delta(a\mathbf{r}^*-h)\delta(b\mathbf{r}^*-k)$$

From the last equation, it is clear that as long as the **a** and **b** vectors are the same, the reciprocal lattice is unchanged in the x^*y^* plane. This is the case of the bulk redefined and slab cells, where the only difference is in the **c** vector.

$$\mathbf{f}^*_{\mathbf{B}} = [(\mathbf{B}^*)^{\mathbf{T}}]^{-\mathbf{1}}\mathbf{r}^*_{\mathbf{B}} \tag{A.69}$$

$[(\mathbf{B}^*)^{\mathbf{T}}]^{-\mathbf{1}}$ can be easily calculated:

$$[(\mathbf{B}^*)^{\mathbf{T}}]^{-\mathbf{1}} = \left(\begin{bmatrix} a'^*_x & a'^*_y & a'^*_z \\ b'^*_x & b'^*_y & b'^*_z \\ 0 & 0 & c'^*_z \end{bmatrix}^T\right)^{-1} = \begin{bmatrix} a'^*_x & b'^*_x & 0 \\ a'^*_y & b'^*_y & 0 \\ a'^*_z & b'^*_z & c'^*_z \end{bmatrix}^{-1} \tag{A.70}$$

$$= \frac{1}{c'^*_z(a'^*_x b'^*_y - a'^*_y b'^*_x)} \begin{bmatrix} b'^*_y c'^*_z & -a'^*_y c'^*_z & a'^*_y b'^*_z - a'^*_z b'^*_y \\ -b'^*_x c'^*_z & a'^*_x c'^*_z & -(a'^*_x b'^*_z - a'^*_z b'^*_x) \\ 0 & 0 & a'^*_x b'^*_y - a'^*_y b'^*_x \end{bmatrix} \tag{A.71}$$

$$= \frac{1}{V^*_B} \begin{bmatrix} b'^*_y c'^*_z & -a'^*_y c'^*_z & a'^*_y b'^*_z - a'^*_z b'^*_y \\ -b'^*_x c'^*_z & a'^*_x c'^*_z & -(a'^*_x b'^*_z - a'^*_z b'^*_x) \\ 0 & 0 & a'^*_x b'^*_y - a'^*_y b'^*_x \end{bmatrix} \tag{A.72}$$

$$= \frac{1}{2\pi} \begin{bmatrix} a'_x & a'_y & 0 \\ -b'_x & b'_y & 0 \\ c'_x & c'_y & c'_z \end{bmatrix} \tag{A.73}$$

In the same way the $[(\mathbf{S}^*)^{\mathbf{T}}]^{-\mathbf{1}}$ matrix can be calculated:

$$[(\mathbf{S}^*)^{\mathbf{T}}]^{-\mathbf{1}} = \left(\begin{bmatrix} a'^*_x & a'^*_y & 0 \\ b'^*_x & b'^*_y & 0 \\ 0 & 0 & 2\pi \end{bmatrix}^T\right)^{-1} = \begin{bmatrix} a'^*_x & b'^*_x & 0 \\ a'^*_y & b'^*_y & 0 \\ 0 & 0 & 2\pi \end{bmatrix}^{-1} \tag{A.74}$$

$$= \frac{1}{2\pi(a'^*_x b'^*_y - a'^*_y b'^*_x)} \begin{bmatrix} 2\pi b'^*_y & -2\pi b'^*_x & 0 \\ -2\pi a'^*_y & 2\pi a'^*_x & 0 \\ 0 & 0 & a'^*_x b'^*_y - a'^*_y b'^*_x \end{bmatrix} \tag{A.75}$$

$$= \frac{1}{V_S^*}\begin{bmatrix} 2\pi b_y'^* & -2\pi b_x'^* & 0 \\ -2\pi a_y'^* & 2\pi a_x'^* & 0 \\ 0 & 0 & a_x'^* b_y'^* - a_y'^* b_x'^* \end{bmatrix} \tag{A.76}$$

$$= \frac{1}{2\pi}\begin{bmatrix} a_x' & a_y' & 0 \\ -b_x' & b_y' & 0 \\ 0 & 0 & c_z' \end{bmatrix} \tag{A.77}$$

It is important to notice that the only difference between $[(\mathbf{B}^*)^{\mathbf{T}}]^{-\mathbf{1}}$ and $[(\mathbf{S}^*)^{\mathbf{T}}]^{-\mathbf{1}}$ is in the c_x' and c_y' components. As a consequence, when the Cartesian coordinates of a point which lies on the x^*y^* plane are transformed in fractional coordinates of the two cell, the f_a^* and f_b^* values will be the same. The difference is in the f_c^* component that is 0 in the slab cell and may be different from 0 in the bulk redefined cell, depending on the orientation of the $\mathbf{c}'^*$ vector.

$$\mathbf{f}_{\mathbf{B}}^* = \frac{1}{2\pi}\begin{bmatrix} a_x' & a_y' & 0 \\ -b_x' & -b_y' & 0 \\ c_x & c_y & c_z \end{bmatrix}\begin{bmatrix} r_x^* \\ r_y^* \\ 0 \end{bmatrix}\begin{bmatrix} (a_x' r_x^*) + (a_y' r_y^*) \\ (-b_x' r_x^*) + (-b_y' r_y^*) \\ (c_x r_x^*) + (c_y r_y^*) \end{bmatrix} \tag{A.78}$$

$$\mathbf{f}_{\mathbf{S}}^* = \frac{1}{2\pi}\begin{bmatrix} a_x' & a_y' & 0 \\ -b_x' & -b_y' & 0 \\ 0 & 0 & c_z' \end{bmatrix}\begin{bmatrix} r_x^* \\ r_y^* \\ 0 \end{bmatrix}\begin{bmatrix} (a_x' r_x^*) + (a_y' r_y^*) \\ (-b_x' r_x^*) + (-b_y' r_y^*) \\ 0 \end{bmatrix} \tag{A.79}$$

- The bulk cell must me sampled along the z^* axis and not along $\mathbf{c}'^*$. This is because as the number of layers along $\mathbf{c}'$ in the slab cell increases the effect on the reciprocal space is a higher number of sampled points along the $\mathbf{c}'^*$ direction, that is along the z^* axis (see Eq. A.63). The z^* direction must be sampled in a range of Cartesian coordinates corresponding to $|\mathbf{c}'^*|$. This corresponds to a variation of 1 in terms of f_z^* of the redefined k points.

- Transform the fractional coordinates of the redefined cell in the primitive cell ones, $\mathbf{A}^*$, (by using Eq. A.36)

Cu (110) surface

The Cu (110) surface is now used as example of the discussion above.

$$\mathbf{A} = \begin{bmatrix} 0.0000 & 1.8149 & 1.8149 \\ 1.8149 & 0.0000 & 1.8149 \\ 1.8149 & 1.8149 & 0.0000 \end{bmatrix} \mathbf{A}^* = \begin{bmatrix} -1.7309 & 1.7309 & 1.7309 \\ 1.7309 & -1.7309 & 1.7309 \\ 1.7309 & 1.7309 & -1.7309 \end{bmatrix} \tag{A.80}$$

$$\mathbf{B} = \begin{bmatrix} 2.5668 & 0.0000 & 0.0000 \\ 0.0000 & 3.6300 & 0.0000 \\ 1.2834 & 1.8150 & 1.2834 \end{bmatrix} \mathbf{B}^* = \begin{bmatrix} 2.4478 & 0.0000 & -2.4478 \\ 0.0000 & 1.7309 & -2.4478 \\ 0.0000 & 0.0000 & 4.8957 \end{bmatrix} \tag{A.81}$$

$$\mathbf{S} = \begin{bmatrix} 2.5667 & 0.0000 & 0.0000 \\ 0.0000 & 3.6299 & 0.0000 \\ 0.0000 & 0.0000 & 1.0000 \end{bmatrix} \mathbf{S}^* = \begin{bmatrix} 2.4478 & 0.0000 & 0.0000 \\ 0.0000 & 1.7309 & 0.0000 \\ 0.0000 & 0.0000 & 6.2832 \end{bmatrix} \tag{A.82}$$

The surface high symmetry points are included in the following path:

$$\mathbf{f}^*_{\mathbf{S}} = \begin{bmatrix} 0.00000 & 0.50000 & 0.50000 & 0.00000 & 0.00000 & 0.50000 \\ 0.00000 & 0.00000 & 0.50000 & 0.50000 & 0.00000 & 0.50000 \\ 0.00000 & 0.00000 & 0.00000 & 0.00000 & 0.00000 & 0.00000 \end{bmatrix}$$

They are transformed in absolute coordinates by using:

$$\mathbf{r}^*_{\mathbf{S}} = \mathbf{S}^{*\mathrm{T}}\, \mathbf{f}^*_{\mathbf{S}} \tag{A.83}$$

Resulting in:

$$\mathbf{r}^*_{\mathbf{S}} = \begin{bmatrix} 0.00000 & 1.22394 & 1.22394 & 0.00000 & 0.00000 & 1.22394 \\ 0.00000 & 0.00000 & 0.86546 & 0.86546 & 0.00000 & 0.86546 \\ 0.00000 & 0.00000 & 0.00000 & 0.00000 & 0.00000 & 0.00000 \end{bmatrix}$$

Where it is clear that all the points are in the x^*y^* plane. The fractional coordinates referred to the redefined cell, which is the one used to define the surface, are calculated by using:

$$\mathbf{f}^{*}_{\mathbf{B}} = (\mathbf{B}^{*\mathrm{T}})^{-1}\,\mathbf{r}^{*}_{\mathbf{S}} \tag{A.84}$$

And the $\mathbf{k}^{\mathbf{b}}_{\mathbf{frac}}$ are:

$$\mathbf{f}^{*}_{\mathbf{B}} = \begin{bmatrix} 0.00000 & 0.50000 & 0.50000 & 0.00000 & 0.00000 & 0.50000 \\ 0.00000 & 0.00000 & 0.50000 & 0.50000 & 0.00000 & 0.50000 \\ 0.00000 & 0.25000 & 0.50000 & 0.25000 & 0.00000 & 0.50000 \end{bmatrix}$$

Bibliography

[1] *BESSY II - Helmholtz-Zentrum Berlin (HZB) - website - http://www.lightsources.org/facility/hzb-helmholtz-zentrum-berlin.* 21, 34

[2] N. Bliss R. Buckley et al. J. A. Clarke, D. Angal-Kalinin. Clara conceptual design report - http://www.stfc.ac.uk/astec/resources/pdf/claracdrv2.pdf. 21, 35, 89, 97

[3] *Oscillator FEL clip - http://www.vanderbilt.edu/exploration/multimedia/flash/fel/felworks.htm.* 21, 36

[4] X. F. D. Stragier, O. J. Luiten, S. B. van der Geer, M. J. van der Wiel, and G. J. H. Brussaard. Experimental validation of a radio frequency photogun as external electron injector for a laser wakefield accelerator. *Journal of Applied Physics*, 110(2):024910, 2011. 21, 39

[5] D.H. Dowell, I. Bazarov, B. Dunham, K. Harkay, C. Hernandez-Garcia, R. Legg, H. Padmore, T. Rao, J. Smedley, and W. Wan. Cathode r&d for future light sources. *Nuclear Instruments and Methods in Physics Research Section A: Accelerators, Spectrometers, Detectors and Associated Equipment*, 622(3):685 – 697, 2010. 25, 30, 33, 41

[6] Lingun Liu and William A. Bassett. Compression of ag and phase transformation of nacl. *Journal of Applied Physics*, 44(4), 1973. 25, 71, 72

[7] Lattice parameter determinations with an xray spectrogoniometer by the debyescherrer method and the effect of specimen condition. *Journal of Applied Physics*, 32(8), 1961. 25, 71, 72

[8] G.B Walker and M Marezio. Lattice parameters and zone overlap in solid solutions of lead in magnesium. *Acta Metallurgica*, 7(12):769 – 773, 1959. 25, 71, 72

[9] John Mullay. *Estimation of atomic and group electronegativities*, pages 1–25. Springer Berlin Heidelberg, Berlin, Heidelberg, 1987. 26, 105, 106

[10] M.E. Couprie. New generation of light sources: Present and future. *Journal of Electron Spectroscopy and Related Phenomena*, 196:3 – 13, 2014. Advances in Vacuum Ultraviolet and X-ray Physics, The 38th International Conference on Vacuum Ultraviolet and X-ray Physics (VUVX2013), University of Science and Technology of China. 29

[11] Majed Chergui. Emerging photon technologies for chemical dynamics. *Faraday Discuss.*, 171:11–40, 2014. 29, 38

[12] Wendy R. Flavell, Frances M. Quinn, Jim A. Clarke, Elaine A. Seddon, Neil R. Thompson, Marion A. Bowler, Mark D. Roper, Susan L. Smith, Hywel L. Owen, Bruno D. Muratori, Brian W. McNeil, and Graeme J. Hirst. 4gls: the uk's fourth generation light source, 2005. 29, 30

[13] John M. J. Madey. Stimulated emission of bremsstrahlung in a periodic magnetic field. *Journal of Applied Physics*, 42(5):1906–1913, 1971. 30, 35

[14] *LCLS website - https://portal.slac.stanford.edu/sites/lclspublic/Pages/Default.aspx.* 30, 37

[15] Contents list. *Faraday Discuss.*, 171:3–9, 2014. 30

[16] B.E. Carlsten, E.R. Colby, E.H. Esarey, M. Hogan, F.X. Krtner, W.S. Graves, W.P. Leemans, T. Rao, J.B. Rosenzweig, C.B. Schroeder, D. Sutter, and W.E. White. New source technologies and their impact on future light sources. *Nuclear Instruments and Methods in Physics Research Section A: Accelerators, Spectrometers, Detectors and Associated Equipment*, 622(3):657 – 668, 2010. 30

[17] John W. Lewellen IV. High-brightness electron guns for linac-based light sources, 2004. 30

[18] Astec website - http://www.stfc.ac.uk/astec. 31, 37

[19] *Computational Materials Science Website - http://www.imperial.ac.uk/computational-materials-science.* 2017. 31

[20] *Synchrotron Radiation Theory and Its Development.* 34

[21] S. S. Hasnain, J. R. Helliwell, and H. Kamitsubo. Fifty Years of Synchrotron Radiation. *Journal of Synchrotron Radiation*, 4(6):315, Nov 1997. 34

[22] *Diamond Light Source - Website.* 1999. 35

[23] *ALICE Website - http://www.astec.stfc.ac.uk/ASTeC/Programmes/Alice/35997.aspx.* 37

[24] A. D. Smith, M. R. F. Siggel-King, G. M. Holder, A. Cricenti, M. Luce, P. Harrison, D. S. Martin, M. Surman, T. Craig, S. D. Barrett, A. Wolski, D. J. Dunning, N. R. Thompson, Y. Saveliev, D. M. Pritchard, A. Varro, S. Chattopadhyay, and P. Weightman. Near-field optical microscopy with an infra-red free electron laser applied to cancer diagnosis. *Applied Physics Letters*, 102(5):053701, 2013. 37

[25] *SACLA website - http://xfel.riken.jp/eng.* 37

[26] *FLASH website - http://www.xfel.eu/overview/flash.* 37

[27] *SwissFEL website - https://www.psi.ch/swissfel.* 37

[28] *VELA website - http://www.astec.stfc.ac.uk/ASTeC/Programmes/vela/38427.aspx.* 38

[29] Jan Kern, Roberto Alonso-Mori, Rosalie Tran, Johan Hattne, Richard J. Gildea, Nathaniel Echols, Carina Glöckner, Julia Hellmich, Hartawan Laksmono, Raymond G. Sierra, Benedikt Lassalle-Kaiser, Sergey Koroidov, Alyssa Lampe, Guangye Han, Sheraz Gul, Dörte DiFiore, Despina Milathianaki, Alan R. Fry, Alan Miahnahri, Donald W. Schafer, Marc Messerschmidt, M. Marvin Seibert, Jason E. Koglin, Dimosthenis Sokaras, Tsu-Chien Weng, Jonas Sellberg, Matthew J. Latimer, Ralf W. Grosse-Kunstleve, Petrus H. Zwart, William E. White, Pieter Glatzel, Paul D. Adams, Michael J. Bogan, Garth J. Williams, Sébastien Boutet, Johannes Messinger, Athina Zouni, Nicholas K. Sauter, Vittal K. Yachandra, Uwe Bergmann, and Junko Yano. Simultaneous femtosecond x-ray spectroscopy and diffraction of photosystem ii at room temperature. *Science*, 340(6131):491–495, 2013. 38

[30] Alan Todd. State-of-the-art electron guns and injector designs for energy recovery linacs (erl). *Nuclear Instruments and Methods in Physics Research Section A: Accelerators, Spectrometers, Detectors and Associated Equipment*, 557(1):36 – 44, 2006. Energy Recovering Linacs 2005Proceedings of the 32nd Advanced {ICFA} Beam Dynamics Workshop on Energy Recovering Linacs32nd Advanced {ICFA} Beam Dynamics Workshop on Energy Recovering Linacs. 39

[31] D. A. McQuarrie and J. D. Simon. *Physical Chemistry: A Molecular Approach.* University Science Books, 1997. 43, 65

[32] D. A. McQuarrie and J. D. Simon. *Quantum Chemistry.* University Science Books, 2007. 43

[33] A. Szabo amd N. S. Ostlund. *Modern Quantum Chemistry: Introduction to Advanced Electronic Structure Theory.* Dover Publications Inc. 43

[34] C. Giacovazzo. *Fundamentals of Crystallography.* Oxford University Press, 2002. 43

[35] Srgio Filipe Sousa, Pedro Alexandrino Fernandes, and Maria Joo Ramos. General performance of density functionals. *The Journal of Physical Chemistry A*, 111(42):10439–10452, 2007. PMID: 17718548. 46

[36] Janus J. Eriksen, Pablo Baudin, Patrick Ettenhuber, Kasper Kristensen, Thomas Kjrgaard, and Poul Jrgensen. Linear-scaling coupled cluster with perturbative triple excitations: The divideexpandconsolidate ccsd(t) model. *Journal of Chemical Theory and Computation*, 11(7):2984–2993, 2015. PMID: 26575735. 46

[37] P. Hohenberg and W. Kohn. *Phys. Rev.*, 136:B864–B871, 1964. 46

[38] W. Kohn and L. J. Sham. *Phys. Rev.*, 140:A1133–A1138, 1965. 46

[39] D. M. Ceperley and B. J. Alder. Ground state of the electron gas by a stochastic method. *Phys. Rev. Lett.*, 45:566, 1980. 48

[40] J. Muscat, A. Wander, and N. M. Harrison. *Chemical Physics Letters*, 342:397–401, 2001. 49

[41] M. A. Bravais. *On the Systems Formed by Points Regularly Distributed on a Plane or in Space*. Memoir Number One. The Crystallographic Society of America, 1949. 50

[42] G. Wulff. *Z. Kristallogr.*, 34:449 – 530, 1901. 53, 56

[43] C. Pisani. *Lecture notes in chemistry: quantum-mechanical ab-initio calculation of the properties of crystalline materials*. 1996. 54, 63, 102

[44] S. Vijayalakshmi, A. Fhlisch, F. Hennies, A. Pietzsch, M. Nagasono, W. Wurth, A.G. Borisov, and J.P. Gauyacq. Surface projected electronic band structure and adsorbate charge transfer dynamics: Ar adsorbed on cu(1 1 1) and cu(1 0 0). *Chemical Physics Letters*, 427(13):91 – 95, 2006. 55

[45] K Doll and N.M Harrison. Chlorine adsorption on the cu(111) surface. *Chemical Physics Letters*, 317(35):282 – 289, 2000. 56, 81

[46] K Doll, N M Harrison, and V R Saunders. A density functional study of lithium bulk and surfaces. *Journal of Physics: Condensed Matter*, 11(26):5007, 1999. 56

[47] Conyers Herring. Some theorems on the free energies of crystal surfaces. *Phys. Rev.*, 82:87–93, Apr 1951. 56

[48] John P. Perdew, Kieron Burke, and Matthias Ernzerhof. Generalized gradient approximation made simple. *Phys. Rev. Lett.*, 77:3865–3868, Oct 1996. 57

[49] S. J. Clark, M. D. Segall, C. J. Pickard, P. J. Hasnip, M. J. Probert, K. Refson, and M.C. Payne. First principles methods using CASTEP. *Z. Kristall.*, 220:567–570, 2005. 57

[50] David Vanderbilt. Soft self-consistent pseudopotentials in a generalized eigenvalue formalism. *Phys. Rev. B*, 41:7892–7895, Apr 1990. 57

[51] C. G. Broyden. *J. Appl. Math.*, 6:76–90, 1970. 58

[52] R. Fletcher. *Comput. J*, 13:317, 1970. 58

[53] D. Goldfarb. *Math. Comput.*, 24:23, 1970. 58

[54] D. F. Shanno. *Math. Comput.*, 24:647, 1970. 58

[55] C. N. Berglund and W. E. Spicer. Photoemission studies of copper and silver: Theory. *Phys. Rev.*, 136:A1030–A1044, Nov 1964. 59, 62

[56] J.B. Pendry. Theory of photoemission. *Surface Science*, 57(2):679 – 705, 1976. 59, 87

[57] M Lders, A Ernst, W M Temmerman, Z Szotek, and P J Durham. Ab initio angle-resolved photoemission in multiple-scattering formulation. *Journal of Physics: Condensed Matter*, 13(38):8587, 2001. 60, 87

[58] M. Grass, J. Braun, and G. Borstel. Full-potential photoemission theory. *Phys. Rev. B*, 47:15487–15499, Jun 1993. 60, 61

[59] J Braun and M Donath. Theory of photoemission from surfaces. *Journal of Physics: Condensed Matter*, 16(26):S2539, 2004. 61

[60] G. Thrner and G. Borstel. Relativistic theory of photoemission from solids. i. key aspects of the model. *physica status solidi (b)*, 126(2):617–628, 1984. 61

[61] William E. Spicer and Alberto Herrera-Gomez. Modern theory and applications of photocathodes, 1993. 62

[62] D. H. Dowell, F. K. King, R. E. Kirby, J. F. Schmerge, and J. M. Smedley. *In situ* cleaning of metal cathodes using a hydrogen ion beam. *Phys. Rev. ST Accel. Beams*, 9:063502, Jun 2006. 62, 65, 87

[63] David H. Dowell and John F. Schmerge. Quantum efficiency and thermal emittance of metal photocathodes. *Phys. Rev. ST Accel. Beams*, 12:074201, Jul 2009. 62, 65, 87

[64] S. Hufner. *Photoelectron spectroscopy - 2^{nd} edition.* 1996. 62

[65] Ivo Souza, Nicola Marzari, and David Vanderbilt. Maximally localized wannier functions for entangled energy bands. *Phys. Rev. B*, 65:035109, Dec 2001. 63

[66] N.W. Ashcroft and N.D. Mermin. *Solid State Physics.* Saunders College, Philadelphia, 1976. 64

[67] K. Peiponen V. Lucarini, J. J. Saarinen and E. M. Vartiainen. *Kramers-Kronig Relations in Optical Materials Research.* Springer, 2010. 65

[68] C. J. Powell and A. Jablonski. Evaluation of calculated and measured electron inelastic mean free paths near solid surfaces. *Journal of Physical and Chemical Reference Data*, 28(1), 1999. 66, 67

[69] A. P. Sorini, J. J. Kas, J. J. Rehr, M. P. Prange, and Z. H. Levine. *Ab initio* calculations of electron inelastic mean free paths and stopping powers. *Phys. Rev. B*, 74:165111, Oct 2006. 66, 67

[70] Wolfgang S. M. Werner. Electron transport in solids for quantitative surface analysis. *Surface and Interface Analysis*, 31(3):141–176, 2001. 66, 67

[71] J. D. Bourke and C. T. Chantler. Measurements of electron inelastic mean free paths in materials. *Phys. Rev. Lett.*, 104:206601, May 2010. 66, 67

[72] I. Nagy and P. M. Echenique. Mean free path of a suddenly created fast electron moving in a degenerate electron gas. *Phys. Rev. B*, 85:115131, Mar 2012. 66, 67

[73] J. Szajman, J. Liesegang, J.G. Jenkin, and R.C.G. Leckey. Is there a universal mean-free-path curve for electron inelastic scattering in solids? *Journal of Electron Spectroscopy and Related Phenomena*, 23(1):97 – 102, 1981. 66

[74] C.J. Powell. The quest for universal curves to describe the surface sensitivity of electron spectroscopies. *Journal of Electron Spectroscopy and Related Phenomena*, 47(0):197 – 214, 1988. 66

[75] M. Cadorna and L. Ley. *Photoemission in Solids*. Springer, 1978. 67

[76] S.D. Kevan. *Angle-Resolved Photoemission*. Elsevier, 1992. 67

[77] B. L. Rickman, Joel A. Berger, A. W. Nicholls, and W. Andreas Schroeder. Intrinsic electron beam emittance from metal photocathodes: The effect of the electron effective mass. *Phys. Rev. Lett.*, 111:237401, Dec 2013. 68

[78] Tuo Li, Benjamin L. Rickman, and W. Andreas Schroeder. Emission properties of body-centered cubic elemental metal photocathodes. *Journal of Applied Physics*, 117(13):134901, 2015. 69

[79] Tuo Li, Benjamin L. Rickman, and W. Andreas Schroeder. Density functional theory analysis of hexagonal close-packed elemental metal photocathodes. *Phys. Rev. ST Accel. Beams*, 18:073401, Jul 2015. 69

[80] Roald Hoffmann. How chemistry and physics meet in the solid state. *Angewandte Chemie International Edition in English*, 26(9):846–878, 1987. 69

[81] Chi-Cheng Lee, Yukiko Yamada-Takamura, and Taisuke Ozaki. Unfolding method for first-principles lcao electronic structure calculations. *Journal of Physics: Condensed Matter*, 25(34):345501, 2013. 70

[82] Timothy B. Boykin and Gerhard Klimeck. Practical application of zone-folding concepts in tight-binding calculations. *Phys. Rev. B*, 71:115215, Mar 2005. 70

[83] I. Deretzis, G. Calogero, G. G. N. Angilella, and A. La Magna. Role of basis sets on the unfolding of supercell band structures: From tight-binding to density functional theory. *EPL (Europhysics Letters)*, 107(2):27006, 2014. 70

[84] Fawei Zheng, Ping Zhang, and Wenhui Duan. Quantum unfolding: A program for unfolding electronic energy bands of materials. *Computer Physics Communications*, 189:213 – 219, 2015. 70

[85] Philipp Haas, Fabien Tran, and Peter Blaha. Calculation of the lattice constant of solids with semilocal functionals. *Phys. Rev. B*, 79:085104, Feb 2009. 72

[86] Andrea Marini, Giovanni Onida, and Rodolfo Del Sole. Plane-wave dft-lda calculation of the electronic structure and absorption spectrum of copper. *Phys. Rev. B*, 64:195125, Oct 2001. 72

[87] Andrea Marini, Rodolfo Del Sole, Angel Rubio, and Giovanni Onida. Quasiparticle band-structure effects on the d hole lifetimes of copper within the GW approximation. *Phys. Rev. B*, 66:161104, Oct 2002. 72

[88] E Wachowicz and A Kiejna. Bulk and surface properties of hexagonal-close-packed be and mg. *Journal of Physics: Condensed Matter*, 13(48):10767, 2001. 72, 82, 84

[89] Bao-Qin Fu, Wei Liu, and Zhi-Lin Li. Calculation of the surface energy of hcp-metals with the empirical electron theory. *Applied Surface Science*, 255(23):9348 – 9357, 2009. 72, 81

[90] S Daniuk, T Jarlborg, G Kontrym-Sznajd, J Majsnerowski, and H Stachowiak. Electronic structure of mg, zn and cd. *Journal of Physics: Condensed Matter*, 1(44):8397, 1989. 72

[91] R Asokamani, K Iyakutti, R S Rao, and V Devanathan. Bandstructure of mg and the effect of correlation. *Journal of Physics F: Metal Physics*, 8(11):2323, 1978. 72

[92] S Chatterjee and P Sinha. Energy band structure of beryllium and magnesium. *Journal of Physics F: Metal Physics*, 5(11):2089, 1975. 72

[93] N. E. Christensen. The band structure of silver and optical interband transitions. *physica status solidi (b)*, 54(2):551–563, 1972. 72

[94] S. Lopez-Moreno and A. H. Romero. Atomic and molecular oxygen adsorbed on (111) transition metal surfaces: Cu and ni. *The Journal of Chemical Physics*, 142(15), 2015. 75

[95] Jeff Greeley and Manos Mavrikakis. Surface and subsurface hydrogen: adsorption properties on transition metals and near-surface alloys. *The Journal of Physical Chemistry B*, 109(8):3460–3471, 2005. PMID: 16851380. 75

[96] Ž. Crljen, P. Lazić, D. Šokčević, and R. Brako. Relaxation and reconstruction on (111) surfaces of au, pt, and cu. *Phys. Rev. B*, 68:195411, Nov 2003. 79

[97] Jia-Jun Tang, Xiao-Bao Yang, LiuZhang OuYang, Min Zhu, and Yu-Jun Zhao. A systematic first-principles study of surface energies, surface relaxation and friedel oscillation of magnesium surfaces. *Journal of Physics D: Applied Physics*, 47(11):115305, 2014. 79

[98] L. Vitos, A.V. Ruban, H.L. Skriver, and J. Kollr. The surface energy of metals. *Surface Science*, 411(12):186 – 202, 1998. 81

[99] H. L. Skriver and N. M. Rosengaard. Surface energy and work function of elemental metals. *Phys. Rev. B*, 46:7157–7168, Sep 1992. 81, 82, 84

[100] F. F. Sanches, G. Mallia, and N. M. Harrison. Simulating constant current stm images of the rutile tio2 (110) surface for applications in solar water splitting. 1494:339–344, 2013. 81

[101] Abhijit Chatterjee, Syuichi Niwa, and Fujio Mizukami. Structure and property correlation for ag deposition on -al2o3a first principle study. *Journal of Molecular Graphics and Modelling*, 23(5):447 – 456, 2005. 81

[102] Alan F. Wright, Peter J. Feibelman, and Susan R. Atlas. First-principles calculation of the mg(0001) surface relaxation. *Surface Science*, 302(1):215 – 222, 1994. 81

[103] Poul L. Hansen, Jakob B. Wagner, Stig Helveg, Jens R. Rostrup-Nielsen, Bjerne S. Clausen, and Henrik Topse. Atom-resolved imaging of dynamic shape changes in supported copper nanocrystals. *Science*, 295(5562):2053–2055, 2002. 81

[104] M.F. Luo, G.R. Hu, and M.H. Lee. Surface structures of atomic hydrogen adsorbed on cu(1 1 1) surface studied by density-functional-theory calculations. *Surface Science*, 601(6):1461 – 1466, 2007. 81

[105] P. O. Gartland, S. Berge, and B. J. Slagsvold. Photoelectric work function of a copper single crystal for the (100), (110), (111), and (112) faces. *Phys. Rev. Lett.*, 28:738–739, Mar 1972. 82

[106] C J Fall, N Binggeli, and A Baldereschi. Deriving accurate work functions from thin-slab calculations. *Journal of Physics: Condensed Matter*, 11(13):2689, 1999. 82

[107] E.V. Chulkov and V.M. Silkin. Ab initio calculation of the surface electronic structure of mg(0001). *Solid State Communications*, 58(4):273 – 275, 1986. 82, 84

[108] Herbert B. Michaelson. The work function of the elements and its periodicity. *Journal of Applied Physics*, 48(11), 1977. 82, 84

[109] G.A. Haas, R.E. Thomas, A. Shih, and C.R.K. Marrian. Work function measurements and their relation to modern surface analysis techniques. *Ultramicroscopy*, 11(2):199 – 206, 1983. 84

[110] F. Reinert, G. Nicolay, S. Schmidt, D. Ehm, and S. Hüfner. Direct measurements of the l-gap surface states on the (111) face of noble metals by photoelectron spectroscopy. *Phys. Rev. B*, 63:115415, Mar 2001. 84

[111] N. V. Smith. Phase analysis of image states and surface states associated with nearly-free-electron band gaps. *Phys. Rev. B*, 32:3549–3555, Sep 1985. 84

[112] N.V. Smith. Photoemission and inverse photoemission from surface states on copper. *Applications of Surface Science*, 2223, Part 1(0):349 – 360, 1985. 84

[113] A. Akin Ünal, Christian Tusche, Safia Ouazi, Sebastian Wedekind, Cheng-Tien Chiang, Aimo Winkelmann, Dirk Sander, Jürgen Henk, and Jürgen Kirschner. Hybridization between the unoccupied shockley surface state and bulk electronic states on cu(111). *Phys. Rev. B*, 84:073107, Aug 2011. 84

[114] Y. Yang, S. C. Wu, F. Q. Liu, K. Ibrahim, H. J. Qian, S. H. Lu, and F. Jona. Surface state at the k point of the surface brillouin zone on cu(111). *Phys. Rev. B*, 54:5092–5096, Aug 1996. 84, 85

[115] M. Hengsberger, F. Baumberger, H. J. Neff, T. Greber, and J. Osterwalder. Photoemission momentum mapping and wave function analysis of surface and bulk states on flat cu(111) and stepped cu(443) surfaces: A two-photon photoemission study. *Phys. Rev. B*, 77:085425, Feb 2008. 84

[116] R Courths, B Cord, H Wern, and S Hfner. Angle-resolved photoemission and band structure of copper. *Physica Scripta*, 1983(T4):144, 1983. 84

[117] Aimo Winkelmann, Christian Tusche, A Akin nal, Martin Ellguth, Jrgen Henk, and Jrgen Kirschner. Analysis of the electronic structure of copper via two-dimensional photoelectron momentum distribution patterns. *New Journal of Physics*, 14(4):043009, 2012. 84

[118] F. Pimpec, C.J. Milne, C.P. Hauri, and F. Ardana-Lamas. Quantum efficiency of technical metal photocathodes under laser irradiation of various wavelengths. *Applied Physics A*, 112(3):647–661, 2013. 87, 97

[119] C. P. Hauri, R. Ganter, F. Le Pimpec, A. Trisorio, C. Ruchert, and H. H. Braun. Intrinsic emittance reduction of an electron beam from metal photocathodes. *Phys. Rev. Lett.*, 104:234802, Jun 2010. 87

[120] Nata ša Stojić, Andrea Dal Corso, Bo Zhou, and Stefano Baroni. Ab initio. *Phys. Rev. B*, 77:195116, May 2008. 87

[121] Johannes Lischner, Derek Vigil-Fowler, and Steven G. Louie. Physical origin of satellites in photoemission of doped graphene: An ab initio *gw* plus cumulant study. *Phys. Rev. Lett.*, 110:146801, Apr 2013. 88

[122] A. Lorusso. Overview and development of metallic photocathodes prepared by laser ablation. *Applied Physics A*, 110(4):869–875, 2013. 88, 89

[123] L. Cultrera, S. Grigorescu, G. Gatti, P. Miglietta, F. Tazzioli, and A. Perrone. Photoelectron emission from yttrium thin films prepared by pulsed laser deposition. *Journal of Nanoscience and Nanotechnology*, 9(2), 2009, abstract =. 88, 89

[124] P. F. Moulton. Spectroscopic and laser characteristics of ti:al2o3. *J. Opt. Soc. Am. B*, 3(1):125–133, Jan 1986. 89

[125] M.E. Kiziroglou, X. Li, A.A. Zhukov, P.A.J. de Groot, and C.H. de Groot. Thermionic field emission at electrodeposited nisi schottky barriers. *Solid-State Electronics*, 52(7):1032 – 1038, 2008. 97

[126] E. L. Murphy and R. H. Good. Thermionic emission, field emission, and the transition region. *Phys. Rev.*, 102:1464–1473, Jun 1956. 97

[127] Lingmei Kong, Alan G. Joly, Timothy C. Droubay, Yu Gong, and Wayne P. Hess. Enhanced quantum efficiency from hybrid cesium halide/copper photocathodes. *Applied Physics Letters*, 104(17):–, 2014. 101

[128] Lingmei Kong, Alan G. Joly, Timothy C. Droubay, Yu Gong, and Wayne P. Hess. Enhanced quantum efficiency from hybrid cesium halide/copper photocathodes. *Applied Physics Letters*, 104(17):171106, 2014. 102

[129] V. N. Kulyasov, V. B. Shilov, G. M. Ermolaeva, and V. G. Krasnov. Enhancement of the quantum efficiency of a fluorescence cesium filter. *Optics and Spectroscopy*, 114(4):522–524, 2013. 102

[130] Huaping Lei, Caizhuang Wang, Yongxin Yao, Yangang Wang, Myron Hupalo, Dan McDougall, Michael Tringides, and Kaiming Ho. Strain effect on the adsorption, diffusion, and molecular dissociation of hydrogen on mg (0001) surface. *The Journal of Chemical Physics*, 139(22):224702, 2013. 102

[131] S. Lopez-Moreno and A. H. Romero. Atomic and molecular oxygen adsorbed on (111) transition metal surfaces: Cu and ni. *The Journal of Chemical Physics*, 142(15):154702, 2015. 102, 103

[132] J. Ghijsen, H. Namba, P.A. Thiry, J.J. Pireaux, and P. Caudano. Adsorption of oxygen on the magnesium (0001) surface studied by {XPS}. *Applications of Surface Science*, 8(4):397 – 411, 1981. 103

[133] Michael F. Francis and Edward F. Holby. *Thermodynamics of Passive Film Formation from First Principles*, pages 157–189. John Wiley and Sons, Inc, 2015. 103, 105

[134] Elsebeth Schröder, Roman Fasel, and Adam Kiejna. Mg(0001) surface oxidation: A two-dimensional oxide phase. *Phys. Rev. B*, 69:193405, May 2004. 103, 105

[135] M. F. Francis and C. D. Taylor. First-principles insights into the structure of the incipient magnesium oxide and its instability to decomposition: Oxygen chemisorption to mg(0001) and thermodynamic stability. *Phys. Rev. B*, 87:075450, Feb 2013. 103, 105

[136] Guang xin WU, Su xia LIU, Jie yu ZHANG, Yong quan WU, Qian LI, Kuo chih CHOU, and Xin hua BAO. Density functional theory study on hydrogenation mechanism in catalyst-activated mg(0001) surface. *Transactions of Nonferrous Metals Society of China*, 19(2):383 – 388, 2009. 103

[137] J. C. Slater. Atomic radii in crystals. *The Journal of Chemical Physics*, 41(10):3199–3204, 1964. 103

[138] R. D. Shannon. Revised effective ionic radii and systematic studies of interatomic distances in halides and chalcogenides. *Acta Crystallographica Section A*, 32(5):751–767, Sep 1976. 103

[139] M. Pozzo and D. Alf. Hydrogen dissociation and diffusion on transition metal (= ti, zr, v, fe, ru, co, rh, ni, pd, cu, ag)-doped mg(0001) surfaces. *International Journal of Hydrogen Energy*, 34(4):1922 – 1930, 2009. 105

[140] R. S. Mulliken. Electronic population analysis on lcaomo molecular wave functions. i. *The Journal of Chemical Physics*, 23(10):1833–1840, 1955. 106

[141] B. Camino, T.C.Q. Noakes, M. Surman, E.A. Seddon, and N.M. Harrison. Photoemission simulation for photocathode design: theory and application to copper and silver surfaces. *Computational Materials Science*, 122:331 – 340, 2016. 107

[142] S. Titmuss, A. Wander, and D. A. King. Reconstruction of clean and adsorbate-covered metal surfaces. *Chemical Reviews*, 96(4):1291–1306, 1996. PMID: 11848790. 113

[143] B Zou, C Walker, K Wang, V Tileli, O Shaforost, NM Harrison, N Klein, NM Alford, and PK Petrov. Growth of epitaxial oxide thin films on graphene. *SCIENTIFIC REPORTS*, 6, 2016. 113

[144] M Serri, W Wu, LR Fleet, NM Harrison, CF Hirjibehedin, CWM Kay, AJ Fisher, G Aeppli, and S Heutz. High-temperature antiferromagnetism in molecular semiconductor thin films and nanostructures. *NATURE COMMUNICATIONS*, 5, 2014. 113

[145] S Rousset, V Repain, G Baudot, Y Garreau, and J Lecoeur. Self-ordering of au(111) vicinal surfaces and application to nanostructure organized growth. *Journal of Physics: Condensed Matter*, 15(47):S3363, 2003. 114

[146] Song Xu and Gang-yu Liu. Nanometer-scale fabrication by simultaneous nanoshaving and molecular self-assembly. *Langmuir*, 13(2):127–129, 1997. 119